Acoustofluidic manipulation of cells

Fangda Wu

A thesis submitted for the degree of Doctor of Philosophy

Cardiff University

March 2021

Abstract

This thesis aims to investigate the manipulation of cells, especially cancer cells, via acoustofluidic techniques at high ultrasound frequencies. This PhD project's motivation and ultimate goal are to separate circulating tumour cells (CTCs) from normal blood cells to achieve CTCs detection via acoustofluidic techniques. At the same time, the acoustofluidics-based manipulation of other types of cells and microparticles have also been investigated.

The presence of rare cancer cells in cancer patient blood, called CTCs, has been increasingly researched as an essential biomarker for cancer diagnosis and cancer treatment monitoring. Separation and enrichment of CTCs from cancer patients' blood samples via liquid biopsy methods have shown excellent compatibility compared with the conventional screening and invasive tissue biopsy methods. As a novel, bio-compatible and label-free technique, acoustofluidics has the potential to become an effective tool to sort CTCs from liquid samples or manipulate other types of cells via the cells physical properties: size, density, and compressibility.

In this thesis, acoustofluidic platforms based on standing surface acoustic waves (SSAW) are demonstrated, including the Interdigital transducers (IDTs) design, cleanroom (CR) fabrication, and integration with microfluidics, electronics and mechanics systems. The simulation has been conducted via Governing equations (Continuity and Navier-Stokes equation) and Finite Element Method (FEM) model to understand the working principle and compare it with the microparticles manipulation experiment on the parallel and tilted-angle IDT SSAW devices. Moreover, a conventional tilted-angle (CTA) IDTs acoustofluidic device has been applied to wash the electroporated cells from the original medium, and a higher electroporation

efficiency and cell viability are achieved. By optimising the IDTs patterning, a filled tilted-angle (FTA) IDTs design with less electrical input power but higher acoustic energy generated compared with CTA IDTs is demonstrated that achieves around 90% deflection efficiency of Hela cells with the input power of 4.5 W. In addition, to overcome the challenges of frangibility and overheating due to the conventional SSAW substrates, a novel Gallium Nitride (GaN) compound semiconductor film based acoustic tweezer is demonstrated. Cancer cell patterning via the GaN platform has been successfully achieved with excellent thermal stability with high input power.

SSAW-based acoustofluidic cell manipulation in this thesis extends understanding of acoustofluidics techniques via the novel IDT design and SSAW generation substrate and will enable further development in high precision cell manipulation and biosensors applications.

Acknowledgement

I would like to gratefully appreciate the following people:

My great supervisor and mentor, Dr Xin Yang, for the patient guidance, continuous encouragement and support, as well as for giving me many opportunities to comprehensively understand and participate in various valuable research projects. Dr Ming Hong Shen, Dr Jian Yang, and Dr Chao Sun for their selfless support and great guidance. Prof. Aled Clayton, Prof. Yongqing Fu, Dr Despina Moschou, Dr Siva Sivaraya, Prof. Yuan Fan, Dr You Zhou, Dr Zhihua Xie, Dr Yinhua Dong and Dr Jerome Cuenca for the critical inspiration and great teaching in both theoretical and experimental work of acoustofluidic area. Dr Meng Cai, Dr Jun Wei and Dr Zhenguang Zhang for providing the essential experimental support and biological samples for my research.

My friends and colleagues, Hanlin Wang, Roman Mikhaylov, Dr Xiaoyang Liu, Dr Jian Qin, and other MUSL members and friends at Cardiff, for the support in both research and daily life, the professional and efficient collaboration, and all the unforgettable memories together.

Thanks to colleagues and staff at Cardiff University for providing my PhD scholarships, research funding and PGR support.

Finally, I shall thank my mother and my wife for their support and understanding when I felt most needed.

Table of contents

List of figures

List of tables

List of publication

- **Wu, F**., Shen, M.H., Yang, J., Wang, H., Mikhaylov, R., Clayton, A., Qin, X., Sun, C., Xie, Z., Cai, M. and Wei, J., 2021. An Enhanced Tilted-Angle Acoustofluidic Chip for Cancer Cell Manipulation. IEEE Electron Device Letters, vol. 42, no. 4, pp. 577-580, DOI: 10.1109/LED.2021.3062292.
- Mikhaylov, R., **Wu, F**., Wang, H., Clayton, A., Sun, C., Xie, Z., Liang, D., Dong, Y., Yuan, F., Moschou, D. and Wu, Z., 2020. Development and characterisation of acoustofluidic devices using detachable electrodes made from PCB. Lab on a Chip, 20(10), pp.1807-1814, DOI: 10.1039/c9lc01192g.
- Sun, C., **Wu, F**., Wallis, D.J., Shen, M.H., Yuan, F., Yang, J., Wu, J., Xie, Z., Liang, D., Wang, H. and Tickle, R., 2020. Gallium nitride: A versatile compound semiconductor as novel piezoelectric film for acoustic tweezer in manipulation of cancer cells. IEEE Transactions on Electron Devices, 67(8), pp.3355-3361, DOI: 10.1109/ted.2020.3002498.
- Sun, C., **Wu, F**., Fu, Y., Wallis, D.J., Mikhaylov, R., Yuan, F., Liang, D., Xie, Z., Wang, H., Tao, R. and Shen, M.H., 2020. Thin film Gallium nitride (GaN) based acoustofluidic Tweezer: Modelling and microparticle manipulation. *Ultrasonics*, *108*: 106202, DOI: 10.1016/j.ultras.2020.106202.
- Sun, C., Mikhaylov, R., Fu, Y., **Wu, F**., Wang, H., Yuan, X., Xie, Z., Liang, D., Wu, Z. and Yang, X., 2020. Flexible Printed Circuit Board as Novel Electrodes for Acoustofluidic Devices. IEEE Transactions on Electron Devices, 68(1), pp.393-398, DOI: 10.1109/TED.2020.3039760.

Chapter 1 Project motivation: circulating tumour cells (CTCs) detection via acoustofluidics

The aim of this chapter is to introduce the background of CTCs detection, which is the motivation of this PhD project. CTCs, as a type of essential biomarkers for cancer diagnosis, play a key role during cancer development. This chapter presents and summarizes various techniques for CTCs detection based on the CTCs' Immunoaffinity or biophysical properties, which also can become the guidance for CTCs detection to be applied on acoustofluidic platforms.

1.1 The Role of CTCs

1.1.1 Cancer development via CTCs

Cancer is one of the leading causes of death in the world, and it caused 164,901 deaths out of 367,167 people diagnosed with cancer in the UK in 2017(UK, 2020). In human bodies, cancer is a disease-causing cell to uncontrollably divide, and it is named a tumour when it occurs in solid tissue. Tumour development can begin either in a single cell or a group of cells(Reya et al., 2001). When a series of genetic mutations happen, which occur as a possible result of exposure to radiation, smoking(Tuchin et al., 2011), poor dietary choices(Doyle et al., 2006) or genetic defects(Linehan et al., 2010), this single cell or a group of cells begin to proliferate uncontrollably into more cells. These cells ultimately developed into a solid tumour. There are two types of tumours, benign (noncancerous) and malignant (cancerous). Malignant tumours acquire the ability to spread to other parts of the body by invading the bloodstream and lymphatic vessels(Plaks et al., 2013), which is called metastasis,

causing most of the cancer deaths(Mehlen and Puisieux, 2006). During metastasis, the tumour cells migrate from the primary tumour to other organs, such as the lung, liver, bone and brain(Cen et al., 2012). The existence of circulating tumour cells (CTCs) in the blood of a metastatic cancer patient was originally demonstrated in 1869 by Thomas Ashworth(Allard et al., 2004). 20 years later, by analysing cancer patients' tissue, Paget proposed the "seed and soil" theory indicating the relation between cancer cells and microenvironment(Paget, 1889). The theory defines that metastasis happens when primary tumour cells are compatible with the specific organs. Since then, research related to CTCs and cancer metastasis has been continuously growing, and currently includes molecular characterisation.

The epithelial-to-mesenchymal transition (EMT) and mesenchymal-to-epithelial transition (MET) are essential steps in the tumourigenic process(Chaffer et al., 2007). Epithelial cells, as a barrier of epithelial tissue, perform the cell-cell adhesions(Niessen, 2007, Gumbiner, 1996). Mesenchymal cells, without adhesion, can migrate or differentiate into other kinds of cells(Thiery et al., 2009). The epithelial cells abandon their cell-cell adhesion during the EMT process and become migratable and differentiable into other tissues and organs(Thiery et al., 2009). On the contrary, cells establish cell polarisation during the MET process and form cell-cell contacts and adhesions(Demirkan, 2013). Both transitions can be abnormally activated through an expression of master transcriptional regulators or intercellular signalling pathways(Satelli et al., 2015b, Nagrath et al., 2007). The abnormal activation could facilitate the formation of CTCs leading to the cancer metastasis(Chaffer and Weinberg, 2011, Lambert et al., 2017, Arumugam et al., 2009), i.e., intravasation of cancer cells into the circulatory system, survival of cancer cells during circulation, extravasation of cancer cells and metastatic lesion initiation.

The formation of CTCs was widely recognised as an important step in the metastatic process(Paterlini-Brechot and Benali, 2007, Dong et al., 2013), as shown in Fig. 1.1.

At the beginning of the EMT process, some of the primary tumour cells lose the junctions to other cells or the extracellular matrix (EMC)(Grünert et al., 2003) and become migratable and aggressive (potential CTCs) to the surrounding stromal tissues, which provide strength and shape to hold the parts of the organ(Liu et al., 2015), e.g. vascular. After they invade the bloodstream, the EMT phenotype helps them survive the anoikis (or cell-detachment-induced apoptosis)(Smit et al., 2009). At the same time, the amount of them significantly reduces due to the intercellular collision and blood fluid shear forces(Joosse et al., 2015). After travelling, the surviving CTCs may adhere to and transmigrate through the endothelium on the vascular wall by their EMT-driven integrin(Shibue et al., 2012, Rejniak, 2016). Finally, the MET converts the CTCs back to their epithelial fate (tight adherence and noninvasive) and forms the metastatic lesion(Craene and Berx, 2013). CTCs can also be released from the metastatic tumour, affecting the growth of the primary tumour(Xue et al., 2014).

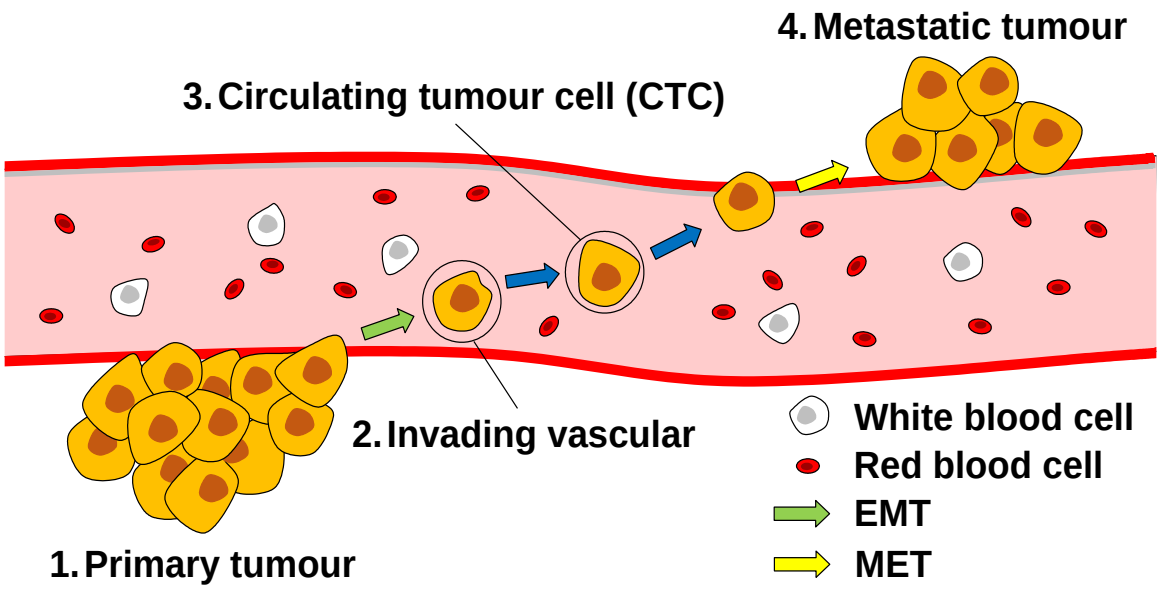

Fig. 1.1 The role of circulating tumour cell (CTC) in cancer metastasis. CTC is released from a primary tumour and then invades the vascular via epithelial-to-mesenchymal transition (EMT). After travelling through the vascular system, the extravasation of CTCs from vascular via mesenchymal-to-epithelia transition (MET) develops to the metastatic tumour.

1.1.2 CTCs and liquid biopsy

Currently, imaging screening (e.g. X-Ray, mammogram, and CT, or non-ionising imaging, such as MRI and ultrasound) combined with pathological and histological examinations are the conventional techniques to diagnose a malignant tumour(Yang et al., 2018, Guan et al., 2018). Pathological and histological examinations are defined as performing fixed staining on specimens from biopsy or surgery and then diagnosing the samples under the microscope. However, early tumour diagnosis and new metastasis are difficult to be detected through those methods because of the limitation of imaging screening resolution(Yang et al., 2018). Although the conventional clinical biopsy, which is a procedure of removing a small amount of tissue, can become the

guide to the cancer treatment(Mikhaylov et al., 2020, Wang et al., 2017), several invasive and time-consuming biopsies for each patient are always needed due to that tumours can generate corresponding resistance to the clinical treatment, or the presence of multiple tumour sites(Gibson, 2019, Steinbichler et al., 2018). Therefore, a more sensitive but more minimally invasive method is strongly needed for patients' cancer diagnoses(Poulet et al., 2019).

Compared to conventional biopsy from solid tissue, liquid biopsy uses the components (biomarkers) in the bodily fluids samples, especially blood, for a real-time and noninvasive monitoring of disease status(Mader and Pantel, 2017). With the development of sensitivity of detecting and analysing cancer biomarkers, CTC liquid biopsy has been widely applied to cancer diagnosis and individual treatment by examining serum(Mellby et al., 2018) and other biofluids, including urine(Jain et al., 2019), saliva(Lousada-Fernandez et al., 2018), and cerebrospinal fluid(Shankar et al., 2017). Moreover, non-invasive liquid biopsy can reduce the anxiety of patients for frequently screening(Mattox et al., 2019). In addition, a single biopsy from the primary tumour cannot reflect all the variety in the tumour. In contrast, the liquid biopsy's random sampling can reveal the heterogeneity within the tumour(Reiter et al., 2018).

CTCs contain the tumour genetic information(Heitzer et al., 2019), based on which clinical cancer diagnostic techniques have been continuously researched(Cristofanilli et al., 2005, Cohen et al., 2008, De Bono et al., 2008). CTC research has its unique advantages over other analytes in cancer biology study, e.g. to help to find the relationship between cell aggregation and metastasis formation(Bray et al., 2018, Hogan et al., 2019). CTCs in the circulation system provide accessible biomarkers to diagnose and characterise tumours and show predictive and prognostic information regarding disease relapse, overall survival and tumour response to therapy in patients(Cohen et al., 2008, Uen et al., 2008, Wong et al., 2009).

The CTC-liquid biopsy can achieve more early-stage cancer diagnosis than conventional image screening with tissue biopsy diagnosis, which needs the solid tumour size to reach the screening resolution(Katayama et al., 2012). CTCs have been confirmed by more and more studies to be used as a diagnostic biomarker for nasopharyngeal carcinoma(Zhang et al., 2018), pancreatic cancer(Qi et al., 2018b, Samandari et al., 2018), breast cancer(Yin et al., 2019, Trapp et al., 2019), liver cancer(Su et al., 2018, Qi et al., 2018a, Li et al., 2018), colon cancer(Tan and Wu, 2018, Weng et al., 2018) and lung cancer(Lowe, 2018, Lim et al., 2018, Messaritakis et al., 2018), e.g. CTCs were detected in 92% of nasopharyngeal carcinoma patients while the healthy people were the control(Zhang et al., 2018).

Along with the cancer diagnosis, staging always relates to the extent of cancer, which can provide potential survival chances and help identify the suitable clinical treatment for the cancer patients(Institute, 2015). TNM stages system is the current standard for a detailed determination of the extent of cancer(Woodard et al., 2016). T refers to the condition of the primary tumour, N represents whether cancer has migrated to lymph nodes, and M indicates whether cancer has spread to other parts of the patient's body. Following each of T, N or M, there is a letter of X or a number that starts from 0. X means the condition cannot be assessed, and the number means the severity (0 means no sign of cancer). Currently, the standard of care is to treat all cancer patients with a certain stage with adjuvant therapy(Staff, 2020). Adjuvant therapy is the treatment in addition to the primary surgery to prevent cancer recurrence. Adjuvant therapy includes chemotherapy, hormonal therapy, antibody therapy and radiation therapy and can be one or more simultaneously. However, there is not a perfectly reliable method to accurately and efficiently identify the stage of each patient. Cancer misdiagnosis or a delay in cancer diagnosing can result in unnecessary toxic effects of adjuvant therapy and micrometastatic lesions to tumour relapse(Mattox et al., 2019). Micrometastatic lesions are defined as "lesions having a

histological diameter of 1mm or less."(Nanko et al., 1998) Recent research has suggested that liquid biopsy after surgery could have a promising indication about the relationship between the CTCs detected from the patient and the tumour relapse rate (patients with tumour recurrence/ total patients number)(Tie et al., 2016)(Clarke et al., 2006), which can be used as additional guidance for choosing a therapy. The number of CTCs in peripheral blood is important in guiding the staging of oesophagal squamous cell carcinomas(Han et al., 2018), pancreatic cancers(DiPardo et al., 2018, Yadav et al., 2018), breast cancer(Yin et al., 2019), colon cancer(Brown et al., 2018, Santasusagna et al., 2018), lung cancer(Lu and Han, 2018, Kapeleris et al., 2018), liver cancer(Nam et al., 2016, Labgaa and Villanueva, 2015, Li et al., 2018) and cervical cancer(Wen et al., 2018). In the peripheral blood, the number of CTCs was found significantly higher from pancreatic cancer(Qi et al., 2018b, Samandari et al., 2018) and breast cancer(Yin et al., 2019) patients with metastasis than those without metastasis, e.g. regarding the oesophagal squamous cell carcinomas(Han et al., 2018) and pancreatic cancer(DiPardo et al., 2018, Yadav et al., 2018), the number of CTCs was found significantly higher in late-stage patients' peripheral blood than the others.

The number of CTCs detected via liquid biopsy can also be used to frequently monitor the clinical efficacy in cancer treatment(Yu et al., 2011), such as pancreatic cancer(Qi et al., 2018b, Samandari et al., 2018), breast cancer(Trapp et al., 2019), gastric cancer(Szczepanik et al., 2019, Kang et al., 2017, Li et al., 2015d) and colon cancer(Tan and Wu, 2018). According to the clinical studies, the number of CTCs detected in gastric cancer patients dropped significantly after the chemostherapy(Szczepanik et al., 2019, Kang et al., 2017, Li et al., 2015d). 14 of 32 (44%) patients initially diagnosed with CTCs positive were found CTCs negative after chemotherapy(Court et al., 2016). The amount of CTCs from pacreatic(Qi et al., 2018b, Samandari et al., 2018) and breast cancer(Trapp et al., 2019) patients'

peripheral blood after-treatment were also detected less than before-treatment. The summary of clinical implications of CTCs-liquid biopsy is described in Table. 1.1.

Table. 1.1 Clinical implications of CTCs-liquid biopsy

Phase	Aim	Tumour type	References
Initial diagnosis	Cancer diagnosis	Nasopharyngeal carcinoma	(Zhang et al., 2018)
		Pancreatic cancer	(Qi et al., 2018b, Samandari et al., 2018)
		Breast cancer	(Yin et al., 2019, Trapp et al., 2019)
		Liver cancer	(Su et al., 2018, Qi et al., 2018a, Li et al., 2018)
		Colon cancer	(Tan and Wu, 2018, Weng et al., 2018)
		Lung cancer	(Lowe, 2018, Lim et al., 2018, Messaritakis et al., 2018)
Therapeutics	Metastasis diagnosis	Oesophagal squamous cell carcinomas	(Han et al., 2018)
		Pancreatic cancers	(DiPardo et al., 2018, Yadav et al., 2018)
	Cancer staging indication	Breast cancer	(Yin et al., 2019)
		Colon cancer	(Brown et al., 2018, Santasusagna et al., 2018)
	Individual treatment guidance	Lung cancer	(Lu and Han, 2018, Kapeleris et al., 2018)
		Liver cancer	(Nam et al., 2016, Labgaa and Villanueva, 2015, Li et al., 2018)
		Cervical cancer	(Wen et al., 2018)
Treatment monitoring	Clinical efficacy monitoring	Pancreatic cancer	(Qi et al., 2018b, Samandari et al., 2018)
		Breast cancer	(Trapp et al., 2019)
	Individual treatment response	Gastric cancer	(Szczepanik et al., 2019, Kang et al., 2017, Li et al., 2015d)
		Colon cancer	(Tan and Wu, 2018)

Compared to the conventional screening methods combined with tissue biopsy, the CTC detection technique via liquid biopsy has competitive advantages, such as non-

invasive and real-time monitoring. It has been applied in various types of cancer diagnoses. However, CTCs have an extremely low concentration in peripheral blood (usually 1-100 CTCs/mL of blood)(Li et al., 2015a). Thus effective detection of CTCs from the blood sample is challenging.

1.2 Technologies for CTC detection

As the gold standard of CTC detection technology, CellSearch® (Veridex LLC, NJ, US) was approved by the U.S. food and drug administration (FDA) for CTC detection and enumeration. CellSearch® is a marker-dependent assay detecting and enumerating CTCs from a 7.5-mL blood sample by using three different antibodies: the epithelial cell adhesion molecule (EpCAM), lymphocyte common antigen (CD45) and cytokeratin (CK)(Search, 2020). As shown in Fig. 1.2, the blood sample is first centrifuged to remove the plasma from the solid blood components and then mixed with antibody-coated magnetic iron nanoparticles and fluorescent dye. Anti-EpCAM coated on the ferrofluid nanobeads are used to catch the CTCs. Since the nanobeads can also catch leukocytes (with EpCAM), to exclude the contamination of leukocytes, the fluorescent antibodies anti-CK and anti-CD45 are added, which will bind to CTCs and leukocytes, respectively. Cell nuclei dye DAPI (4',6-diamidino-2-phenylindole) is also added for further CTCs microscopy identification. By applying a magnetic field at the view of digital fluorescent microscopy, the nanobeads with epithelial cells (CTCs and leukocytes) are pulled to a focal depth under the microscopy for detecting and counting. The cells with CK+, DAPI and CD45- expression will be identified as CTCs while the cells with CK-, DAPI and CD45+ as leukocytes to exclude the contamination.

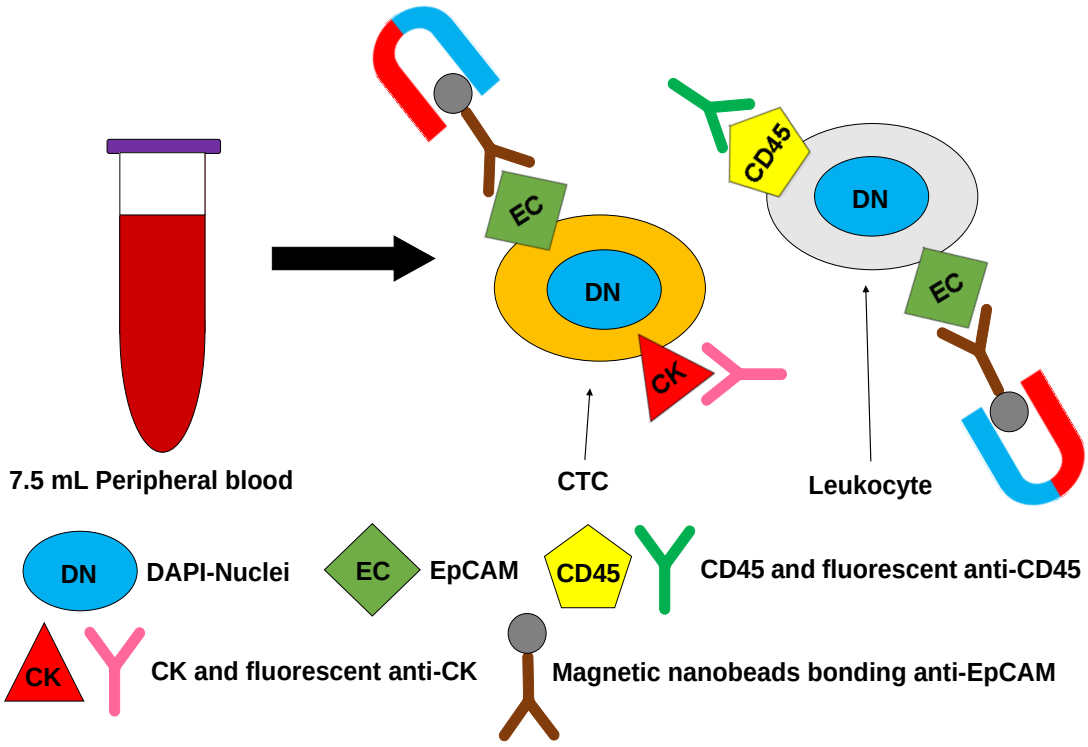

Fig. 1.2 Schematic diagram of CellSearch® system. Peripheral blood from cancer patients is added with magnetic beads connected with EpCAM and fluorescent CK and CD45 antibodies to catch and identify CTCs and leukocytes. Then the magnetic field is applied to harvest the captured CTCs and leukocytes with DAPI-Nuclei under the microscope for identification.

CellSearch® has already been used in metastatic cancer prognosis estimation, therapeutic efficacy monitoring and potential cancer survival rate guidance in breast, prostate and colorectal cancers(van de Stolpe et al., 2011, Riethdorf et al., 2018). It greatly depends on the EpCAM expressing(Cristofanilli et al., 2004) while CTCs with negative EpCAM expression will not be recognised, which has been observed during disease progression and metastasis(Truini et al., 2014). For instance, recent research reports that many CTCs from patients with early and metastatic lung cancer were failed to be detected by CellSearch®(Hanssen et al., 2016). There were only 35% of metastatic patients diagnosed CTCs positive(Hanssen et al., 2016). Thus it can result

in a high cost for each detection but incomplete detection of all populations of CTCs(Shen et al., 2017).

Recently, various techniques targeting the detection of the extremely rare CTCs from patients blood have been applied through different approaches. The platforms for the CTCs detection can be generally broken down into immunoaffinity-based and biophysical property-based approches(Yu et al., 2011). Capture efficiency, enrichment efficiency, purity, throughput and cells viability are defined to help identify the detection performance of the various approaches(Jin et al., 2014), as shown in Table. 1.2.

Table. 1.2 Parameters for identifying device performance of CTCs detection approaches(Jin et al., 2014).

Parameter	Definition
Capture efficiency	The ratio of captured tumour cells to the tumour cells in the original samples
Enrichment efficiency	Similar to capture efficiency but emphasizing the increase of tumour cells in the samples volume
Purity	The capability to avoid contamination of cells other than tumour cells
Throughput	The number of cells to be processed by the device in a unit of time
Cells viability	Quantification of the number of live cells

1.2.1 Immunoaffinity-based approaches

Antibodies, also named Y-shaped proteins, can specifically bind to antigens that can stimulate the immune system to generate a response. Immunoaffinity-based CTC enrichment or capture technique uses the unique binding between antigens and antibodies of CTCs or other cells to separate them. The positive detection method capture CTCs by the antibodies only targeting CTCs rather than other cells in the

collected sample. The EpCAM surface marker is generally used in the positive enrichment approaches to target tumour cells from cancer patients' blood(Pantel et al., 2012). On the contrary, the negative method depends on the antigens not expressed on CTCs but other cells. Antibodies against CD45 are normally used in the negative enrichment method to separate CTCs from leukocytes in blood (Ferreira et al., 2016), while the removal of other components of blood needs centrifugation or blood lysis(Ferreira et al., 2016). Comparing the positive and negative methods, the former typically results in higher purity because there is no extra centrifugation or blood lysis, which can cause sample loss. Sample loss represents the cells loss inside the device during the enrichment or capture process. The negative methods can avoid the incomplete detection of CTCs by being independent of CTCs' unique antigen expression(Yang et al., 2009, Lara et al., 2004, Baccelli et al., 2013).

CTC capturing devices combining immuno-markers with magnetics have been reported in many studies as the immunomagnetic method. The MagSweeper (Fig. 1.3 a) achieved the CTCs capture efficiency of 62 ± 7% with a purity of 51 ± 18% using round-bottom neodymium magnetic rods covered with removable nonadherent plastic sleeves(Talasaz et al., 2009). The samples before CTCs capturing were firstly mixed with magnetic beads functionalised with an antibody that targeted CTCs. Then the magnetic rods were able to capture the magnetic beads connecting the target CTCs from the samples. Its capture-wash-release method allowed a blood process rate of 9 ml/h and was validated by detecting no CTCs from 5 healthy donors while CTCs-positive from all 17 metastatic breast cancer patients. Another device using biomimetic immuno-magnetosomes (IMSs) was introduced (Fig. 1.3 b) that achieved 70-90% of CTCs from the samples mixed with Leukocytes in 15 mins(Xiong et al., 2016). The IMCs are fabricated by coating dibenzocyclooctyne group-modified antibody (DBCO-Ab), which aims the EpCAM on CTCs, on the azide (N_3) leukocyte membrane magnetic nanoclusters (LMNCs). The LMNCs can make the

magnetosome be repelled from leukocytes in the peripheral blood(Rodriguez et al., 2013). The magnetic nanoclusters can supply a higher magnetic field than the single magnetic beads without a larger size or external magnetic field for the following capture-separate process. The CTCs capture was implemented by applying a magnetic field on the samples for 15 mins to capture the IMS connecting with CTCs and then removing the rest of the samples. In addition, Strep-tag® is another immunomagnetic system that can capture and release CTCs with 79% capture efficiency, 70% release rate and 85% CTCs viability for a further cancer diagnosis and therapy analysis, such as molecular profiling(Lu et al., 2015). As shown in Fig. 1.3 c, Strep-Tactin-coated magnetic beads (STMBs) react with the strep-tag II (labelled immunoglobulin G (IgG)) and form the IgG-STMBs, which can interact with multiple types of antibodies targeting CTCs, i.e., anti-EpCAM, anti-EGFR (epidermal growth factor receptor) and anti-HER2 (human epidermal growth factor receptor 2). The captured CTCs with Strep-tag II can be released by adding D-biotin, which interact with STMBs. Strep-tag® was validated by successfully isolating CTCs from 17 patients peripheral blood samples.

On the contrary, a negative immunomagnetic CTCs enrichment approach called EasySep™ targets blood cells instead of CTCs using CD45 and CD66b antibodies. It has been tested with cancer cell line spiked samples with a cancer cells recovery rate of around 42% while a red blood cell (RBC) contamination around 9000 RBC/ml. Although it provides a short detection time (25 min for 1 ml sample) and can capture the CTCs without labelling, the purity of captured CTCs is low, which is unfriendly for further analysis.

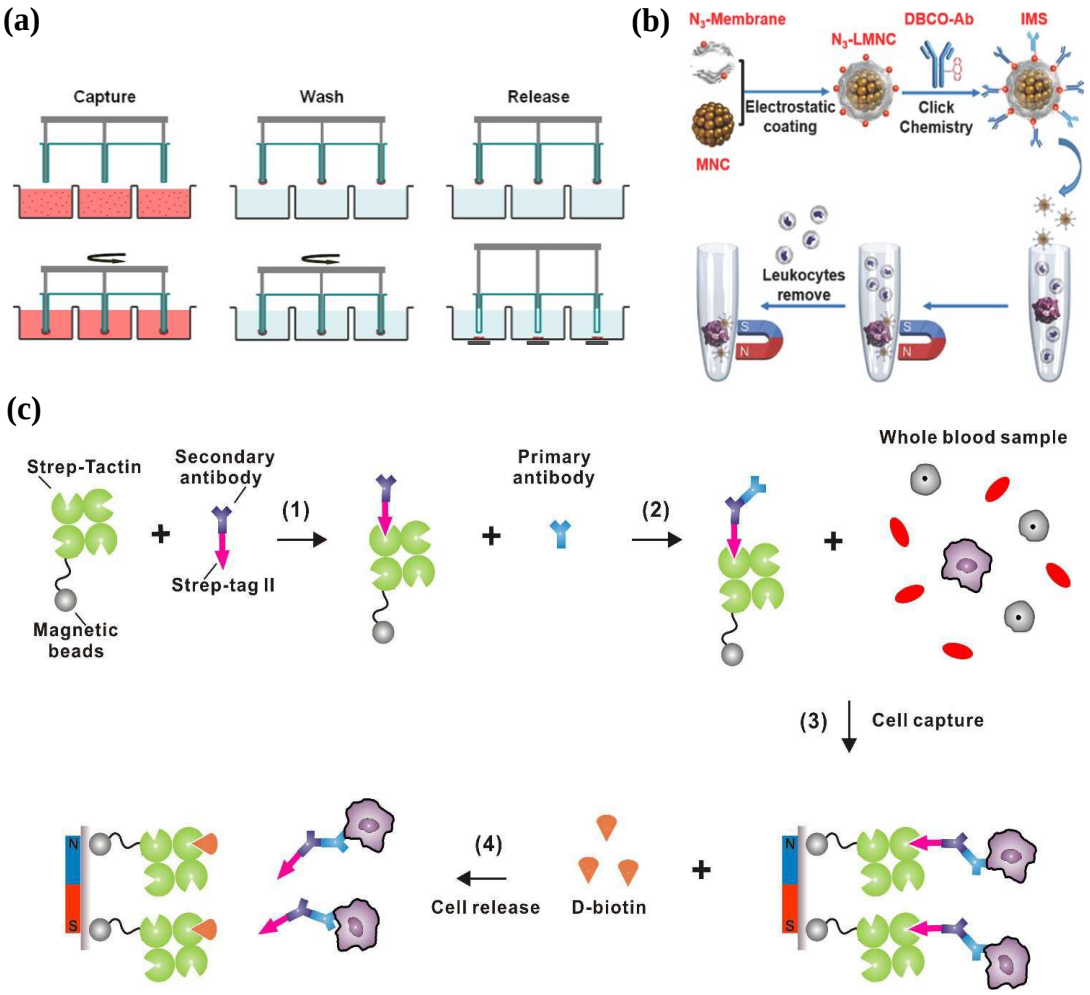

Fig. 1.3 Schematic of different immunomagnetic CTCs enrichment (a) MagSweeper(Talasaz et al., 2009) uses magnetic rods covered with removable sleeves to harvest CTCs via a capture-wash-release process from blood samples. (b) biomimetic immuno-magnetosomes (IMSs)(Xiong et al., 2016) is developed with antibody-coated magnetic beads for CTC capture under a magnetic field. (c) Strep-tag®(Lu et al., 2015) achieves CTC capture and release by biotin-triggered decomposable immunomagnetic beads.

CTCs immunocapture via microfluidic (immuno-microfluidic enrichment) devices is another emerging technique since cell-antibody contact and capture efficiency can be precisely controlled and improved by the fabricated structures in micro-scale(Ferreira

et al., 2016). A microfluidic device with surface-immobilized anti-EpCAM antibodies was developed and successfully captured CTCs from the breast cancer cell line-spiked blood samples with a recovery rate reaching 97%(Dharmasiri et al., 2009). Fig. 1.4 a presents the microfluidic channel structure of this CTCs capturing system, and the structure of the sinusoidal channels (part D of Fig. 1.4 a) allows improved cell-antibody contact. CTC-Chip, as shown in Fig. 1.4 b, is another immuno-microfluidic CTCs enrichment device that was validated by captured CTCs from the peripheral blood of patients with metastatic cancer (e.g., lung, prostate, breast, colon and pancreatic cancers) with the CTCs recovery rate, purity and cell viability of 60%, 50% and 98%, respectively(Nagrath et al., 2007, Maheswaran et al., 2008). The device was functionalised by coating anti-EpCAM on the micropillars, which can provide sufficient surface area for contacting CTCs(Ma et al., 2015). Since the nonspecific leukocyte can also adhere to the micropillars with antibodies, a geometrically enhanced differential immunocapture (GEDI) chip was developed to decrease the contacting opportunity between the leukocyte and micropillars. As shown in Fig. 1.4 c, the cells will follow different streamlines in the microchannel depending on their size. The CTCs (blue in the picture) are larger than the leukocytes (yellow in picture) thus will more frequently interact with the immuno-coated surfaces; thus, the purity of captured CTCs increases. A CTCs capture efficiency of 85% was achieved from the anti-prostate specific membrane antigen (PSMA) cell lines spiked sample with a purity of 68%.

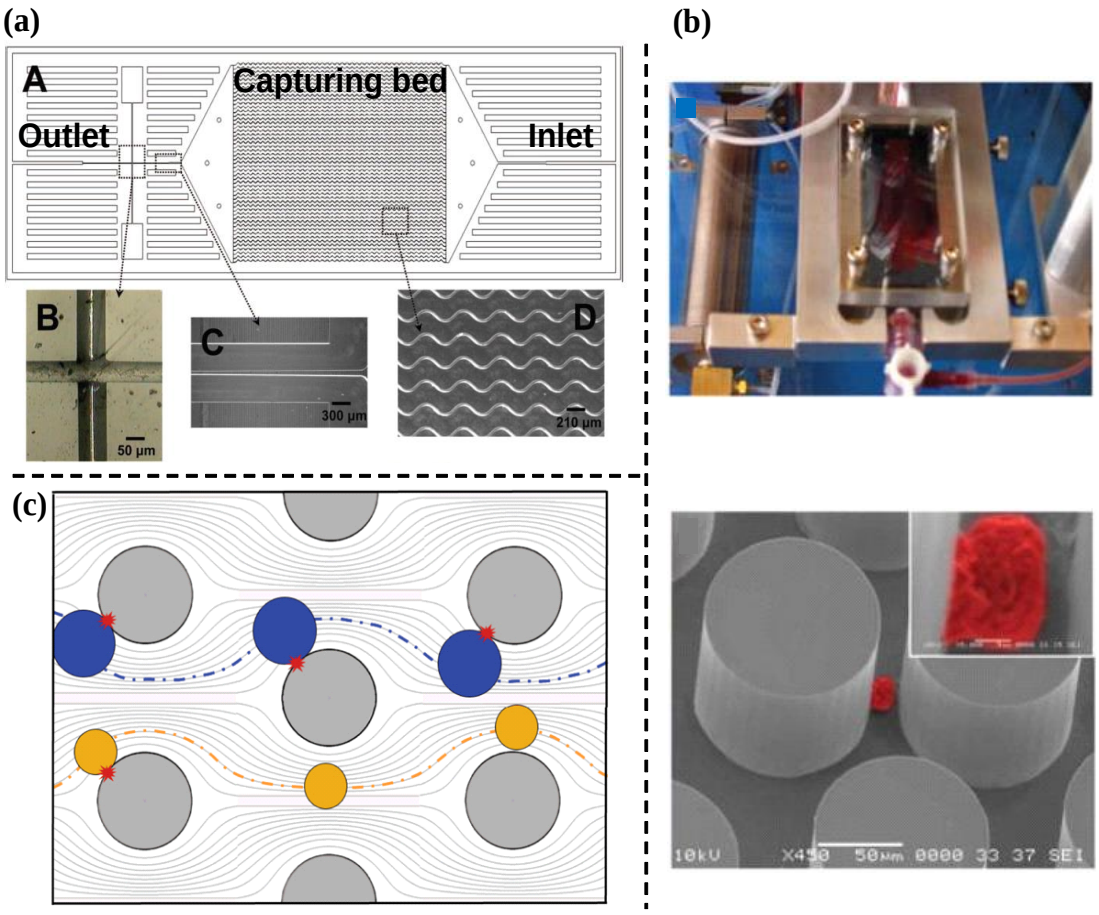

Fig. 1.4 Schematic of different immuno-microfluidic CTCs enrichment (a) micro-chip based micro sampling unit (HTMSU)(Dharmasiri et al., 2009, Adams et al., 2008) retain CTCs via an antibody-coated microfluidic channel (b) CTC-Chip(Nagrath et al., 2007) uses microfluidic channel containing various antibody-coated micropillars to capture CTCs (red in the picture) (c) geometrically enhanced differential immunocapture (GEDI) chip(Gleghorn et al., 2010) improved the micropillars (grey in picture) geometrical arrangements for an enhanced CTCs (blue in the picture) capture and decreased the contacting opportunity between the leukocyte (yellow in picture) and micropillars.

The contact between CTCs and antibodies plays an important role in microfluidic immunocapture. Thus nanomaterials that have a larger surface area for more antibodies bonding can increase the capture efficiency. A polymer-GO (polymer

graphene oxide) chip is developed with biocompatible graphene oxide nanosheets coated with EpCAM antibodies and covered by microfluidic channels for CTCs capture, observation and culturing(Yoon et al., 2016). As shown in Fig. 1.5 a. the GO nanosheets, as biocompatible nanomaterials, have a large surface area for binding anti–EpCAM to capture CTCs. The GO nanosheets are built on a thermoresponsive polymer which is thermal responsive material and can release CTCs (below 12℃) for downstream analysis. In the cancer patients blood tests, CTCs capturing efficiency was 80% and 67% for metastatic breast cancer and pancreatic cancer, respectively. Fig. 1.5 b indicates a silica nanopillar (SiNP) based microfluidic platform, and it also achieved an enhanced CTCs capture by increasing the CTCs-antibodies contact frequency via nanomaterials and unique channel structures(Wang et al., 2011). The serpentine chaotic mixer induces vertical flow that leads CTCs towards the bottom SiNP coated with EpCAM for more frequent interaction. In the test of prostate cancer patients blood, compared with CellSearch®, the SiNP chip captured significantly more CTCs in 17 out of 26 samples while neither platform captured CTCs in the rest of the samples.

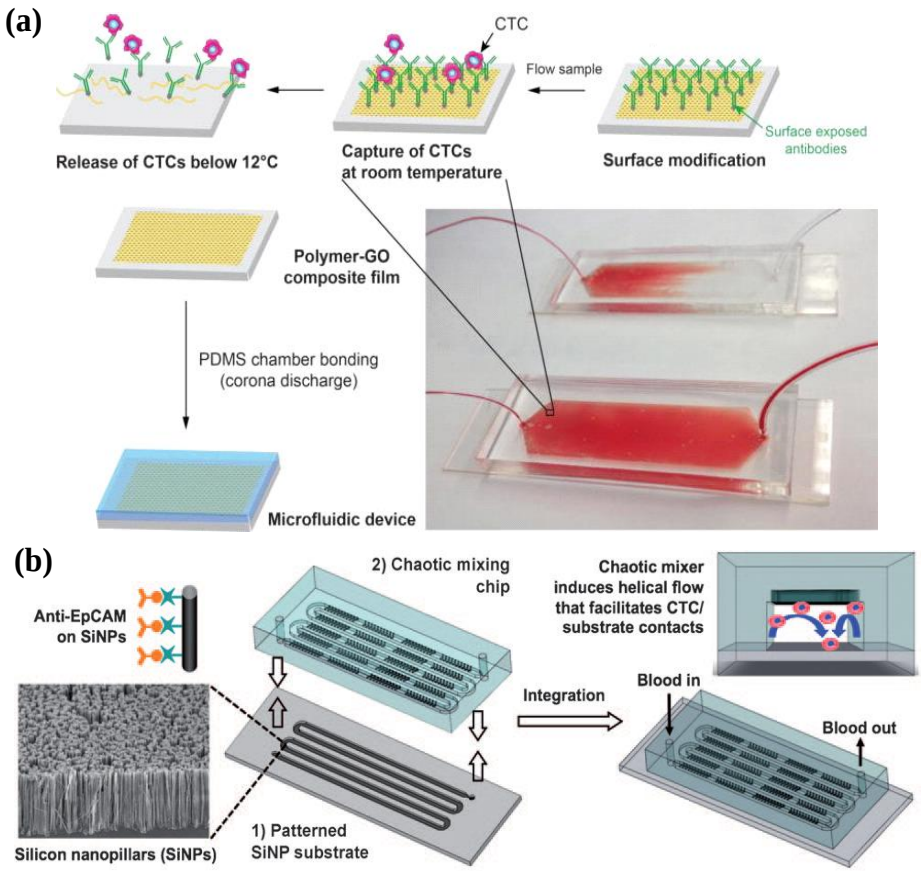

Fig. 1.5 Schematic of nanomaterial-enhanced CTCs enrichment (a) polymer-GO (graphene oxide) chip(Yoon et al., 2016) uses thermal-sensitive GO as the bottom substrate bonded with antibodies for capture and release CTCs. (b) silica nanopillar (SiNP) chip(Wang et al., 2011) increased the CTC-antibody interaction area for an enhanced capture.

In recent research, false-positive results in CTC immunoaffinity-based detection can happen as nonmalignant epithelial cells having similar epithelial expression with CTCs were also found in patients with benign colon(Pantel et al., 2012), pancreatic(Cauley et al., 2015) and breast(Franken et al., 2012, Crisan et al., 2000) diseases. Although more alternative epithelial CTCs antigens were developed, e.g., EGFR, HER2, mucin 1 (MUC1), stem cell markers (CD133) and mesenchymal markers (vimentin)(Satelli et al., 2015a), the EMT can cause the epithelial markers to

down-regulated (reduction in cellular response) or lost(Polyak and Weinberg, 2009), which results in the escape of CTCs from enrichment or critical CTCs missing(Gorges et al., 2012). The surface expression of CTCs varies among the diverse range of tumours, and there is no universal CTC antigens found(Ferreira et al., 2016). Therefore, it is challenging to capture CTCs with a representative population for current positive immunoaffinity-based enrichment approches(Marrinucci et al., 2010, Mikolajczyk et al., 2011, Pecot et al., 2011, Serrano et al., 2014). In addition, the positive method of bonding CTCs on the device surface or magnetic particles after enrichment increases the difficulty of further biological analysis(Bankó et al., 2019) because extra steps to release the CTCs from them are required. Regarding the negative enrichment method, although it is independent of CTCs' labels, compared with positive methods, the lower purity of collected samples and higher sample loss due to the extra centrifugation of blood samples also makes it challenging for further analysis(Yang et al., 2009)(Lara et al., 2004, Baccelli et al., 2013, Ferreira et al., 2016).

1.2.2 Biophysical property-based approaches

As to the CTCs detection in blood samples, the physical and mechanical properties between CTCs and normal blood cells are different, such as density, size and deformbility(Ahn et al., 2020). Based on these distinguishable biophysical properties, CTCs can be separated and enriched with avoiding inaccuracy caused by the heterogeneous antigen expression in CTCs(Harouaka et al., 2013).

CTC microfiltration is one of the biophysical property-based approaches that normally contains various pores in micro-scale to filter cells depending on their size and deformity. A tandem flexible micro spring array (tFMSA) has been developed for CTCs separation(Yeh et al., 2017, Harouaka et al., 2014). tFMSA (Fig. 1.6 a) contains a

single layer of parylene diaphragm where four areas of FMSA membranes are patterned and can block CTCs from the sample flow (red arrows in the picture). There are two layers of polydimethylsiloxane (PDMS) with four wells and channel structures guiding the sample flow so that the device allows up to 4 distinct sizes of cells to be captured. The sample flow is controlled by a syringe withdrawing at the outlet. Spiked cancer cells lines (breast cancer and melanoma) sample was tested with a capture efficiency and viability of 90% and 80%, respectively. As shown in Fig. 1.6 b, another CTC microfilter named separable bilayer (SB) has a double parylene-C layer structure with two sizes of holes hexagonally respectively distributed on the top and bottom layers(Zhou et al., 2014). The device is designed to trap CTCs along the edges of the large top hole where the mechanical stress on cells reduces drastically, and the captured cells can be released by disassembling the bilayer structure. By pumping the samples towards the top layer, tumour cells with a larger size can be trapped between the parylene-C membrane while leukocytes and red blood cells pass through the microfilter. The SB microfilter was tested with cancer cell lines mixed with blood from healthy donors with a capture efficiency of around 80%.

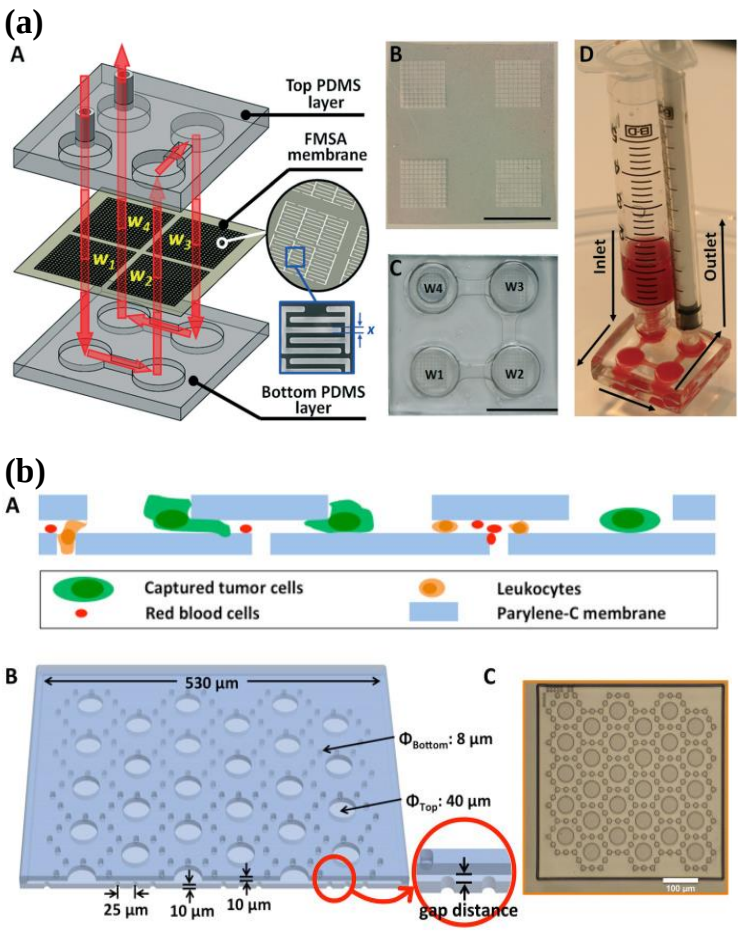

Fig. 1.6 Schematic of microfiltration-based CTCs enrichment (a) tandem flexible micro spring array (tFMSA) microfilter(Yeh et al., 2017) has been developed with a unique filter structure allowing 4-times CTCs filtering from blood samples. (b) separable bilayer (SB) microfilter(Zhou et al., 2014) uses double-layer porous membranes with hexagonally arranged holes for harvesting CTCs.

Microfluidic chips without immuno-method have also been developed for capturing and enriching CTCs. Depending on cells size, ANGLE utilises stepped structures and a reverse flow to capture CTCs within a disposable microfluidic channel called Parsortix while allowing other blood cells to pass through(Hvichia et al., 2016, ANGLE, 2019), as shown in Fig. 1.7 a. Cancer cell line spiked sample was used to validate the device resulting in 54-69% enrichment rate. Fig. 1.7 b shows another size-based

CTCs sorting microfluidic device that has been developed by using dean flow fractionation (DFF) in a spiral microchannel(Hou et al., 2013). During one cycle, cancer cells from the blood sample can be dragged to one side opposite to where the healthy blood cells are due to their larger size. Blood samples from metastatic lung cancer patients were used to test the DFF device, and CTCs were captured from all 20 samples while there were around 440 leukocytes/mL contamination.

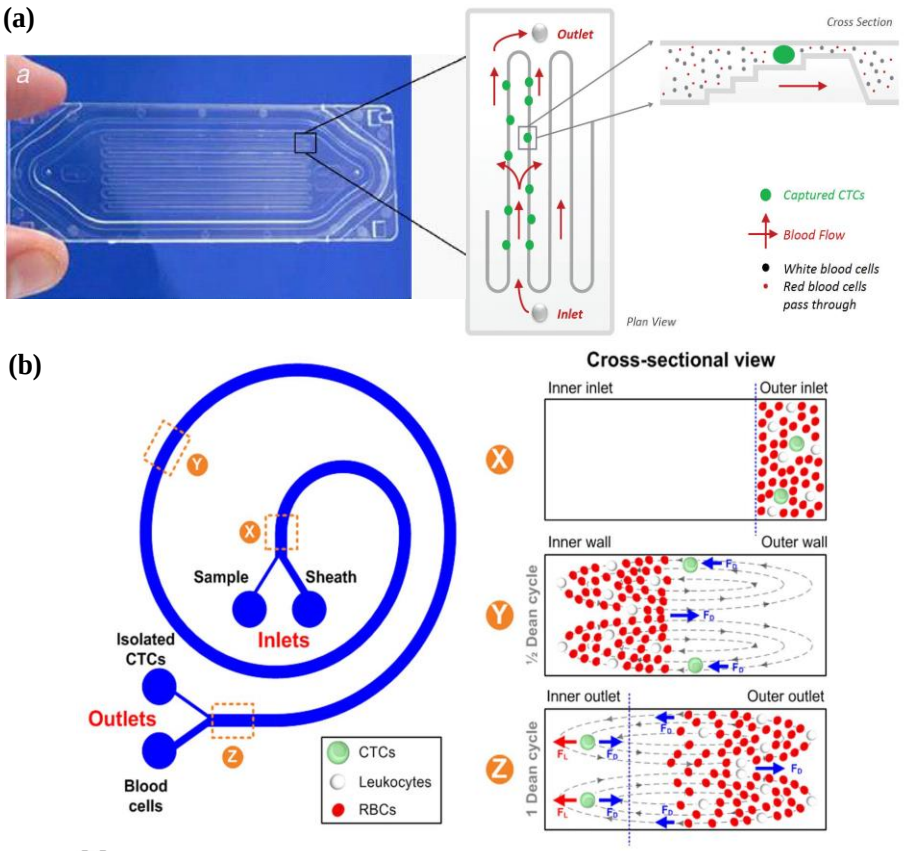

Fig. 1.7 Schematic of microfluidics chips for CTCs enrichment (a) Parsotix stepped microchannel(ANGLE, 2019, Hvichia et al., 2016) can retain and release CTCs by a stepped design microchannel and a reverse flow. (b) Dean Flow Fractionation (DFF) spiral microchannel(Hou et al., 2013) uses DFF within a spiral microchannel to enrich CTCs from normal blood cells.

Centrifugation is one of the earliest reported CTCs enrichment methods from blood samples based on the density difference of cells, and it develops to the current density-based gradient centrifugation(Bankó et al., 2019). Similarly, the OncoQuick® (GrenierBioOne, Frickenhausen, Germany) tube has been designed and applied for CTC enrichment with enrichment medium and a porous barrier allowing blood cells to pass but blocking the CTCs(Greiner, 2021). For a whole enrichment process, the OncoQuick tube is filled with samples and centrifuged. After the centrifugation, the enrichment medium with a larger density than serum remains at the bottom side, and the CTCs and platelets can be enriched between the medium and serum. A CTC detection rate of only 23% was reported by using OncoQuick® to test samples from 61 metastatic cancer patients(Balic et al., 2005). By implementing extra components, the AccuCyte® system provides an improved density-based CTC enrichment method(Campton et al., 2015). Within two centrifugations AccuCyte® system uses a float and EpiCollector™ for cell stratification and automatic collection, respectively. The whole enrichment process is indicated in Fig. 1.8 b. Blood is added into the tube with a float for the first centrifugation to separate plasma and blood cells. After the plasma is aspirated, the high-density fluid is added into the tube with a sealing ring. Finally, the EpiCollector™ and a transfer tube are inserted, followed by the second centrifugation to collect the buffy coat cells in the transfer tube (a fluid switching process). It showed a similar CTC detection efficiency compared with CellSearch® when dealing with clinical samples from breast, prostate and colorectal cancer patients(Campton et al., 2015).

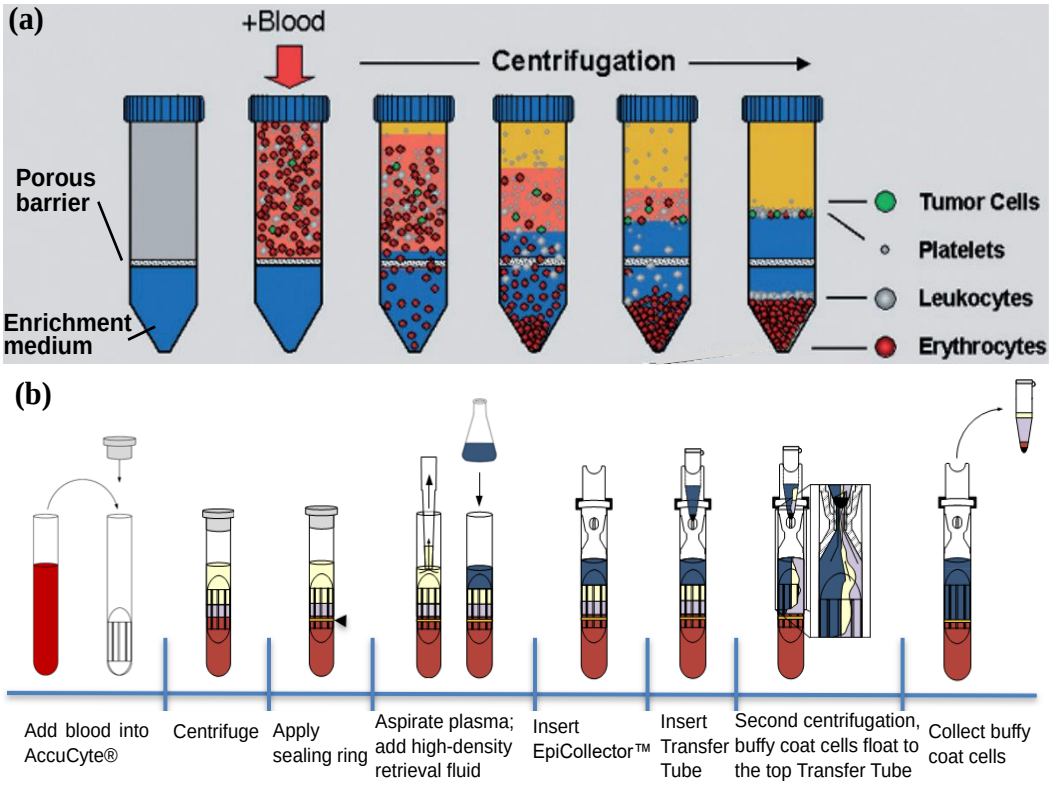

Fig. 1.8 Schematic of density-based CTCs enrichment (a) OncoQuick®(Greiner, 2021) applied a porous membrane allowing blood cells to pass in density-based gradient centrifugation for CTCs enrichment (b) AccuCyte®(Campton et al., 2015) develops a novel float and a medium auto-switching part to enrich CTCs after two centrifugation.

Although these biophysical property-based approaches can provide effective biomarker independent CTCs capture and enrichment, which is friendly to downstream analysis, there are still some challenges. The driving pressure of the high throughput microfilters can lead to clogging of the device, and the increased pressure can damage the captured cells, thus decreasing the number of cells harvested(Hvichia et al., 2016). As to the size-based microfluidic CTCs sorting, the size overlap between CTCs and healthy blood cells, especially leukocytes, can lower the samples purity to increase the noise seen in detailed gene analysis and fluorescent imaging analysis(Bankó et al., 2019). Density-based centrifugation techniques also face a similar challenge: leukocyte contamination can result in

significantly low purity of enriched CTCs(Ferreira et al., 2016). In summary, biophysical-based approaches can achieve label-free and cell-unmodified CTCs capture, which is friendly for downstream analysis, and decrease the chance of CTCs loss in the immuno-dependent methods. It is desired for clinical application of CTCs in cancer screening.

1.3 Thesis outline

This thesis describes the CR fabrication methods and experimental set-up of SAW-based acoustofluidic devices for cells manipulation. The clinical application of the devices has been investigated in cell washing and cancer cell separation. Optimisation of the acoustofluidic devices is demonstrated by developing a novel FTA IDT design and applying gallium nitride substrates, respectively. The structure of the thesis is briefly outlined below.

Chapter 1 describes the motivation and aim of this project: CTCs detection by acoustofluidic devices and introduces the background of CTCs detection.

Chapter 2 introduces the background of acoustofluidics manipulation, the theory of surface acoustic wave (SAW)-based manipulation and various application of acoustofluidics manipulation of cells.

Chapter 3 presents the design and fabrication of SAW-based acoustofluidic devices with CR facilities and the whole experimental set-up for the following experimental work. Conventional IDT design and Novel FTA IDT design are both demonstrated. The detailed CR fabrication process of acoustofluidics devices is described with the proper response to the environmental changes. Portions of this chapter were published as listed below with a description of the contribution from the thesis author.

- Wu, F., Shen, M.H., Yang, J., Wang, H., Mikhaylov, R., Clayton, A., Qin, X., Sun, C., Xie, Z., Cai, M. and Wei, J., 2021. An Enhanced Tilted-Angle Acoustofluidic Chip for Cancer Cell Manipulation. IEEE Electron Device Letters, vol. 42, no. 4, pp. 577-580, DOI: 10.1109/LED.2021.3062292
  Contribution: design and fabrication of the CTA and FTA device, all the experimental work, writing of the manuscript.
- Mikhaylov, R., Wu, F., Wang, H., Clayton, A., Sun, C., Xie, Z., Liang, D., Dong, Y., Yuan, F., Moschou, D. and Wu, Z., 2020. Development and characterisation of acoustofluidic devices using detachable electrodes made from PCB. Lab on a Chip, 20(10), pp.1807-1814, DOI: 10.1039/c9lc01192g
  Contribution: experimental work via conventional parallel IDT device. part of the IDT design.
- Sun, C., Mikhaylov, R., Fu, Y., Wu, F., Wang, H., Yuan, X., Xie, Z., Liang, D., Wu, Z. and Yang, X., 2020. Flexible Printed Circuit Board as Novel Electrodes for Acoustofluidic Devices. IEEE Transactions on Electron Devices, 68(1), pp.393-398, DOI: 10.1109/TED.2020.3039760. chapter 3
  Contribution: design of the microchannel, part of the device set-up design.

Chapter 4 studies the relation between electrical input power and cell-mimic microparticles behaviours in the acoustofluidic field. The numerical and experimental investigation for four polystyrene particle sizes, 5 μm, 10 μm, 15 μm and 20 μm are studied and compared.

Chapter 5 presents the work that applies the acoustofluidic platform in cell washing applications. The cells after electroporation are deflected and separated from the original medium, which improves electroporation efficiency and cell viability.

Chapter 6 introduces a novel FTA IDT design and comparisons with the CTA design to prove the optimisation to acoustofluidic devices. Hela cancer cells and peripheral blood mononuclear cells (PBMCs) are used to investigate the possibility to separate cancer cells via the acoustofluidic device using FTA design. Portions of this chapter were published as listed below with a description of the contribution from the thesis author.

- Wu, F., Shen, M.H., Yang, J., Wang, H., Mikhaylov, R., Clayton, A., Qin, X., Sun, C., Xie, Z., Cai, M. and Wei, J., 2021. An Enhanced Tilted-Angle Acoustofluidic Chip for Cancer Cell Manipulation. IEEE Electron Device Letters, vol. 42, no. 4, pp. 577-580, DOI: 10.1109/LED.2021.3062292
  Contribution: design and fabrication of the CTA and FTA device, all the experimental work, writing of the manuscript.

Chapter 7 presents the optimisation of acoustofluidics devices by substituting the

substrate materials from conventional lithium niobate to gallium nitride. The related numerical simulation and cells manipulation work is demonstrated. Portions of this chapter were published as listed below with a description of the contribution from the thesis author.

- Sun, C., Wu, F., Wallis, D.J., Shen, M.H., Yuan, F., Yang, J., Wu, J., Xie, Z., Liang, D., Wang, H. and Tickle, R., 2020. Gallium nitride: A versatile compound semiconductor as novel piezoelectric film for acoustic tweezer in manipulation of cancer cells. IEEE Transactions on Electron Devices, 67(8), pp.3355-3361, DOI: 10.1109/ted.2020.3002498.
  Contribution: design of the device set-up and microchannel, part of the experimental work.

- Sun, C., Wu, F., Fu, Y., Wallis, D.J., Mikhaylov, R., Yuan, F., Liang, D., Xie, Z., Wang, H., Tao, R. and Shen, M.H., 2020. Thin film Gallium nitride (GaN) based acoustofluidic Tweezer: Modelling and microparticle manipulation. Ultrasonics, 108: 106202, DOI: 10.1016/j.ultras.2020.106202.
  Contribution: design of the device set-up and microchannel, part of the experimental work.

Chapter 8 summarizes the conclusions from each chapter and discusses future research.

Chapter 2 Acoustofluidics manipulation

Acoustofluidics is a technique combining acoustics with microfluidics which investigates acoustic waves and their interaction with different interfaces in micro or nano meter scales. This project only focuses on the part of acoustofluidics application that uses surface acoustic waves (SAWs) based acoustofluidics devices to achieve particle and cell manipulation only depending on their physical properties(Laurell et al., 2007, Petersson et al., 2007, Lenshof et al., 2012b). Acoustics originally represented the pressure variations in an elastic medium, such as air, water and solids, that can be detected by the human ear with a frequency between 20 Hz and 20 kHz. Nowadays, acoustics research has been expanded with a greater frequency scale, such as ultrasound (from 20 kHz to 1 GHz) and infrasound (below 20 Hz). On the other hand, microfluidics is “the science and technology of systems that proceed or manipulates small amounts of fluids using channels with dimensions of tens to hundreds of micrometres”(Squires and Quake, 2005). Microfluidics can achieve a well-controlled microenvironment for manipulating fluids and particles(Ren et al., 2013).

Many experiments have been carried out to prove the theoretical hypothesis of the phenomena that appear in acoustofluidics particles manipulation, such as the channel resonances and particle motion by acoustic radiation force(Barnkob et al., 2010, Augustsson et al., 2011), and an acoustic force and pressure measurement by using optical trapping(Lakämper et al., 2015). This chapter aims to introduce the background of SAW-based acoustofluidics manipulation techniques and current acoustofluidics manipulation research and their applications.

2.1 Surface acoustic wave (SAW)

A surface vibration can generate a sound wave characterised by the amplitude of pressure variations, wavelength (λ) and frequency (f). The amplitude of pressure variation always indicates the energy carried by the sound wave. Wavelength describes the wave travelling distance within one pressure variation cycle while frequency indicates the number of cycles per unit time, such as that per second is called Hertz (Hz). Moreover, the period (T) represents the time for the wave to pass a fixed point as a cycle. In addition, the speed of sound (c) is related to the frequency (f) and wavelength (λ) by $c = f\lambda$, and it varies when travelling in different mediums or environments (e.g., temperature and pressure).

Lord Rayleigh firstly researched surface acoustic waves (SAWs) in 1885(Rayleigh, 1885), where acoustic waves propagate near the surface of a substrate. As an elastic wave, SAW has a slow decay with propagating due to its propagation mode(Gedge and Hill, 2012). Rayleigh waves and Love waves are the two main types of SAWs(Everett, 2013), and the most obvious difference between them is their propagation, shown in Fig. 2.1 a and b, respectively. The surface particles motion of Rayleigh waves is in an elliptical path on a surface perpendicular to the substrate surface. In contrast, Love waves move in a horizontal and transverse direction to the wave propagation(Everett, 2013).

Furthermore, Rayleigh waves can present on any free surface while Love waves typically need an added overlayer as a waveguide and only bring shear stresses due to its vibration mode(Kovacs et al., 1992). With about only one wavelength of wave penetration in-depth, most of the energy of Rayleigh waves remains along the propagation surface(Gedge and Hill, 2012). In addition, there are also some other types of SAW, such as shear horizontal SAW (SH-SAW), surface transverse wave

(STW) and surface skimming bulk wave (SSBW). They have been used for different sensing and transducing application by their identical surface particle motion and propagation mode (Manohar, 2012).

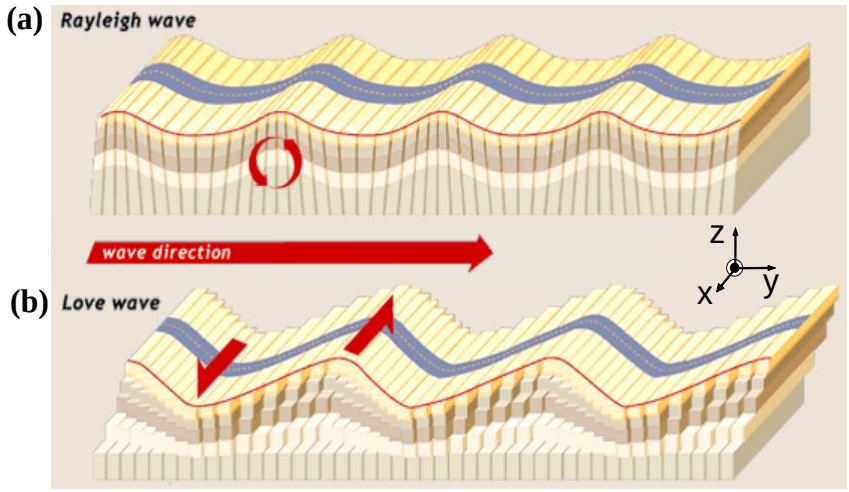

Fig. 2.1 Schematic of the two types of surface acoustic waves (SAWs) propagation (a) Rayleigh waves(Exploratorium, 2021) have a two-dimensional elliptical surface particle motion vertical to the propagating surface. (b) Love waves(Exploratorium, 2021) move in a horizontal and transverse direction to the wave propagation

Compared with SAW, bulk acoustic wave (BAW) is another type of acoustic wave which propagates through the substrate and has also been applied in some acoustofluidics applications(Xie et al., 2019). BAW-based devices usually employ the microchannel to be part of the system, whose operation relies on the acoustic transducer and the property of the microchannel material(Skov and Bruus, 2016). SAW-based acoustofluidic devices are compact and easy to fabricate for high-frequency applications (MHz – GHz) (Gedge and Hill, 2012). They are versatile and less dependent on the acoustic property of the microchannel when compared to those made using BAWs, thus showing good performance(Nama et al., 2015). Moreover, the energy of BAW can dissipate into the microfluidic structure in an acoustofluidic device(Muller et al., 2012). In contrast, the energy of SAW is mostly retained on the

substrate surface and leads to efficient energy usage(Nama et al., 2015). The energy profile of SAW proportionally varies by the depth of penetration, defined by $e^{-2\pi\frac{y}{\lambda}}$, where y is the depth from the surface of substrate and λ is the SAW wavelength(Kirschner, 2010).

In SAW-based acoustofluidic devices, a standing acoustic wave is normally used for precisely acoustofluidic manipulation due to its higher working frequency(Gedge and Hill, 2012). A standing surface acoustic wave (SSAW) is a vibrational pattern created on the medium surface as a superposition result of the interaction between two counter-propagating acoustic waves with the same frequency. In Fig. 2.2, it is shown that the SSAW generation from two opposite SAW sources during a half period (t_0 ~ t_4) (Wikimedia, 2021). t_0 is the initial state, and there is an increase of 1/8 of the period till t_4. from t_0 to t_4, the positions where the amplitude remains zero are named pressure nodes (PNs). In contrast, the locations where the amplitude varies with a maximum absolute value are named pressure antinodes (ANs). At t_0 and t_4, the two opposite SAWs coincide and form the wave with the highest amplitude, enhancing energy. Since the positions that have the maximum amplitude or remaining non-vibration are fixed in an SSAW, the SSAW-based acoustofluidics can provide precisely cells manipulation.

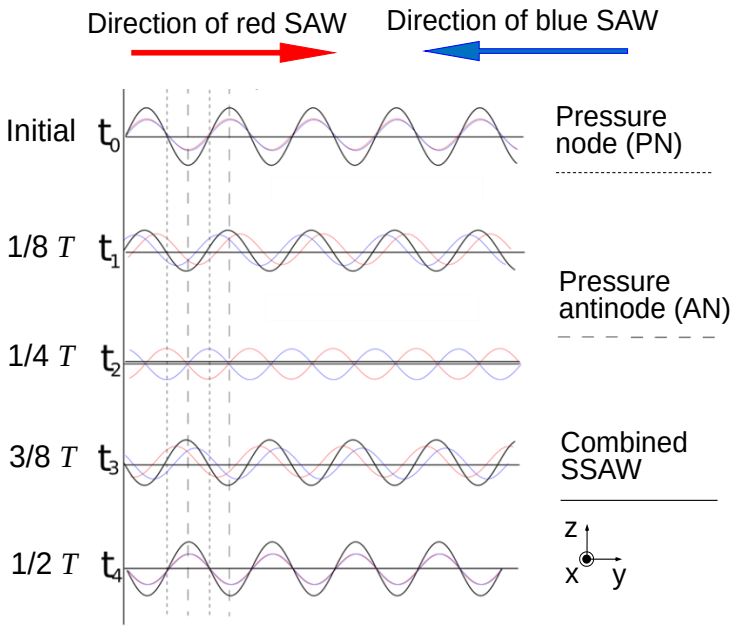

Fig. 2.2 Schematic(Wikimedia, 2021) of standing surface acoustic wave (SSAW) generation within a half period ($t_0 \sim t_4$). PNs are the positions that remain 0 amplitude of the combined SSAW. Those places with varying maximum absolute values of amplitude are pressure antinodes (ANs).

2.2 Generation of SAW

SAW is typically generated by an inter-digital transducer (IDT) consisting of piezoelectric materials patterned with inter-digital electrodes (IDEs) working at ultrasonic frequencies. As shown in Fig. 2.3, the combination of both positive and negative electrodes produces the electric field on the piezoelectric substrate, where a periodic expansion and compression strain is generated. The accumulated strain forms the SAW propagating from the input IDT in a longitudinal and transverse direction and travelling along the piezoelectric substrate surface(Fall et al., 2018).

Converse piezoelectricity plays an important role in SAW generation. It describes that

material expansion and compression occur in piezoelectric materials when a charge with potential is applied. The converse piezoelectricity can be described by(Sirohi and Chopra, 2000)

$$\varepsilon_k = d_{jk}E_j + S_{km}\sigma_m, \tag{2.1}$$

where ε is the induced strain, and *E* is the applied electric field (Volt/m), σ_m is the stress (N/m^2), d_{jk} and S_{km} are the constants of the piezoelectric coefficient (m/Volt) and the elastic compliance (m^2/N), respectively. Among these parameters, the piezoelectric coefficient d_{jk} indicates the strain produced per unit electric field applied at constant stress, where the first and second subscript is the direction of an applied electrical field and the induced strain, respectively. Due to the IDE patterned position and the required SAW vibration direction, as shown in Fig. 2.3, d_{33} is one of the key factors to piezoelectric material selection for SAW generation devices, which means the applied electric field is parallel to the direction of the induced strain. Another key factor is the electromechanical coupling coefficient k^2 that is defined as(Ltd) $k^2 = \frac{Mechanical\ energy\ stored}{Electrical\ energy\ applied} = \frac{Electrical\ energy\ converted\ to\ mechanical\ energy}{Input\ of\ electrical\ energy}$

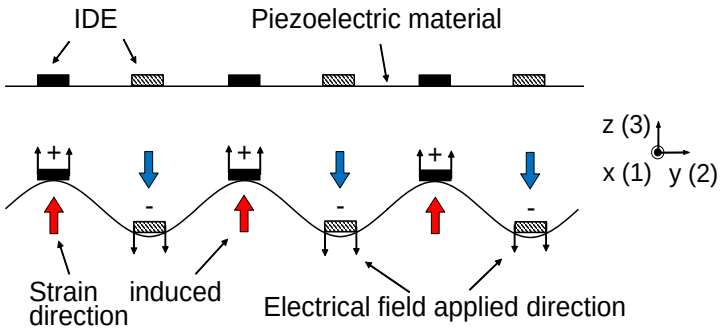

Fig. 2.3 IDEs are patterned on piezoelectric material to generate SAW where the direction of the applied electric field and the induced strain are the same/parallel. 1,2, and 3 represents the direction in the Cartesian reference frame.

Several popular piezoelectric materials are potentially suitable for SAW generation, and their key properties are shown in Table. 2.1. Quartz (SiO_2), lithium tantalate ($LiTaO_3$), lithium niobate ($LiNbO_3$) and langasite has been considered according to their acoustic wave velocity v_p, piezelectric coefficient d_{33}, the electromechanical coupling coefficient k^2 and thermal conductivity. 128° Y - Cut $LiNbO_3$ has the highest efficiency from electrical energy to the amplitude of SAW vibration. At the same time, its lower thermal conductivity (the ability to transfer/conduct heat) compared with SiO_2 and $LiTaO_3$ indicates that an efficient cooling system is necessary to prevent damaging device and manipulated biological samples. In terms of the acoustic wave velocity, it relates to the working frequency of the SAW devices. In conclusion, the 128° Y - Cut $LiNbO_3$ is the most suitable piezoelectric substrate for SAW generation.

Table. 2.1 Properties of piezoelectric materials for SAW generation

Piezoelectric material for SAW	v_p (m/s)	d_{33} (pm/Volt)	k^2 (%)	Thermal conductivity (W/m°K)	References
Quartz (SiO_2)	3159	2.3	0.16	10	(Chin, 2006, Zaszczyńska et al., 2020)
X - Cut Lithium Tantalate ($LiTaO_3$)	3290	1.93	0.75	4.6	(Chin, 2006, Roditi.com, Dmphotonics.com)
128° Y - Cut Lithium Niobate ($LiNbO_3$)	3980	16	5.5	4.4	(Chin, 2006, Zaszczyńska et al., 2020, Bostonpiezooptics.com, Roditi.com)
Langasite	2330	6.5	0.37	1.9	(Chin, 2006, Kugaenko et al., 2012, Miracrys.com, 2021)

The first IDT for the SAW device was successfully built on a $LiNbO_3$ substrate in

1969(Tancrell et al., 1969). A typical IDT structure consists of a pair of busbars with extended electrodes parallel and evenly distributed between them, as shown in Fig. 2.4. There are several parameters to consider when designing the IDE pattern on the piezoelectric substrate to create the inter-digital transducer (IDT). Firstly, the frequency of the generated SAW relies on the synchronous frequency of the device. To achieve the maximum transduction (electrical energy to mechanical vibration) efficiency, the frequency of the input signal should be the same as the synchronous frequency(Kirschner, 2010), f_0, which is determined by the pitch p of the IDT fingers (shown in Fig. 2.4), given by,

$$f_0 = \frac{v_\mathrm{p}}{p} \tag{2.2}$$

where v_p is the propagation velocity of a wave in the substrate. Secondly, the bandwidth of the SAW frequency generated by the IDTs is

$$BW = \frac{2f_0}{N} \tag{2.3}$$

where N is the number of pairs of fingers in the IDT. By substituting Equation 2.2 to 2.3, the bandwidth BW can also be described as:

$$BW = \frac{2}{Np} v_\mathrm{p} = 2\frac{v_\mathrm{p}}{l_\mathrm{IDT}} \tag{2.4}$$

where l_IDT is the total length of IDT parallel with the SAW propagation direction.

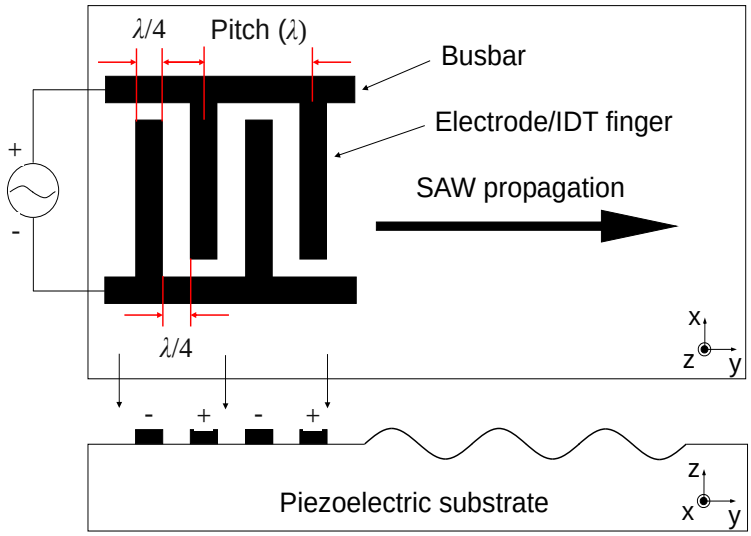

Fig. 2.4 Schematic of the top and side views of SAW generated by an IDT device.

2.3 Theory of SAW-based acoustofluidics manipulation of particles and cells

Based on the inverse piezoelectric effect, the SAW is generated and propagated along a piezoelectric substrate, and is interfered with fluid in a microchannel. The acoustic energy is radiated into the fluid, which leads to acoustic streaming of the fluid and particle motion inside the microchannel. When the particles enter the SAW field in the channel, they experience the acoustic radiation force $\boldsymbol{F}^{\mathrm{rad}}$ and the Stokes drag force $\boldsymbol{F}^{\mathrm{drag}}$ due to the acoustic streaming as shown in Fig. 2.5.

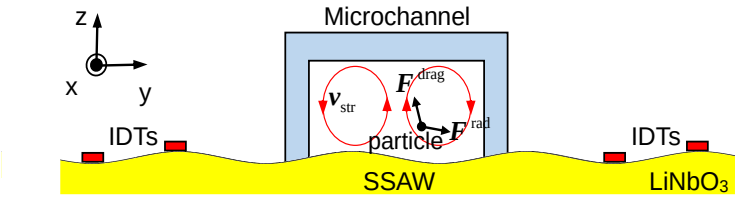

Fig. 2.5 The total force exerted on the microparticle inside the acoustic microchannel is the combination of the acoustic radiation force $\boldsymbol{F}^{\mathrm{rad}}$ and Stokes drag force $\boldsymbol{F}^{\mathrm{drag}}$.

To determine the time-averaged acoustic radiation force $\boldsymbol{F}^{\mathrm{rad}}$ on a spherical particle, which leads to the net movement of the particles besides local oscillation, the first order acoustic pressure $\hat{p}_1$ and velocity $\hat{\boldsymbol{v}}_{\boldsymbol{1}}$ need to be obtained. According to the Navier-Stokes equation, the governing equations describing the conservation of momentum and the continuity for the bulk fluid flow are(Nama et al., 2015),

$$\frac{\partial \hat{\rho}}{\partial t} = -\boldsymbol{\nabla} \cdot (\hat{\rho}\hat{\boldsymbol{v}}) \tag{2.5}$$

$$\hat{\rho}\frac{\partial \hat{\boldsymbol{v}}}{\partial t} = -\boldsymbol{\nabla}\hat{p} - \hat{\rho}(\hat{\boldsymbol{v}} \cdot \boldsymbol{\nabla})\hat{\boldsymbol{v}} + \eta\boldsymbol{\nabla}^2\hat{\boldsymbol{v}} + \beta\eta\boldsymbol{\nabla}(\boldsymbol{\nabla} \cdot \hat{\boldsymbol{v}}) \tag{2.6}$$

$$\beta = \frac{\eta_{\mathrm{b}}}{\eta} + \frac{1}{3} \tag{2.7}$$

where $\hat{\rho}$, $\hat{\boldsymbol{v}}$, $\hat{p}$, η, η_{b} are the fluid density, fluid velocity, fluid pressure, shear viscosity and bulk viscosity, respectively. By defining the equilibrium fluid density and pressure as zeroth-order state ρ_0 and p_0, the different fields can be expressed as,

$$\hat{p} = p_0 + \hat{p}_1 + \hat{p}_2 + \cdots \tag{2.8}$$

$$\hat{\rho} = \rho_0 + \hat{\rho}_1 + \hat{\rho}_2 + \cdots \tag{2.9}$$

$$\hat{\boldsymbol{v}} = \hat{\boldsymbol{v}}_{\boldsymbol{1}} + \hat{\boldsymbol{v}}_{\boldsymbol{2}} + \cdots \tag{2.10}$$

The orders above two are neglected, while the first-order term is used for the following calculation. $\hat{p}$ is approximated to be proportional to $\hat{\rho}$,

$$\hat{p}_1 = c_0^2 \hat{\rho}_1 \tag{2.11}$$

where c_0 is approximately equal to the value of the speed of sound in the fluid as a constant. After substituting the above equations, and combining the derived Eq. 2.5 and Eq. 2.6 for the first-order terms, the governing equation for $\hat{p}_1$ and $\widehat{\boldsymbol{v}}_\mathbf{1}$ can be described as

$$\frac{\partial^2 \hat{p}_1}{\partial t^2} = c_0^2 \left[1 + \frac{(1+\beta)\eta}{\rho_0 c_0^2} \frac{\partial}{\partial t}\right] \boldsymbol{\nabla}^2 \hat{p}_1 \tag{2.12}$$

$$\rho_0 \frac{\partial \widehat{\boldsymbol{v}}_\mathbf{1}}{\partial t} = -c_0^2 \boldsymbol{\nabla} \hat{\rho}_1 + \eta \boldsymbol{\nabla}^2 \widehat{\boldsymbol{v}}_\mathbf{1} + \beta\eta \boldsymbol{\nabla}(\boldsymbol{\nabla} \cdot \widehat{\boldsymbol{v}}_\mathbf{1}) \tag{2.13}$$

By assuming the first-order terms to be harmonic time dependence, the p_1 and $\boldsymbol{v}_\mathbf{1}$ can be obtained by,

$$\left[1 + \frac{\mathrm{i}\omega(1+\beta)\eta}{\rho_0 c_0^2}\right] \boldsymbol{\nabla}^2 p_1 + \frac{\omega^2}{c_0^2} p_1 = 0 \tag{2.14}$$

$$\boldsymbol{v}_\mathbf{1} = -\frac{\boldsymbol{\nabla} p_1}{\mathrm{i}\omega\rho_0}\left[1 + \frac{\mathrm{i}\omega(1+\beta)\eta}{\rho_0 c_0^2}\right] \tag{2.15}$$

where $\omega = 2\pi f$ is the angular frequency, and f is the SAW frequency. The time-averaged acoustic radiation force $\boldsymbol{F}^{\mathbf{rad}}$ is combined with the second-order pressure and the first-order momentum flux on a spherical particle surface. Settnes and Bruus (2012) have derived the radiation force, when the particle radius is much smaller than the wavelength, as,

$$\boldsymbol{F}^{\mathbf{rad}} = -\pi a^3 \left[\frac{2\kappa_0}{3}\mathrm{Re}(f_1^* p_1^* \boldsymbol{\nabla} p_1) - \rho_0 \mathrm{Re}(f_2^* \boldsymbol{v}_1^* \boldsymbol{\nabla} \boldsymbol{v}_1)\right] \tag{2.16}$$

where a, κ_0, f_1 and f_2 are the particle radius, the isentropic compressibility of the fluid and the scattering coefficients, respectively. The complex conjugate of the quantity is represented as the asterisk ($*$).

Stokes drag force $\boldsymbol{F}^{\mathbf{drag}}$ is another type of force experienced by the particles from the particles relative motion to the viscous fluid. The time-averaged $\boldsymbol{F}^{\mathbf{drag}}$ can be described as

$$\boldsymbol{F}^{\mathbf{drag}} = 6\pi\eta a(\langle \hat{\boldsymbol{v}}_2 \rangle - \boldsymbol{v}_{\mathrm{p}}) \tag{2.17}$$

where $\boldsymbol{v}_{\mathrm{p}}$ and $\langle \hat{\boldsymbol{v}}_2 \rangle$ are the particle velocity vector and the time-averaged streaming velocity. Applying Newton's second law of motion to the particles inside the channel yields,

$$m_{\mathrm{p}} \frac{d\boldsymbol{v}_{\mathrm{p}}}{dt} = \boldsymbol{F}^{\mathbf{rad}} + \boldsymbol{F}^{\mathbf{drag}} \tag{2.18}$$

where m_{p} is the mass of the particle. The acceleration term in Eq. 2.18 can be neglected because of the much shorter particle acceleration time than most experimental observations. Thus, the velocity of the particles $\boldsymbol{v}_{\mathrm{p}}$ can be calculated by,

$$\boldsymbol{v}_{\mathrm{p}} = \langle \hat{\boldsymbol{v}}_2 \rangle + \frac{\boldsymbol{F}^{\mathbf{rad}}}{6\pi\eta a} \tag{2.19}$$

The $\langle \hat{\boldsymbol{v}}_2 \rangle$ can be determined by the boundary conditions, and applied for further simulation, such as particles trajectories along the channel.

The acoustic radiation force $\boldsymbol{F}^{\mathrm{rad}}$ can be sub-categorised as primary and secondary radiation force representing the force directly from the acoustic field and the force

induced from particles interaction, respectively(Doinikov, 2003). In this thesis, due to the SSAW stimulation and application scenarios, only the primary radiation force is considered, which results in particle migration towards PNs or ANs(Shi et al., 2009). The secondary radiation force is normally used for particles or cells aggregation research(Wu et al., 2019b). As shown in Fig. 2.5, the SSAWs generate periodic pressure fluctuations in the fluid inside the microchannel, which induce acoustic radiation force $\boldsymbol{F}^{\mathrm{rad}}$ that drives microparticles either towards the PNs or ANs, which depends on the sign of the acoustic contrast factor $\phi(\rho,\beta)$ (ϕ>0 – moving towards PNs, ϕ<0 – moving towards ANs). On the y-z plane which is perpendicular to the IDT finger electrodes orientation, for a plane standing wave made from horizontal sinusoidal waves, $\boldsymbol{F}^{\mathrm{rad}}$ can be denoted as:

$$\boldsymbol{F}^{\mathrm{rad}} = -\left(\frac{\pi p_0^2 V_{\mathrm{p}} \beta_{\mathrm{f}}}{2\lambda}\right) \phi(\rho,\beta) \sin(2ky) \tag{2.20}$$

$$\phi(\rho,\beta) = \frac{5\rho_{\mathrm{p}} - 2\rho_{\mathrm{f}}}{2\rho_{\mathrm{p}} + \rho_{\mathrm{f}}} - \frac{\beta_{\mathrm{p}}}{\beta_{\mathrm{f}}} \tag{2.21}$$

where p_0, V_{p}, β_{f}, ϕ, k, y, ρ_{p}, ρ_{f}, and β_{p} are the acoustic pressure, the volume of the microparticle, compressibility of the fluid, SAW wavelength, wave number, distance from a PN in the y-axis, density of the fluid, the density of the microparticle and compressibility of the microparticle, respectively. The acoustic radiation force will drive microparticles with a positive acoustic contrast factor towards the PNs. In contrast, microparticles with a negative contrast factor will be driven towards the ANs. Polystyrene microspheres used in this project have a positive acoustic contrast factor which drives them towards the PNs. The acoustic pressure is estimated by(Ding et al., 2014)

$$p_0 = \sqrt{\alpha \frac{P_{in} \rho_{\mathrm{s}} c_{\mathrm{s}}}{A_{\mathrm{w}}}} \tag{2.22}$$

where α, P_{in}, ρ_{s}, c_{s}, and A_{w} are the power conversion factor, input power, density of $LiNbO_3$, phase velocity of SAW in $LiNbO_3$ and working area (IDT length multiplied by the distance between two IDT), respectively. In addition, microparticles are impeded by the Stokes drag force $\boldsymbol{F}^{\mathrm{drag}}$, as described by Eq. 2.17

2.4 Applications of acoustofluidic manipulation

As a powerful tool, acoustofluidics can manipulate micro- or nano-particles and cells with biocompatible, contactless and label-free characteristics(Zhang et al., 2020). Acoustic-based microfluidic devices have been applied in manipulating biological particles such as circulating tumour cells (CTCs)(Li et al., 2015a, Antfolk et al., 2015, Wu et al., 2018b), extracellular vesicles (EVs)(Wu et al., 2017a, Lee et al., 2015), bacteria(Ohlsson et al., 2018, Li et al., 2017, Ohlsson et al., 2016), and inflammatory cells(Li et al., 2016b). According to the function, acoustofluidic manipulation can be classified into particle and cell patterning, focusing, separation and sorting based on different SAW and BAW acoustofluidic devices(Zhang et al., 2020). Deflection rate, removal rate and recovery rate are defined to help identify the cells/particles manipulation performance of the various acoustofluidic devices, as shown in Table. 2.2.

Table. 2.2 Parameters for identifying acoustofluidic device performance of cells/particles manipulation.

Parameter	Definition
Deflection rate	The ratio of target particles, which are efficiently deflected by acoustic force in the microfluidic channel and collected by the non-wasteful outlets, to the target particles that flow through the microfluidic channel.
Removal rate	The ratio of target particles, which are removed from the original samples, to the target particles in the original samples
Recovery rate/ separation efficiency	Similar to removal rate. The ratio of target particles, which are separated from other components in the samples, to the target particles in the original samples.

Acoustic patterning normally uses the acoustic field to manipulate a single or a group of particles or cells at a specific position, or actuate samples to the desired location. For single particle or cell patterning in microscale, an acoustic tweezer (Fig. 2.6a) containing two pairs of opposing IDTs achieves traping and translating samples by Standing SAW within a microchamber(Ding et al., 2012). Down to nanoscale, a BAW-based device successfully creates concentric and rectangular patterns using 5nm diamond nanoparticles within a square reservoir and cylindrical reservoir, respectively(Raeymaekers et al., 2011). Instead of using continuous acoustic wave generation, a micro-particles and cells patterning is demonstrated within a nanosecond-scale pulse of SAW generated from a pair of opposing IDTs (Fig. 2.6b). The patterning position can be readily and arbitrarily modified depending on the pulse delays, frequency modulation and phase shifts(Collins et al., 2016). By generating a standing acoustic wave in a central cavity, cells can be patterned in a commonly used and disposable petri dish(Armstrong et al., 2019), as shown in Fig. 2.6c. A non-spherical shaped nanowire motor (Fig. 2.6d), which is powered by an acoustic field and orientated by a magnetic field, has also been demonstrated to have the ability to flow to the targeting cell controllably(Ahmed et al., 2013).

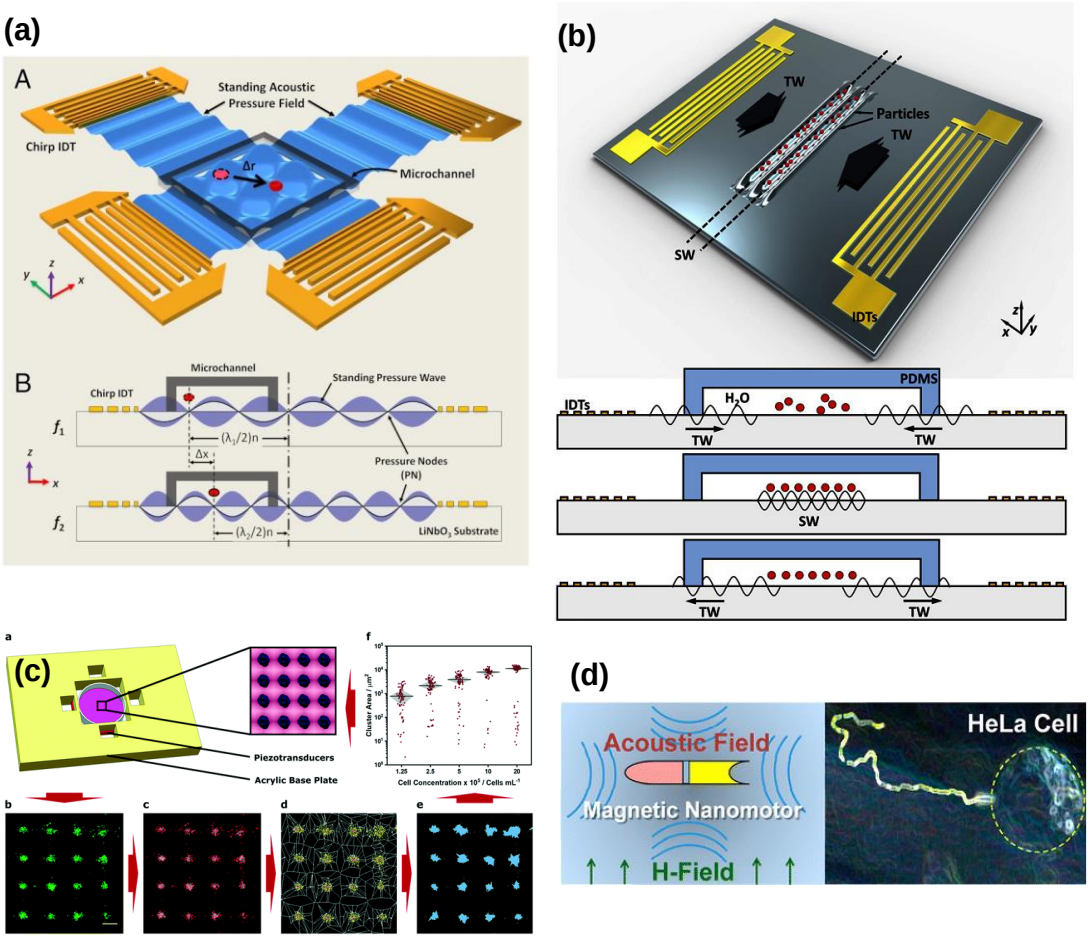

Fig. 2.6 The schematic of different acoustic patterning techniques. (a) an acoustic tweezer applying standing SAW for single microparticles manipulation(Ding et al., 2012). (b) a nanosecond-scale pulse of standing SAW patterns microparticles and cells within a microfluidic channel(Collins et al., 2016). (c) cells are patterned in a disposable petri dish by applying a standing acoustic field(Armstrong et al., 2019). (d) a controllable non-spherical nanowire is powered by the acoustic field and guided by a magnetic field(Ahmed et al., 2013).

Acoustic focusing typically aligns samples along acoustic PNs and replaces the sheath flow that avoids the sample dilution. It has been applied in an SSAW fluorescence-activated cell sorter (FACS) (Fig. 2.7a) where each cell are in a single-line distributed in the downstream laser detection(Ren et al., 2018). For multiple PNs

acoustic focusing (Fig. 2.7b), the multiple cells alignments created by BAW can potentially increase the flow cytometry efficiency when dealing with large particles and high sample volume(Piyasena et al., 2012). Acoustic focusing has also been integrated with commercial FACS platform (stimulated Raman scattering cytometers)(Zhang et al., 2017).

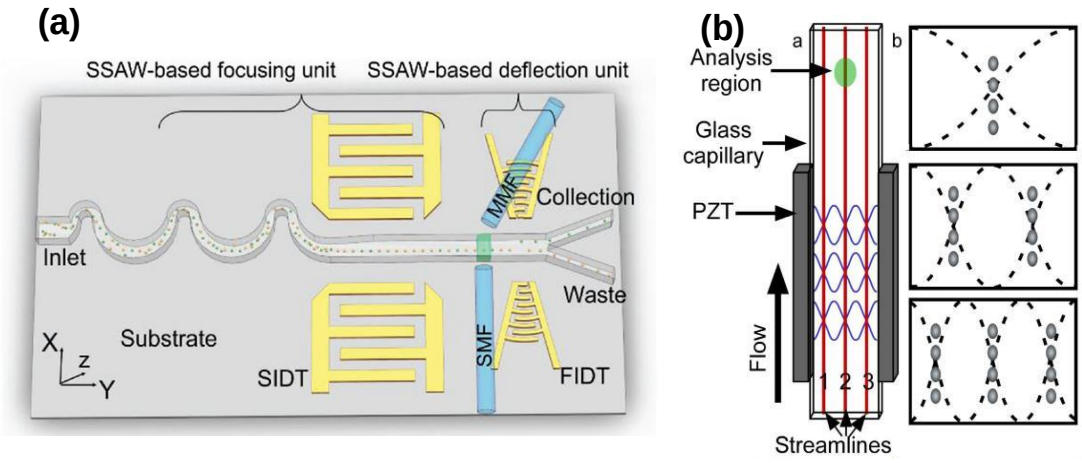

Fig. 2.7 Acoustic focusing based techniques (a) an SSAW FACS utilizes acoustic focusing for an accurate downstream laser detection(Ren et al., 2018). (b) flow cytometry for large-sized cells and sample volume is potentially improved by a multimode acoustic focusing based on BAW(Piyasena et al., 2012).

As to acoustic separation, based on a tilted-angle SSAW device (Fig. 2.8a), CTCs can be separated from breast cancer patient blood with a recovery rate of 83%(Li et al., 2015a). By using a similar acoustofluidic platform, cultured *E. coli* bacterias are mixed with healthy human RBC and separated according to their size differences with collected *E. coli* purity of 96%(Li et al., 2016a). In nanoscale, the EVs separation from healthy human blood has been achieved via a two-stage tilted-angle SSAW device, as shown in Fig. 2.8b(Wu et al., 2017b). The sample is introduced and focused by two sheath flow in the microchannel, and the RBCs, white blood cells and platelet are deflected and separated at the first stage. The EVs are then separated from the

apoptotic bodies and microvesicles at the second stage, where they implement a pair of IDT with a higher working frequency. Moreover, both nano-sized EVs and lipoproteins are successfully separated from each other based on a parallel IDT SSAW device (Fig. 2.8c) according to the difference of their acoustic contrast factor(Wu et al., 2019a). EVs with negative factor are aligned on the ANs while lipoproteins with posive factor on the PNs.

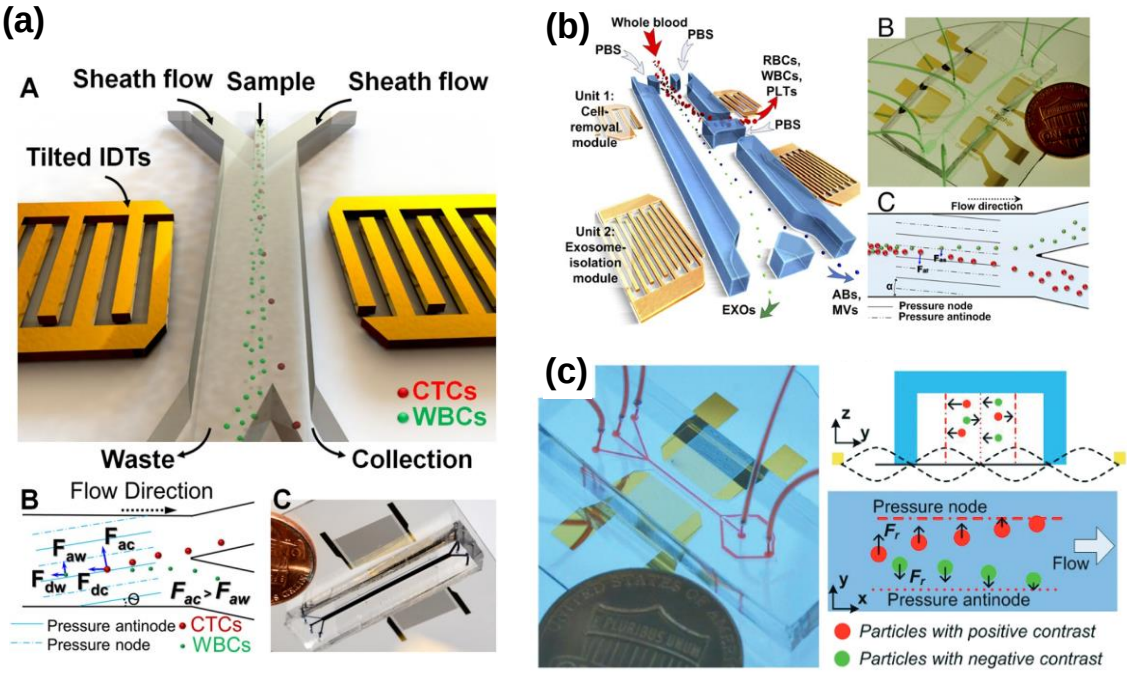

Fig. 2.8 SSAW-based acoustofluidic separation (a) Brest cancer cells are separated from cancer patients blood via a tilted-angle SSAW acoustofluidic device(Li et al., 2015a) (b) a two-stages tilted-angle SSAW device achieved EVs separation from the healthy human whole blood(Wu et al., 2017b). (c) both nanosized EVs and lipoproteins can be separated via acoustofluidics due to their acoustic contrast factor(Wu et al., 2019a).

Besides SSAW separation techniques, the platelet removed from RBC and WBC has been demonstrated based on BAWs acoustofluidic devices (Fig. 2.9a) with an 88.9% blood cell removal rate(Gu et al., 2019). A separation of platelet, RBC and WBC from

undiluted whole blood sample has been reported by lateral cavity acoustic transducers (LCATs) (Fig. 2.9b) depending on the air bubbles acoustic streaming inside microchannel(Garg et al., 2018).

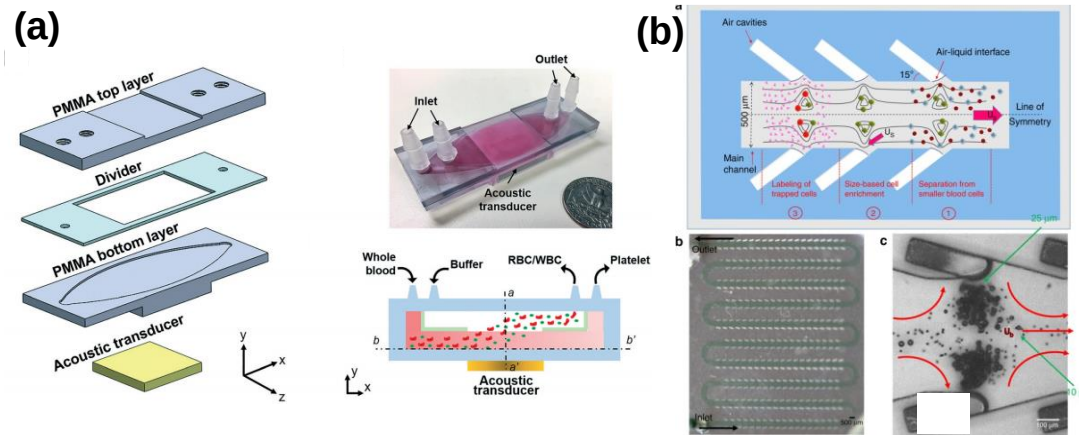

Fig. 2.9 Acoustic separation techniques (a) BAW based platelet separation from RBC and WBC has been demonstrated on a platform with plastic structure(Gu et al., 2019). (b) an LCAT based acoustic streaming device can trap and separate blood components (platelet, RBC and WBC) from the undiluted whole blood(Garg et al., 2018)

Acoustic sorting normally requires a feedback control that triggers acoustic manipulation, especially for single-cell profiling(Zhang et al., 2020), which is different from acoustic separation. Similar to the SSAW-based FACS(Ren et al., 2018), a travelling SAW-based acoustofluidic device (Fig. 2.10a) with a waveguide structure can fluorescently sort labelled mouse melanoma cells with a 330-μs cell deflection duration(Schmid et al., 2014). Moreover, as shown in Fig. 2.10b, an acoustothermal tweezer using spatiotemporally varying thermal stimuli (acoustic streaming and acoustothermal Marangoni effects) causes the lateral migration on droplets in the microfluidic channel, thus achieving the sorting purpose(Park et al., 2017).

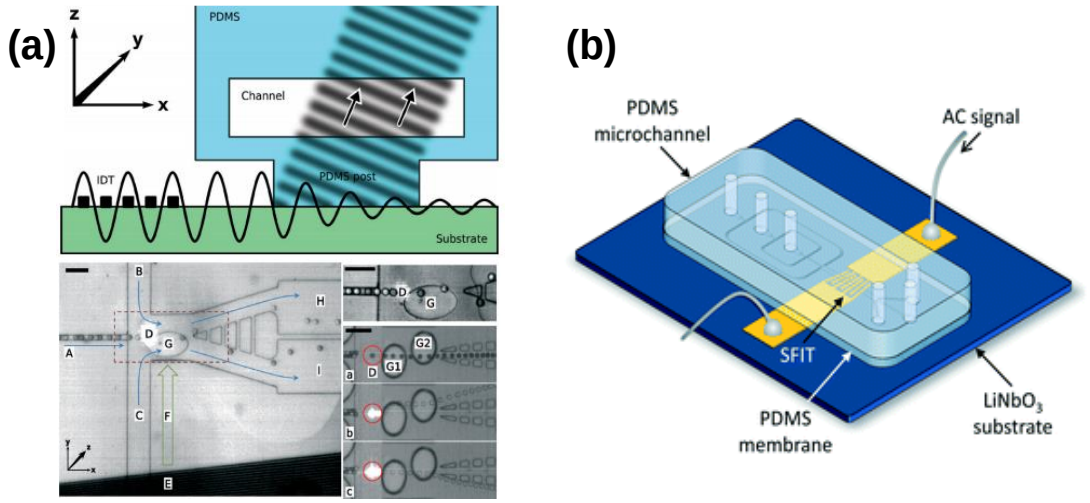

Fig. 2.10 Acoustofluidic sorting techniques (a) a travelling SAW-based cell sorting device can achieve fluorescence labelled mouse melanoma cells sorting with a waveguide structure(Schmid et al., 2014). (b) an acoustothermal tweezer has been reported to achieve droplet sorting based on acoustic streaming and acoustothermal Marangoni effects(Park et al., 2017).

Acoustic manipulation has also been utilised in other applications. For instance, on-chip single and double layer Hela cells coating(Ayan et al., 2016) based on SSAW is effectively achieved, enabling variable applications in chemistry, engineering and medicine. Moreover, acoustofluidic cell washing(Li et al., 2015b) eases the labelling procedure in biological and biomedical research. A novel continuous cell washing method for the various lab-on-chip application is also introduced(Li et al., 2015c). In conclusion, acoustic-based manipulation has great potential in biomedical applications owing to its label-free and biocompatible characteristics.

2.5 Conclusion

This chapter introduces acoustofluidics manipulation from the SAW-based acoustofluidic theory to the systematic review of the current application in recent years. Acoustofluidic manipulations have been applied for fundamental research and clinical

applications that manipulate samples ranging from nanometers to millimetres without special working media that might damage the cells(Xie et al., 2019). Key parameters for identifying the capability of acoustofluidic manipulation devices are demonstrated, including deflection efficiency, removal rate, and recovery rate.

Chapter 3 Design, fabrication and experimental setup of the acoustofluidic cells manipulation devices

This chapter aims to demonstrate the designs, fabrication and experimental setup of the acoustofluidic cells manipulation devices, including IDTs and microfluidic channels and the experimental setup used in this thesis. Fully investigating the whole process of building the devices can help a comprehensive understanding of the devices and develop effective optimisation and innovation to the projects. In this thesis, three types of IDT designs we used, including parallel IDTs, Conventional tilted-angle (CTA) IDTs and Filled tilted-angle (FTA) IDTs, which have their unique features thus have been used for different applications described in the following chapters. The parallel and CTA IDTs are commonly used in various current SSAW-based acoustofluidics research. At the same time, FTA design is a novel development in this thesis with improvements in both saving input energy and providing evenly distributed acoustic field with enhanced acoustic power. The fabrication of the devices with CR facilities follows the standard operation procedure (SOP) developed by the CR of Engineering school of Cardiff University. However, environmental changes, such as temperature and humidity, can impact the fabrication procedure. Therefore, the detailed operation procedures and responses to the unexpected situation have been developed and described in this chapter according to the practical experience. The experimental setup consists of a system control and acoustofluidics platform which employs many mechanical and electrical components for the following cell manipulating experiments.

3.1 The Design of Acoustofluidic Devices

Among the three designs, the parallel design is the basic IDT design suitable for

fundamental research of SSAW-based manipulation. Thus, it was first fabricated for microparticles manipulation test. The CTA design avoids the limitation of microchannels' width by sacrificing the acoustic pressure while handling samples with a large concentration of particles. It was then fabricated for cells manipulation preventing microchannel blockage. In comparison to parallel and CTA design, the FTA design not only avoids the channel width limitation but also saves the acoustic pressure sacrificed by the CTA design. It can also provide a more evenly distributed acoustic field than CTA does. With such advantages, the FTA design was fabricated and used to investigate the cancer cell separation described in chapter 6.

3.1.1 Parallel IDTs device

Parallel IDTs are the devices whose IDT fingers are in parallel with the flow direction in the microchannel. The schematic of the parallel IDT device is shown in Fig. 3.1, consisting of a pair of IDTs and a microchannel bonded onto the substrate between the IDTs. The microchannel's width is designed to be approximately half-wavelength of the SAW to allow the two PNs of the SSAW to be positioned near the two walls of the microchannel, while an AN is formed at the centre. A sample containing microspheres or cells is introduced from the sample inlet with two sheath flows used to control the sample flow width through the flow rate ratio between the sample and sheath. Both IDTs are driven by the same radio frequency (RF) signal to produce rayleigh SSAW. A sample containing microspheres or cells is introduced from the sample inlet; two sheath flows control the sample width entering the acoustic field by setting the flow rate ratio between the sheath and sample. Microspheres or cells dominated and actuated by acoustic radiation force migrate towards PNs and are collected at the two sheath outlets, while other samples are collected from the middle outlet.

There are 40 pairs of finger electrodes on each IDT with the finger width, length and pitch of 50 μm, 1 cm and 200 μm, respectively. The distance between the centre of the first front finger on both IDTs is 3 mm. The working frequency of the IDT is 19.6 MHz identified by S parameter measurement on a vector network analyser (VNA, E5061B ENA, Keysight Technologies, U.K.) and sweeping frequency on a signal generator (RS Pro Arbitrary Waveform Generator), which produces a SAW wavelength of 200 μm. The width of the microchannel inlet, outlet and height is 100 μm, 80 μm and 60 μm, respectively. The width of the middle part (active acoustic area) of the microchannel is 120 μm. The width of the outlet channel increases to 200 μm at the reservoir to stabilise the flow.

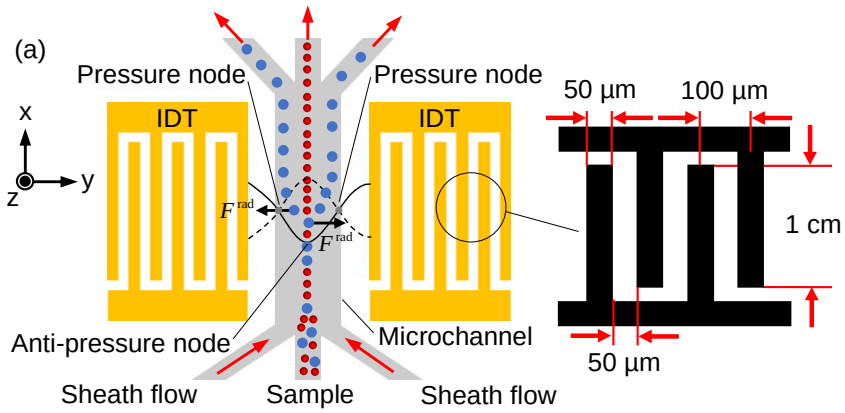

Fig. 3.1 Schematic of the parallel IDTs SSAW device integrating a pair of IDTs and a microfluidic channel, and the dimension of the IDT design. Two opposite IDTs generate SSAW and form PNs where samples are introduced and focused from the inlets are dominated and actuated by acoustic radiation force. Samples migrated to the PNs are collected by the two sheath outlets.

3.1.2 Conventional tilted-angle (CTA) IDT device

The CTA device (Fig. 3.2) is introduced for effective sample manipulation attributing to the establishment of several PN lines orienting inclination (θ) to the flow direction. A wider microchannel (a few times the SAW wavelength), which can accommodate many PN lines, is applied for microspheres, cell manipulations, and separation. A wide channel with three inlets and two outlets is used to minimise the chance of channel blockage caused by the sample deposition and accumulation and allow a larger flowrate and throughput. Once entering the SSAW field in the microchannel, the samples dominated by the acoustic radiation force follow the PNs and are collected in outlet 1.

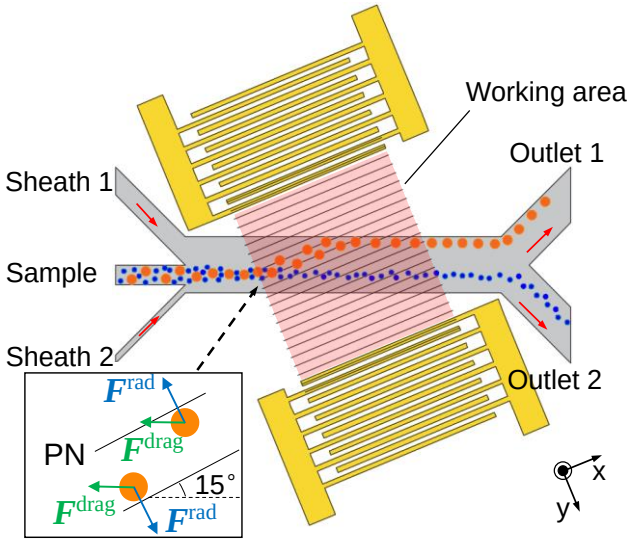

Fig. 3.2 Schematic of the parallel IDTs SSAW device in which the samples are introduced and focused from the inlet. Particles dominated by acoustic radiation force are deflected, followed the PNs and collected in outlet 1 while other particles remain flowing to outlet 2.

The tilted-angle structure brings more consideration of the dimension design. The CTA

IDTs have been designed with the same electrode dimension of the parallel IDTs but with an optimal inclined angle(Ding et al., 2014) of θ=15° to the flow orientation of microchannel which is bonded between the two IDTs with an 800 μm (four times of the wavelength) width and 60 μm height. The value of θ is related to the sample separation distance, and an optimal value (θ=15°) referring to the numerical simulation was investigated by other researchers(Ding et al., 2014). Moreover, the length of the fingers (1 cm) must be long enough for the samples trapped by the tilted PNs to be able to migrate to outlet 1. The width of each inlet and outlet has been designed to fulfil the tilted-angle SSAW manipulation and separation function. The width of sheath 1, sample, sheath 2, outlet 1 and 2 are 400 μm, 300 μm,100 μm, 400 μm and 400 μm, respectively, which allows all the samples to flow below the centerline and to outlet 2 when SSAW is not generated.

According to Eq. 2.20, the acoustic pressure p_0 determines the acoustic radiation force experienced by the particles, and it can be described by Eq. 2.22. The working area A_{w} is calculated as the IDT finger length multiplied by the distance between the two IDTs. Although CTA avoids the wavelength's restriction on the width of the microchannel in parallel IDT design, it creates two empty areas which increase the working area A_{w} thus lower the acoustic pressure is generated compared with parallel IDTs at the same input power P_{in}.

3.1.3 Filled tilted-angle (FTA) IDT device

SSAW can remotely manipulate micro- and nano-objects with high spatial and temporal precisions via the acoustic radiation force F^{rad}. A faster deflection of microparticles can be achieved by increasing the F^{rad} resulting in high-throughput

processing of samples. It has been realised by enhancing acoustic energy density(Sehgal and Kirby, 2017, Wu et al., 2018c, Wu et al., 2018a). For instance, the improvement of the efficiency in a SAW-based microcirculatory system has been achieved by an optimal microchannel structure(Franke and Wixforth, 2008). An enhanced efficiency in acoustic particles focusing has been achieved by decreasing the thickness of the microfluidic device(Ota et al., 2019). Focused(Fakhfouri et al., 2016) and unidirectional(Zhao et al., 2020) IDTs achieved high accuracy and high-throughput separation of micro- and nano-particles. A flow divider in a microchannel streamlined with a glass-SAW device offered effective CTC sorting from the whole blood of prostate cancer patients with a considerably high throughput(Wu et al., 2018c). In addition, a high sample flow rate of up to 500 µl/min was achieved for microparticle separation by applying a novel sheathless microchannel(Wu et al., 2018a). When the mechanical properties of the micro-objects are given, i.e., their size, density and compressibility, further increase of the F^{rad} is desired to speed up the manipulation process. It can be enhanced by optimising the acoustofluidic device parameters, including increasing the acoustic pressure and the SAW frequency(Mao et al., 2016).

In this work, a novel FTA (Fig. 3.3b) SSAW device for enhancing the acoustic pressure by patterning additional IDTs to fill the device space adjacent to the microchannel is developed. This FTA has its unique advantages as an acoustofluidic device for saving its footprint and increasing the acoustic energy density for a better manipulation performance. The CTA device generally exhibits two zones without patterned electrodes (blue triangles in Fig. 3.3a), where no active SAW is generated. As shown in Fig. 3.3b, the FTA device redesigns the IDT pattern by extending the busbars of the electrodes towards the microchannel and patterning additional finger electrodes to occupy these zones, resulting in stronger active SAW generation. The entire FTA finger electrodes are seamlessly following through the microchannel wall to generate

more effective SAW actuation while reducing the attenuation caused by the microchannel and piezoelectric substrate.

For comparative purposes with CTA, FTA devices were developed using similar parameters (θ=15°) except the FTA employed 24 additional finger electrodes to follow through the microchannel. The acoustic pressure p_0 of the device is accordingly increased since the device working area between the two IDTs is reduced (Eq. 2.22) due to adding electrodes. The working areas of the FTA and the CTA devices were 40 mm^2 and 70 mm^2, respectively. The 43% reduction in the working area realised by the added electrodes offers ~32% higher acoustic pressure in the FTA device with the same input power. Since the FTA device employs a smaller working area, producing the same acoustic pressure requires a smaller input power resulting in reduced joule heat. The parameters for CTA and FTA design are shown in Table. 3.1. More detailed investigations of the FTA SSAW device, including numerically and practically comparison with CTA, are described in chapter 6.

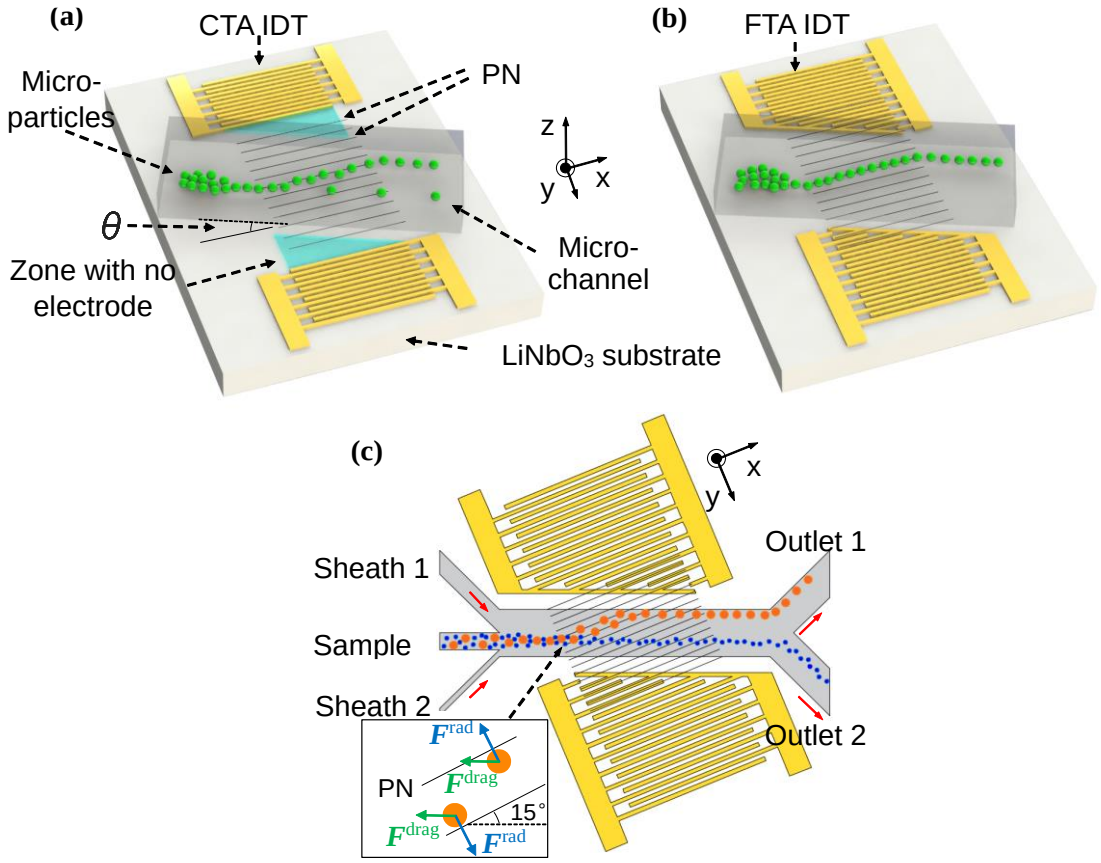

Fig. 3.3 The models of (a) the conventional tilted-angle (CTA) device and (b) the filled tilted-angle (FTA) device. The interdigital transducer (IDT) on the FTA device has additional electrodes to fill the blue triangle zones of the CTA. (c) The schematic illustration of the FTA separation.

Table. 3.1 Design parameters of CTA and FTA

SSAW device	Number of pairs of fingers	Tilted-angle θ	Distance between the IDT pair	Width of finger electrodes	Length of finger electrodes	Working area A_w
CTA	40	15°	7 mm	50	10 mm	70 mm^2
FTA	52	15°	4 mm	50	10 mm	40 mm^2

3.2 Device fabrication

The IDTs and microfluidic channels are the most important components in the acoustofluidic manipulation system, and they require high-precision fabrication by CR facilities. In the following sections, the fabrication process of IDTs and microfluidic channels are introduced.

3.2.1 Photolithography

Photolithography creates thin-layer patterns made of photoresists, which are organic compositions, and their solubility is sensitive to Ultraviolet (UV) radiation. The patterns are transferred from photomasks to wafers via a mask aligner instrument that emits UV with controllable radiation intensity(Berkowski et al., 2005, 2007), also called mask alignment. Photolithography also consists of pre- and post- procedures for IDT and microfluidic channel fabrication, including wafer preparation, spin coating, development, wet etching. Metal deposition and channel moulding are the extra processes for IDTs and microchannel fabrication, respectively.

The wafer preparation is cleaning for the following strong and uniform photoresist adhesion on the wafer. It needs to be performed under a fume cupboard due to the harmful solvent used. Then the spin coating is a typical process to evenly deposit photoresist with the desired thickness on a wafer. The typical spin coating process is described in Fig. 3.4. A sufficient amount of photoresist is first injected on the wafer placed on a rotator and fixed by the vacuum. A spinning is followed, and the faster spinning speed leads to a thicker layer established. However, the final thickness of the deposited layer also relates to the viscosity of the photoresist, rotational acceleration, the order of muti-spinning with different speeds and the environment,

such as temperature and humidity. The environment needs to be strictly monitored and controlled. Soft or hard baking on a hotplate is followed to solidify the spined photoresist or strengthen the resist structure, respectively. Multi-layer structures can be built by repeating the procedure with soft baking in between.

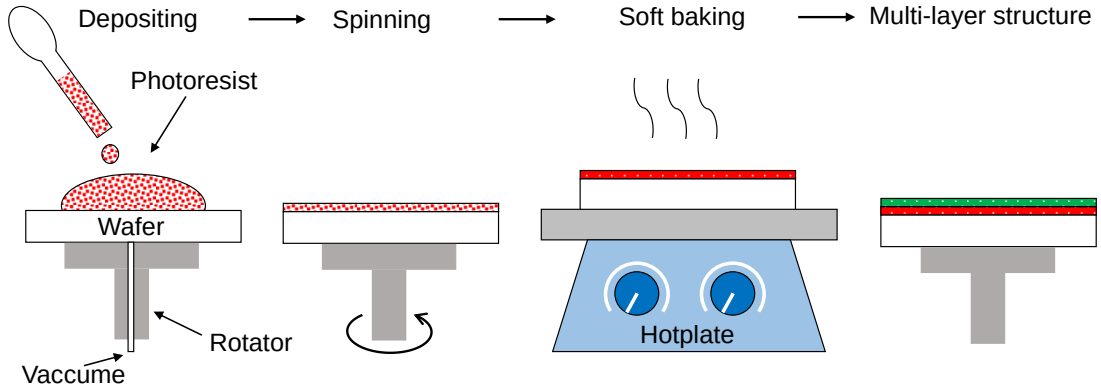

Fig. 3.4 The process of spin coating. The photoresist is deposited on the wafer and followed by a spinning. A soft baking is required for multi-layer structures.

The essential step of photolithography, mask alignment, is proceeded after the spin coating. As shown in Fig. 3.5, the wafer with a thin photoresist layer is placed on a mask aligner that emits UV radiation to the photoresist through a photomask. The photomask contains the desired pattern to be transferred onto the photoresist. A precise pattern can be created by controlling the UV intensity and exposure time, depending on the photoresist properties and the manufacturing environment. Under the UV exposure, the positive photoresist becomes soluble when it is rinsed in the photoresist developer that is the solvent to remove the undesired part of the resist.

On the contrary, the negative resist becomes insoluble to the developer when exposed to UV. After developer rinsing, the insoluble structures of the thin resist layer are left on the wafer, and create the pattern. Therefore, positive and negative resist react separately to UV exposure and form opposite patterns using the same

photomask. The IDTs are fabricated by depositing metal on the pattern followed by wet etching, which removes material from the wafer by liquid chemicals.

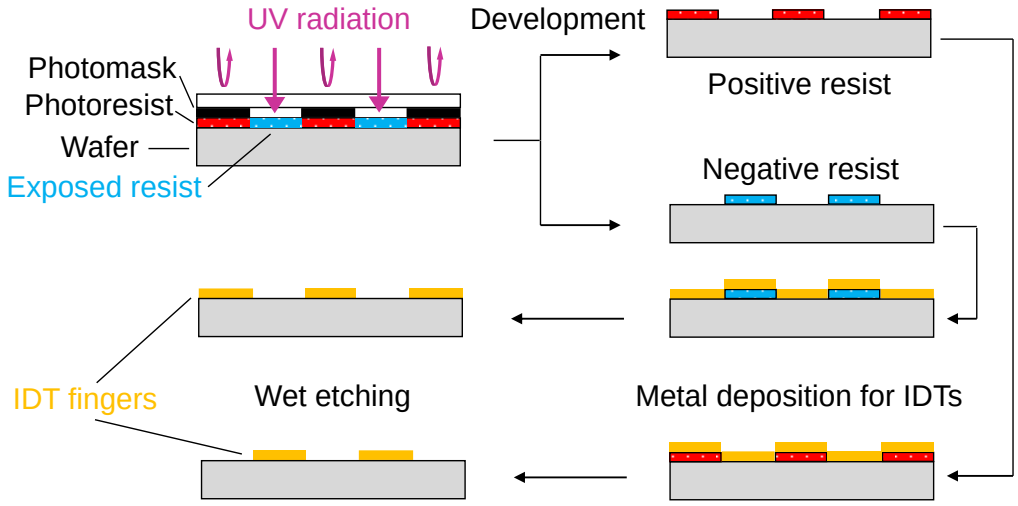

Fig. 3.5 The process of mask alignment, development and wet etching for IDT fabrication. Positive and negative resist separately react to UV exposure and form opposite patterns using the same photomask. Metal is deposited on the wafer with resist patterns after development, and then the IDT fingers are fabricated by the wet etching.

3.2.1 Fabrication of interdigital transducers (IDTs)

During the soft lithography, dust can result in defects in the productions. All the procedures were carried out in the CR to avoid the undesired dust, and the manufacturing procedure was based on recent studies(Shi et al., 2009, Travagliati et al., 2013). The fabrication procedure was a standard lift-off photolithographic process with gold on $LiNbO_3$. The detailed steps for the CR fabrication are presented as follows.

The IDT can be fabricated by either positive or negative photoresists using different

methods. For positive resist manufacturing, a double layer resists structure needs to be applied. In contrast, the negative resist method only needs a single layer deposition because of the UV radiation and photoresist properties. As shown in Fig. 3.6, by using the positive resist method, the wall of the resist structure after patterning and development was inclined that led to the connection of the deposited metal; thus, the IDT electrodes could not be fabricated after the wet etching. By implementing the double-layer method, this problem was avoided. As to the negative resist method, the inclined resist wall was in the opposite direction so that the metal was deposited separately in each groove to form the finger electrodes.

In summary, the inclined wall was caused by the UV intensity decreasing with UV penetrating the resist, so the positive resist diluted more. At the same time, the negative photoresist's solidification became less during the exposure. Due to the above mechanism, the single-layer negative resist method was selected for the rest of the manufacturing work because of its less complexity.

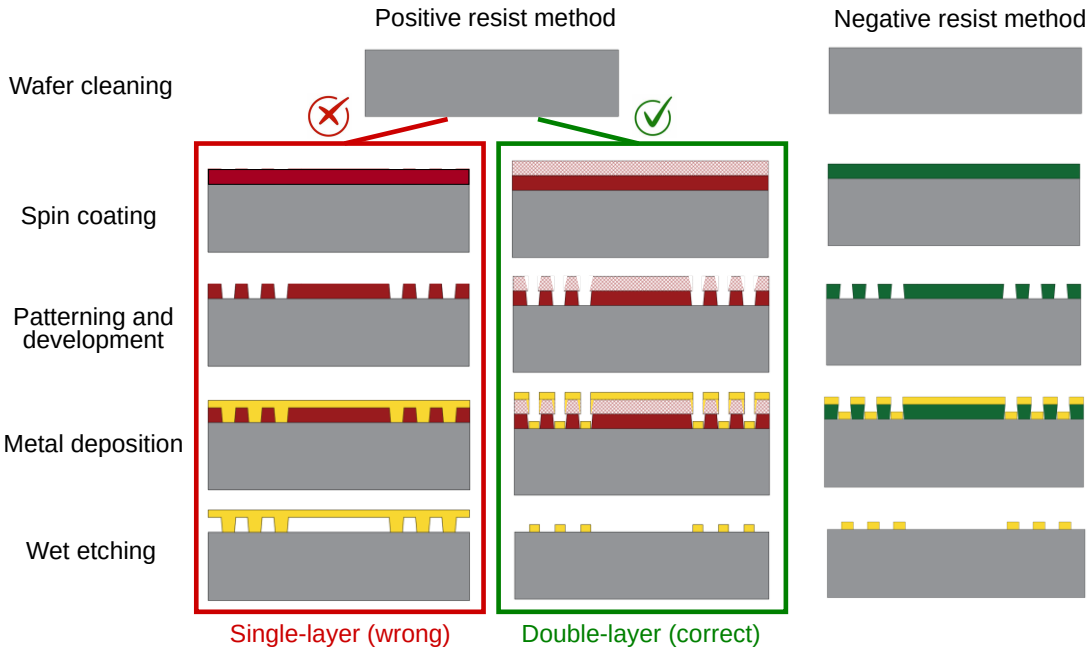

Fig. 3.6 The schematic of IDT fabrication by photolithography. The double-layer positive resist and single-layer negative resist methods are suitable for the IDT

fabrication due to the resists reaction to UV exposure. The negative resist method is less complex, so that selected for the IDT fabrication.

When choosing the material for patterning finger electrodes onto the piezoelectric substrate to develop IDTs, several features, including substrate adherence, electrical resistivity and boiling point need to be considered. Table. 3.2 shows common IDTs finger's material properties. Adherence property is essential for the bonding between the interdigital electrodes and piezoelectric substrates. High adherence allows long-term usage of IDTs by reducing wear or even fingers fall-off from the substrate during the assembling and transporting of the device. The lower electrical resistivity allows for low joule heat produced and better energy conversion. The boiling point determines the possible fabrication methods for depositing the layer of electrodes onto the substrate. The thermal evaporation method can be used with a lower boiling point, which is cheaper, simpler, and faster(Kirschner, 2010). Based on those parameters, the most attractive material would appear to be copper, but it tends to diffuse into the substrates(Hashimoto, 2000). Although gold has poor substrate adherence, it has lower resistivity, providing higher efficiency for the device. Additionally, it has the appropriate boiling point, thus allowing the thermal evaporation methods to be used. Therefore, gold was selected as the material for patterning electrodes with chromium (Cr) as a thin adheresion layer.

Table. 3.2 Properties of piezoelectric materials for SAW generation(Kirschner, 2010)

Metal	Substrate adherence	Electrical resistivity (μΩ·cm)	Boiling Point (K)
Copper	Good	1.7	3200
Aluminium	Good	2.65	2792
Gold	Poor	2.2	3129
Tungsten	Average	5.0	5828
Titanium	Good	50	3560

The $LiNbO_3$ wafer was rinsed with acetone, methanol and isopropanol (IPA), respectively, by leaving the wafer in each solvent on a hotplate at 85°C for 5 mins. A nitrogen gun blowing then dried the wafer. The AZnLoF 2070 negative resist was deposited on the $LiNbO_3$ wafer for the spin coating (4000 rpm, 60 secs, for 5.5 μm layer) followed by a soft bake (110 °C, 90 secs). The wafer covered by resist was then aligned with a photomask and exposed under the UV radiation (83 mW/cm^2) for 40 secs. The UV dose was the key parameter as a guide for adjusting mask alignment and can be denoted as,

$$Intensity\ (\mathrm{mW/cm^2}) \cdot exposuretime\ (\mathrm{s}) = dose(\mathrm{mJ/cm^2}).$$

Another soft bake was undertaken to strengthen the adhesion between the aligned resist and the wafer (110 °C, 90 secs). The sample was rinsed in the MF 319 developer and deionized water for 1 min to remove the unwanted photoresist. Long developing can lead the whole pattern structure to fall off from the wafer. The nitrogen gun blowing finally dried the wafer.

Edwards 306A Thermal Evaporator was used to deposit metal for electrodes patterning. As shown in Fig. 3.7, the evaporator consists of a single removable glass

bell jar chamber pumped by a turbopump and backed by a rotary pump. The rotary pump is also to roughly pump the chamber from atmospheric pressure. The improved pumping performance can be achieved by cooling a liquid nitrogen trap positioned on the diffusion pump. The chamber is always thoroughly cleaned and left at the pressure of $5*10^{-2}$ mbar after each usage. The thermal deposition process started from releasing the chamber to air pressure and placing the wafer with resist patterns facing down on the substrate holder inside the chamber. Cr and gold were positioned in the separate crucibles, and the vacuum chamber was sealed. Cooling water was introduced to the system, and the rotary pump was open till the pressure inside the chamber reached $5*10^{-2}$ mbar. The system was switched to the turbopump to work for 30 mins, and the diffusion pump was then filled with liquid nitrogen till the chamber pressure decreased below $4*10^{-6}$ mbar (30 mins). After the turbopump was closed, the evaporated material was heated up by generally increasing the system's voltage to 70 volts. The mass of the deposited material was measured in real-time by the system and converted to thickness. After firstly depositing a 20 nm layer of Cr as the adhesion layer, the crucible was switched to the one containing gold. The evaporation process was repeated until a layer of 100 nm gold deposition was achieved. The whole system was closed and left for 1 hour to cool down. Then the wafer was taken out, and the chamber was fully cleaned and left at the pressure of $5*10^{-2}$ mbar. The final wet etching process removed the rest of the resist and left the finger electrodes on the wafer. The wafer can either be left in the acetone overnight or put in the ultrasonic bath with acetone for fast removal.

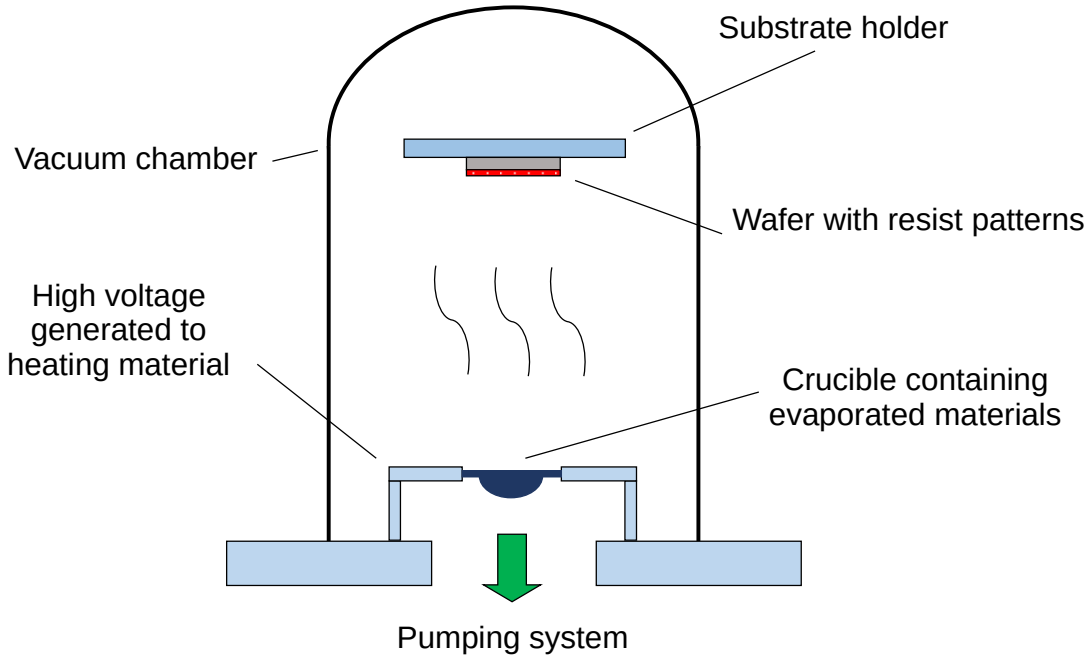

Fig. 3.7 The schematic of the thermal evaporation system for depositing IDT electrodes. The targeting material is evaporated in the vacuum chamber from the electricity heated crucible towards the substrate fixed on the substrate holder.

3.2.2 Fabrication of microfluidic channel

There are many methods for fabricating a microfluidic channel, while lithography on a solid material is conventional to fabricate microfluidic channels. Micro-milling by a high precision numerical control system provides fast manufacturing of hard materials, but the shape of the spindle limits the resolution of the microfluidic channels. Direct laser etching to create microchannels is rapid but it requires specific thermal degradation effect materials and critical parameters control(Wang et al., 2012). CR based photolithography provides higher precision but with a complex procedure and high cost.

The materials for the microfluidic channel can be separated into hard and soft materials. Hard materials, such as poly (methylmethacrylate) (PMMA) and polycarbonate (PC), are normally used in BAW devices that its low attenuation and high acoustic reflection properties benefit the single transducer devices depending on the reflection to generate the standing wave inside the microchannel. However, the high SAW reflection rate of hard materials can prevent SAW from interacting with samples. Moreover, the SAW devices create standing waves by using two opposing transducers without limiting the reflection properties of the channel mateirals(Lenshof et al., 2012a). The most popular soft material for making microfluidic channels is PDMS(Ren et al., 2013), which has the advantages of ease and low cost in microfabrication(McDonald et al., 2000). Its transparency allows the real-time observation during SAW manipulation, and its acoustic impedance is close to the water, which avoids the chaotic reflection in the flow(Lenshof et al., 2012a). Photolithography is commonly used to fabricate the moulding for PDMS microchannel using SU-8 negative photoreisist(Faustino et al., 2016). Therefore, the PDMS was selected as the microchannel materials and photolithography was used as its moulding fabrication method.

The SU-8 2050 negative photoresist was used to fabricate the channel moulding on a 3 inches single side polished silicon wafer with CR facilities. The SU-8 was left steady in a bottle overnight before being used to remove any air bubbles that potentially affected the mask alignment quality. The wafer was firstly cleaned with acetone, methanol and IPA bath for 5 mins, respectively, followed by the nitrogen gun blowing. Before photoresist deposition, the wafer was placed on a hot plate (180°C, 5 mins) to acquire a fully dry surface for a strong resist adhesion. After photoresist injection, the spin coating of the wafer was separated into two stages (500 rpm for 15 secs and 2500 rpm for 45 secs) with an acceleration of 200 rad/s^2 for an evenly 60 μm height layer distributed. The UV exposure (83 mW/cm^2 for 10 secs) was between

a pre-baking and post-baking which were 65°C for 3 mins followed by 95°C for 9 mins and 65°C for 2 mins followed by 95°C for 9 mins, respectively. If there are air bubbles generated during the baking, it needs to be stopped till the bubbles break and are re-baked. The ethylene carbonate solvent was used to develop the wafer for 2.5 mins. Finally, the mould was hard baked at 180°C for 20 mins and generally cooled down on a hotplate to fix the resist structure on the wafer that sustains in several times of PDMS channel moulding.

The PDMS microfluidic channel fabrication is described in Fig. 3.8. The silicon elastomer (DOWSIL, SYLGARD 184) and curing agent (DOWSIL, RT Cure) was mixed at a ratio of 10:1, and the mixture was then poured in a container with the channel mould positioned at the bottom. A vacuum treatment was necessary to remove the air bubbles. The PDMS can naturally cure at room temperature over 48 hours with a precise dimension and fine channel surface. It can also cure on a hotplate at 65 °C for 2 hours for fast moulding. After curing, the PDMS was peeled off from the channel mould and followed by punching holes in them for future tubing connection. The hole punching method is shown in Fig. 3.9 a. In short, at the inlet area, a blind hole was created with a diameter of 1.25 mm on the channel side, creating a tank-like space to prevent leakage. A 0.5 mm through-hole for fitting the tubing metal connectors was then created, concentric with the blind whole. At the outlet area, the blind hole was similarly created while the 0.5 mm through-hole was slightly tilted punched from the side, which can decrease the pressure rather than comparing with the structure of vertical punched. Fig. 3.9 b shows the photo of a PDMS microchannel.

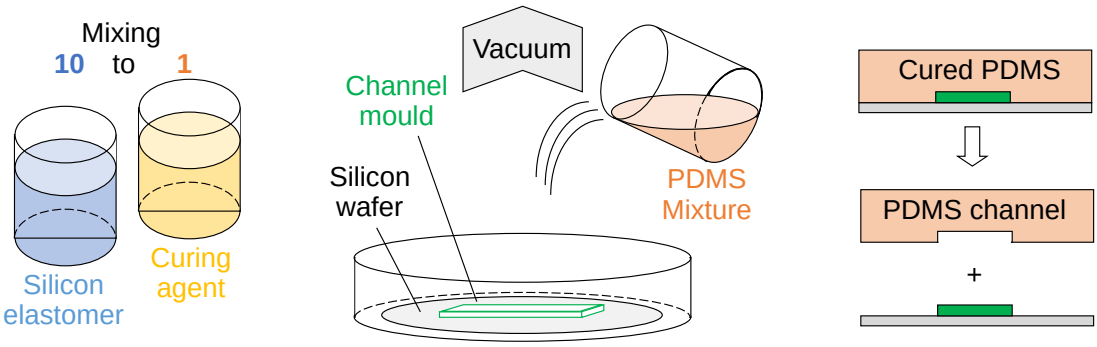

Fig. 3.8 The moulding process of PDMS microfluidic channel fabrication. The silicone elastomer and curing agent were firstly mixed with a ratio of 10 to 1. The mixture was poured into a container with the channel mould followed by vacuum treatment. The cured PDMS channel was peeled off from the mould.

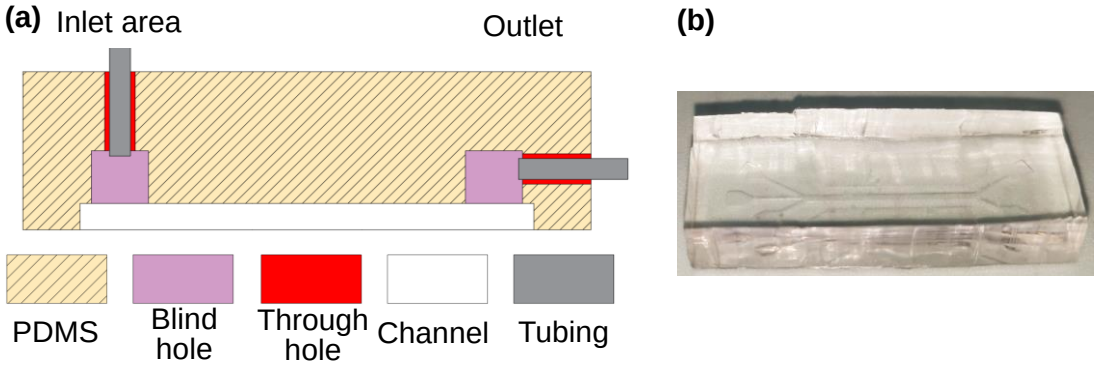

Fig. 3.9 (a) The schematic of hole punching for tubing connection on a PDMS microfluidic channel. (b) the photo of a PDMS microfluidic channel.

3.2.3 Bonding microfluidic channel on IDTs

The bonding of microfluidic channels is essential since any leakage can cause a short circuit of IDTs, permanently damaging the interdigital electrodes and breaking the IDTs substrates. The most commonly used bonding technique is plasma treatment of both microfluidic channels and IDT wafers. This method requires not only a costly

plasma treatment device but also a long and multi-step procedure. If there is leakage during the experiment, the bonding needs to be repeated. A mechanical bonding method was developed that was easy to install and fast to recover from leakage conditions. The structure is demonstrated in Fig. 3.10. The mechanical force was applied by screws, connected with the holder, and compressing a 3D-printed pressor. A transparent acrylic plate was placed between the pressor and the PDMS channel to resist deformation and evenly distribute the pressure along the PDMS channel on the IDT wafer. This technique is easy and fast to assemble and disassemble; thus, the bonding can be quickly recovered once leakage happens by only properly cleaning both the PDMS channel and IDTs substrate.

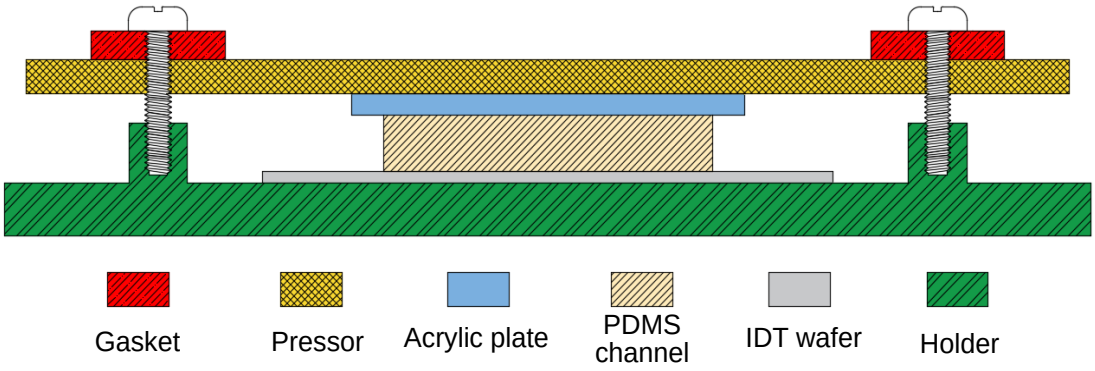

Fig. 3.10 The schematic of the mechanical bonding method for PDMS channel and IDT wafer. A pressor, acrylic plate, channel and IDT are placed on a holder, and fixed by screws and gaskets.

3.3 Experimental setup

The Acoustofluidic CTC separation system set-up diagram is shown in Fig. 3.11. The overall system can be mainly divided into two parts, the acoustofluidic platform and the system controls. The SSAW generation, the sample separation and the collection

process all happen on the acoustofluidic platform. The system controls include the RF signal input for the IDTs, microfluidics control of sample input and cooling control for the cooling of the IDTs.

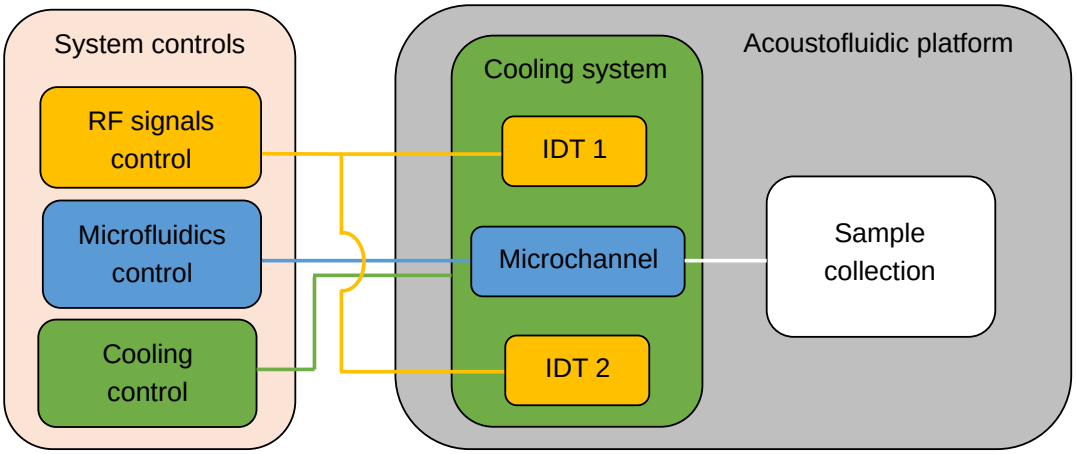

Fig. 3.11 Overall acoustofluidic CTCs separation system setup diagram

3.3.1 RF signal generation and power monitoring

The RF signal is generated and amplified for driving the IDTs. A signal control system for the SAW device was developed to generate and monitor the input signals to the IDTs. The signal monitoring components can help to calculate the real-time efficiency of the electrical input power of the IDT. An abnormal efficiency indicates that a systematical check needs to be implemented before the further operation not to damage the system.

The block diagram of the signal control set-up is shown in Fig. 3.12. 19.6 MHz RF signal was generated from the signal generator, which then was amplified by a power amplifier (Mini-circuit, ZHL-100W-GAN+). Since the resistance of the IDTs was far

from 50 Ω (i.e., standard optimal resistance), it resulted in signal reflection from the IDTs. L-type impedance matching networks were implemented between each side of IDT and the coupler to improve the electrical power efficiently transferred to the IDTs with less signal reflection. The L-type matching network used the most simple capacitor-inductor components connection compared with others. The electrical impedance of the IDT was identified by a vector network analyser (VNA, E5061B ENA, Keysight Technologies, U.K.). The selection of capacitors and inductors for matching networks depended on the IDT's impedance on the Smith Chart.Thus the power meters were applied to monitor the forward (incident) and reverse (reflected) powers. The difference between the forward and reverse power was calculated to determine the input power P_{in}, in Eq. 2.22. The forward power and reverse power was shown by the two power meters (Keysight 8990B) connected to a coupler (Mini-circuit, ZFBDC20-62HP-S+).

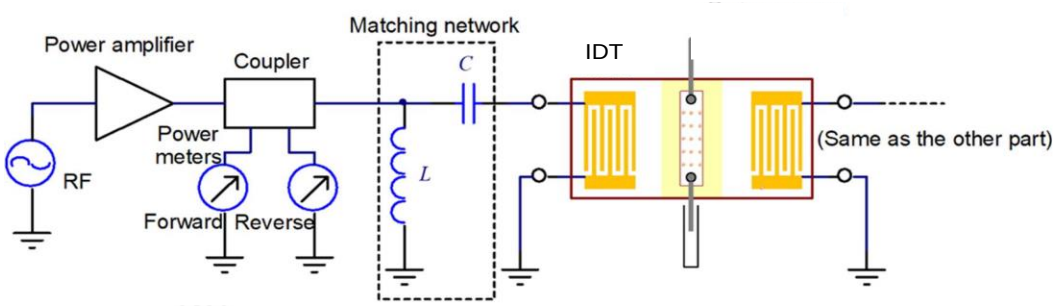

Fig. 3.12 The setup of the RF signal generation and power monitoring. The RF signal was generated and amplified by the signal generator and power amplifier, respectively. It was monitored by the coupler and power meters, and was transported to the IDTs through an L-type matching network.

3.3.2 Microfluidic control

For the sample input of the SAW system, either a pressure pump (EverFlow, MK3+) or two syringe pumps (Masterflex) can be used to introduce the sample and sheath flow [22% glycerol with 78% phosphate buffer saline (PBS) (vol/vol)]to the microfluidic channel. Before each experiment, IPA (Sigma-Aldrich, 2-Propanol solution), 0.1% bovine serum albumin (Sigma-Aldrich, Albumin bovine serum) and PBS are used for flushing the microchannel for approximately 30 min to clean and coat the microchannel, which prevents the microparticles from adhering to the channel. In the three inlets microchannel, given the fixed width of the microchannel and a flow rate, the width of the samples is controlled by the flow rate of the two side inlets. A 3D-printed part is developed to balance the pressure at the output since the minor difference in the height of the outlet tubing tips can significantly change the flow rate of one of the outlets. Fig. 3.13 shows the 3D-printed pressure balancer with a vertical, horizontal and angle adjustment, as well as an angle fixing, to position the collector mounted on the holder. By adjusting each of them at specific positions, the pressure of each outlets tubing will be balanced and fixed. In the experimental work in chapters 4,5,6 and 7, the pressure balancer was applied and provided an easy and stable outlet flow control.

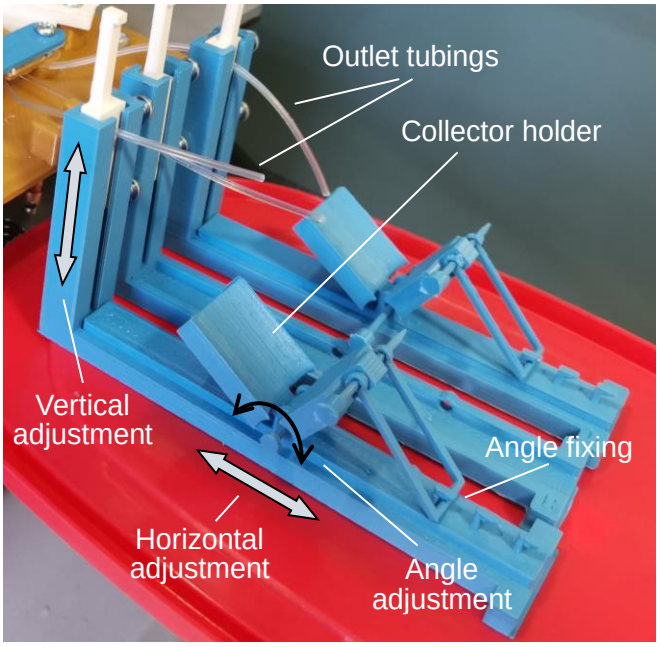

Fig. 3.13 The 3D-printed outlet pressure balancer consists of a vertical, horizontal, angle adjustment and angle fixer to precisely position the collector mounted on the holder, thus achieving a pressure control.

3.3.3 Cooling control

The long working period and high electrical power input can create joule heat on the IDT wafer. The thermal conductivity of lithium niobite is low. Thus, the heat generated is not able to quickly dissipate at room temperature. The overheated device can impact cell viability, acoustic field distribution and even damage the IDTs. Therefore, active cooling needs to be integrated into the system. Fig. 3.14 shows the schematic diagram of the developed active cooling system. With thermal grease, the IDTs substrate bonded with a microchannel is mounted on an aluminium plate. An electric thermal sensor is attached to the plate near the IDTs wafer to give a temperature

reading and feedback to a control board. Once the temperature exceeds a pre-set threshold, the peltier, which generates cooling on the top side and the heat on the other side, is triggered until the desired temperature is reached. There is a cooling fan with a copper structure to dissipate the heat from the bottom side of the peltier. The colling system was successfully built and provided a more stable working environment for the following experiments described in chapters 4,5 and 6. There was no IDT breakage after applying this cooling system. However, the temperature readings always slightly fluctuate around the setting value, which could be improved by using a more advanced control unit in the future.

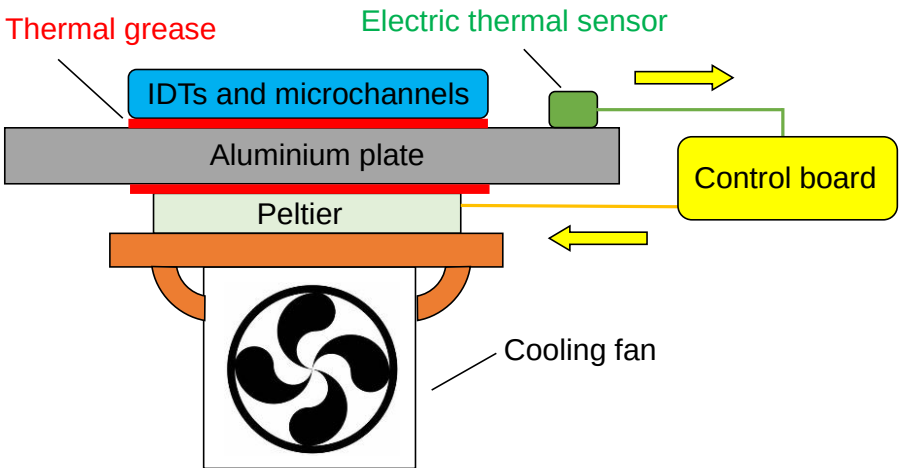

Fig. 3.14 The schematic of the system cooling control. The IDTs bonded with microchannels are mounted on an aluminium plate that connects a thermal sensor for sensing and a Peltier for cooling. The signal from the sensor is transferred to a control board to control the trigger of the peltier. The bottom cooling fan helps the heat to dissipate from the system.

3.4 Conclusion

For the design of IDT, the parallel design can provide large acoustic pressure by its small working area, while the wavelength limits its microchannel's width. This limitation can lead to frequent blockage of the microchannel during the experiment. However, the parallel design is the basic IDT design suitable for fundamental research of SSAW-based manipulation. Thus it was applied and demonstrated in chapter 4. The CTA design avoids the limitation of microchannels' width by sacrificing the acoustic pressure while handling samples with a large concentration of particles. It was applied in the cell washing project described in chapter 5.

In comparison to parallel and CTA design, the FTA design not only avoids the channel width limitation but also saves the acoustic pressure sacrificed by the CTA design. It can also provide a more evenly distributed acoustic field than CTA does. The FTA design requires only a minor modification to the CTA design, i.e., adding 24 more finger electrodes to reduce the working area without extra fabrication and cost. With such advantages, the FTA design was used to investigate the cancer cell separation in chapter 6.

As to the device fabrication, lithium niobate substrate with chrome and gold electrodes patterns was selected as the suitable materials, while the PDMS was chosen for the materials of microfluidic channels. The detailed CR fabrication method by soft lithography and evaporation in CR was established, and effective responses to the changes in the fabrication environment were developed. Furthermore, the experimental setup established a stable and controllable working environment that is essential for the following acoustofluidic manipulation work.

Chapter 4 Acoustofluidic manipulation using parallel IDTs

This chapter investigates the relationship between electrical input power and cell-mimic microparticles behaviours in the acoustofluidic field, such as particle deflection and separation. Acoustic-based particle separation has great potential in biomedical and chemical applications. Its potential in manipulating microparticles of various sizes is yet to be fully explored. The fundamental IDT structure (parallel design) was used to avoid interference from unnecessary features. This work with cell-mimic microparticles can become a guidance for the following bio-sample manipulation projects in this thesis. In this work, the numerical study and experimental data for four polystyrene particle sizes, 5 μm, 10 μm, 15 μm and 20 μm were studied and compared. By using the numerical methods, the relationship between the microspheres final position and the input power of the IDT, the acoustic radiation force distribution along the y-direction in the microchannel, the distribution of microspheres at the inlet and outlet, and the relationship between the separation efficiency and the input power were analysed. The theoretical part of this chapter was investigated together with Hanlin Wang. This chapter more focuses on the experimental work and the comparison between the theoretical model and practical data. More details related to the simulation are presented in the appendices.

4.1 Numerical simulation of acoustofluidic separation

The schematic of the parallel IDTs devices for particles separation is described in Fig. 3.1 in chapter 3. Particles dominated by acoustic radiation force can be deflected from the middle of the channel towards the PN on each side and collected by the side

collection. In contrast, the other particles are collected at the centre waste outlet.

4.1.1 Equations for particle trajectories and separation efficiency

The theoretical part was investigated together with the help of Hanlin Wang. For convenience, the essential parameters used in the simulation are listed in Table. 4.1.

Table. 4.1 Parameters used in the simulation of parallel IDT structure.

	Description	Value
μ	Viscosity of the fluid	1.64 mPa s
β_f	Media compressibility	3.48 x 10-10 Pa-1
ϕ	Acoustic contrast factor	0.5685
d	Polystyrene microsphere diameter	
P	Electrical input power	
w	Sample channel width	120 μm
T	Polystyrene microsphere travelling time	
λ	Wavelength	200 μm
A	Acoustic working area	0.3 mm^2
Z	Acoustic impedance	17437.5 x 10^3 Ohm

According to Eq. 2.19, the final position on the y-axis (y_f) of microparticles after the acoustic separation is then given by

$$y_f = \frac{\lambda}{2\pi} tan^{-1}\left(tan\left(\frac{2\pi}{\lambda} y_0\right) \cdot e^{k \cdot T}\right) \tag{4.1}$$

$$k = \frac{\pi^2}{9} \cdot \frac{d^2}{\lambda^2} \cdot \frac{P \cdot Z}{A} \cdot \frac{\beta_f \phi}{\mu} \tag{4.2}$$

The particles final position represents whether they are separated or not after acousto-deflection. To numerically study the particles separation rate related to the

IDTs electrical input power, the probability density function of polystyrene microspheres in the initial sample fluid can be expressed as a parabolic function:

$$f(y_0) = \frac{6}{w^3} \cdot \left(\frac{w}{2} - y_0\right)\left(\frac{w}{2} + y_0\right) \tag{4.3}$$

where y_0 is the initial lateral position of polystyrene microspheres. After the acoustic deflection, the final polystyrene microspheres position is given by Eq. 4.1. The initial distribution (Eq. 4.3) then can be transformed into a new probability density $g(y_\mathrm{f})$ at the exit of the acoustic region, using the following relation,

$$f(y_0)dx_0 = g(y_\mathrm{f})dy_\mathrm{f} \tag{4.4}$$

which leads to

$$g(y_\mathrm{f}) = f(y_0) \cdot \left(\frac{dy_\mathrm{f}}{dy_0}\right)^{-1}$$

$$= f(y_0) \cdot \left\{e^{-k \cdot T} + e^{-k \cdot T}\, tan^2\left(\frac{2\pi}{\lambda} y_0\right)\right\} \cdot sec^{-2}\left(\frac{2\pi}{\lambda} y_0\right) \tag{4.5}$$

For a given polystyrene microsphere diameter d, the separation efficiency (ξ) is then defined as the fraction of microparticles collected as the centre outlet

$$\xi(d) = \int_{-w/2}^{w/2} g(y_\mathrm{f})\, dy_\mathrm{f} \tag{4.6}$$

4.1.2 Numerical study of acoustofluidic separation

MATLAB was used to build these numerical models for further investigation, and the results were compared with the practical experiments. The general parameters settings in MATLAB codes are presented in Appendix 1. Fig. 4.1 (a) shows the

schematic of the model, in which a sheath to sample flow rate ratio of 3:1 was set to focus the sample width to be 17 μm (yellow area), or ±8.5 μm off the AN. The two PNs located at the position ±50 μm off the ANs. In the acoustic field, microspheres were driven by the acoustic force towards the PNs in the sheath, where they were 'trapped' and flushed by the sheath flow to be collected at the sheath outlets. When the microsphere entered the acoustic field, its initial y position, y_0 , could be anywhere within the sample width, which determined its acoustic radiation force (Eq. 2.20) and, in turn, the acceleration of its translation to the PN. Its final position, y_f, was the distance from the AN to the microsphere position when it was leaving the acoustic field.

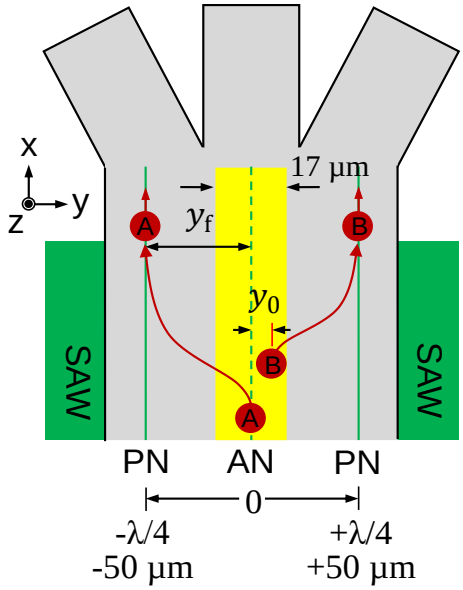

Fig. 4.1 The schematic of the model used in the numerical analysis, two PNs are positioned near the wall of the microfluidic channel, which drives microspheres to translate to the sheath. PN – solid green lines), AN – green dash line. The yellow area is the sample width of 17 μm.

Fig. 4.2 shows the translation of the four sizes of microspheres on the y-direction under different input powers. The vertical axis is the final position y_f of the

microspheres inside the microchannel calculated by Eq. 4.1. Solid lines show the final position of the microspheres, which initiated from the boundary of the sample flow (e.g. microsphere B in Fig. 4.1). In contrast, dash lines show the microspheres' final position of which initial position was 1 nm off the ANs (e.g. microsphere A in Fig. 4.1). Thus, an upper power P_{H} and a lower power P_{L} are identified, which can successfully translate microspheres initially located across a different lateral position in the sample width. Operating at the lower power P_{L} is about to translate any microspheres to the sheath outlet while operating at the upper power P_{H} allows all microsphere to migrate to the sheath outlet.

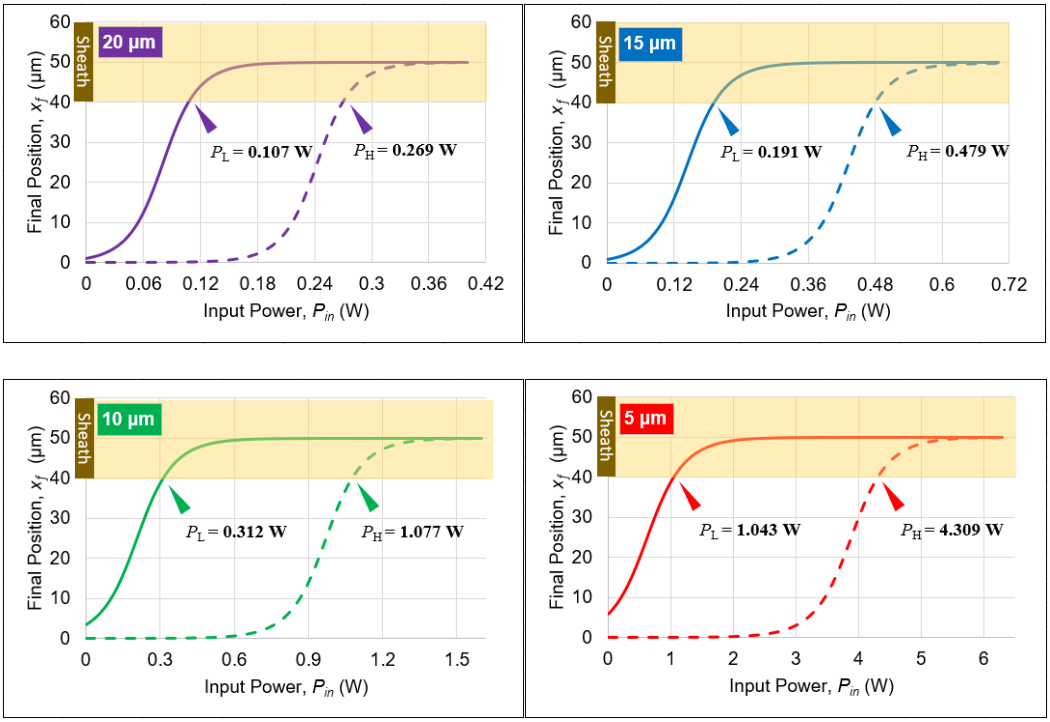

Fig. 4.2 Numerical analysis: the final position for the four sizes of microspheres in the acoustofluidic device under different input powers. The upper power P_{H} is for translating microspheres close to the centre, the lower power P_{L} is for translating microspheres at the boundary of the sample width. The MATLAB coeds are shown in Appendix 2.

The operation input powers ranged between P_H and P_L are shown in Fig. 4.3 for the four sizes of microspheres. Smaller microspheres require higher operation input power to be translated to the sheath. It can be predicted that if the operation input power of one microsphere is distinct from that of another microsphere, in their mixture, by operating the input power of the larger microspheres, the larger microspheres can be separated to the sheath outlet. In comparison, the smaller microspheres remain at the centre outlet. For example, when operating the input power between 0.107 W and 0.269 W (the upper and lower power shown in Fig. 4.2), 20 μm microspheres can be separated from the 10 μm ones. If the operation input power of two sizes overlapped, e.g. 20 μm and 15 μm, 15 μm and 10 μm, 10 μm and 5 μm, they are not possible to be separated from each other using the current settings. One can alter the parameters such as the sample width, flow rate, and sheath to sample flow rate ratio to change the separation resolution.

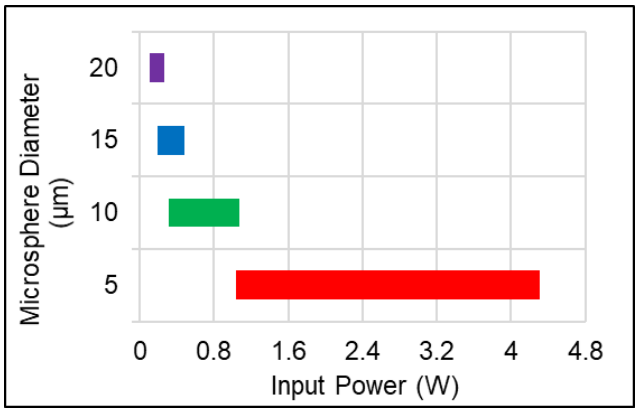

Fig. 4.3 Numerical analysis: the operation power range for translating the four sizes of microspheres from the sample to the sheath.

Fig. 4.4 shows the magnitude of the acoustic radiation force is proportional to the volume of the microsphere, the input power, and associated with the microsphere position on the y-direction. The maximum input power (solid line) and minimum input power (dash line) used in the experiment were applied to plot the force versus lateral

position.

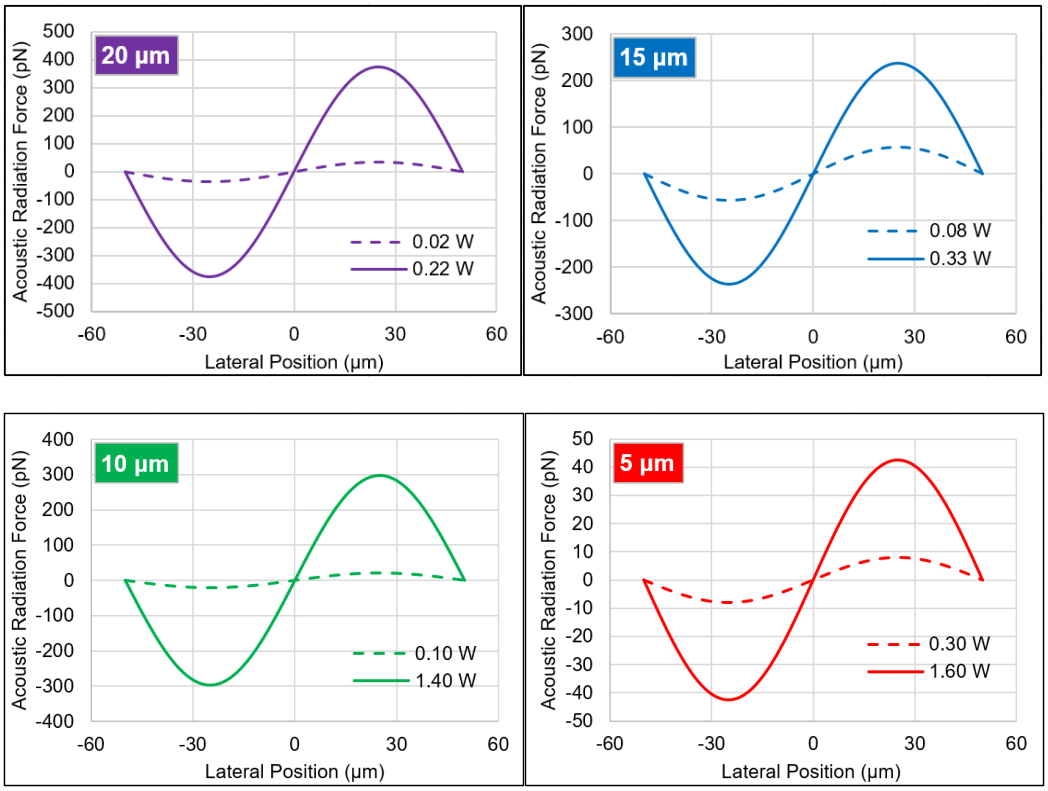

Fig. 4.4 Numerical analysis: the acoustic radiation force on four sizes of microspheres in the acoustofluidic device under different input powers. The MATLAB codes are shown in Appendix 3.

A 90% separation efficiency, i.e., the number of microspheres collected from both sheath outlets accounts for 90% of the total collected from both the sheath and centre outlets, is considered a good separation rate. To predict the separation efficiency, probability densities of microspheres at the inlet and outlet were analysed using the model given in the SI. At the inlet, all the microspheres were concentrated between ±8.5 μm off the microchannel centre due to the focusing effect produced by the two sheath flows (dotted line in Fig. 4.5a). The acoustic field deflected the microspheres, resulting in an increasing microsphere density at the sheath regions (solid line in Fig.

4.5a). When the input power is set to 0.564 W, 90% of the 10 μm microspheres are migrated to the sheath. The input power was altered in the model to investigate the power for separating microspheres with different sizes. Fig. 4.5b shows a critical input power of 0.107 W, at which all the microspheres still stay in the centre without being translated to sheath for collection, and the sample width of the 20 μm microspheres increase from 20 μm to 80 μm. Increasing the input power can further decrease the centre density and increase the sheath density. An example of the input power of 0.25 W is given in Fig. 4.5c. Neither 5 μm and 10 μm microspheres receive sufficient acoustic force to migrate to the sheath for the given separation length (1 cm, the same as the length of the IDT), while almost all the 20 μm microspheres translated to the sheath and 64.8% of the 15 μm microspheres also collected at the sheath outlet.

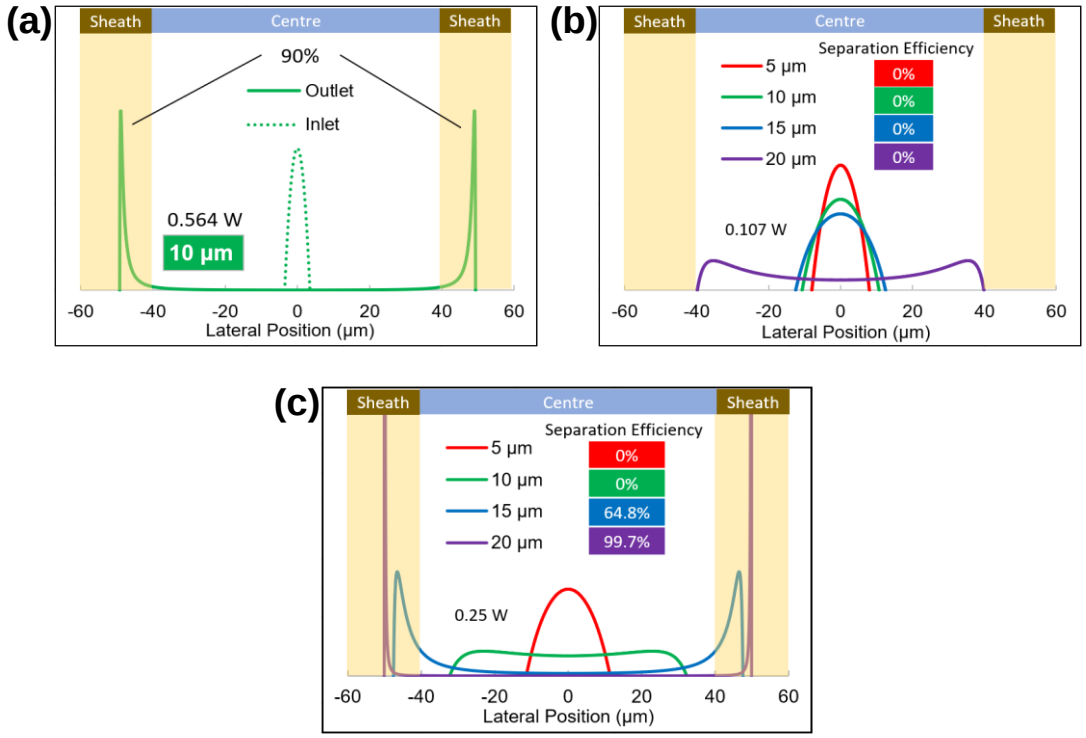

Fig. 4.5 Numerical analysis: (a) the probability density of the microsphere sized 10 μm at the inlet and outlet when the input power was 0.564 W. (b) The critical input power (0.107 W) to keep all microspheres remained at the centre. (c) When the input power is 0.25 W, nearly all the 20 μm microspheres were translated to the sheath, while the 64.8% 15 μm microsphere migrated to the sheath and all the 5 and 10 μm microspheres stayed at the centre. The MATLAB codes are shown in Appendix 4.

The above simulation results indicate a clear relationship between the input power and the separation efficiency of different sizes of microspheres. Fig. 4.3 informs the possibility of the separation between 20 μm and 10 μm, 15 μm and 5 μm, which leads to Fig. 4.6 showing the theoretical input power to separate these two combinations and guiding the following experiments to achieve efficient separation.

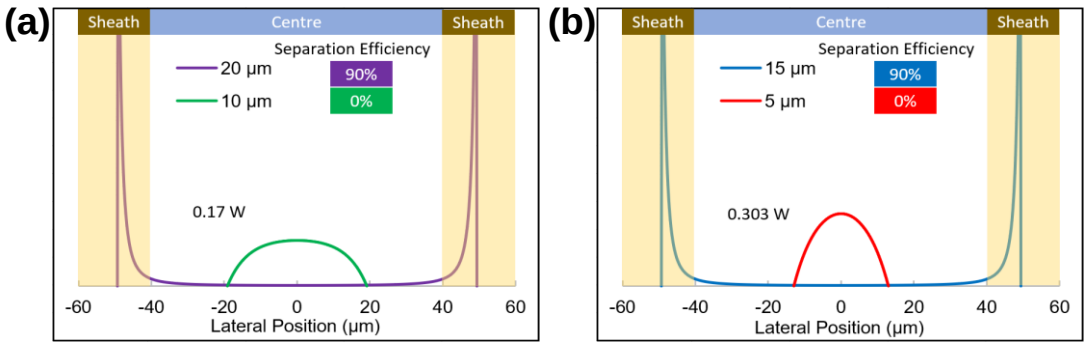

Fig. 4.6 Numerical analysis: (a) the distribution of 20 μm and 10 μm microspheres after separation at the input power of 0.17 W. (b) The distribution of 15 μm and 5 μm microspheres after separation at the input power of 0.303 W.

4.2 Experimental data and discussion

To investigate the true input power of the IDTs, the incident power and the reflected power were monitored using power meters. The output power of the signal generator was adjusted to produce an output power between 0.3 W to 1.6 W, as shown in Fig. 4.7. The input power is well correlated to the incident power. The power reflections from the IDTs are approximately 6% and 4%, respectively, which indicate a high power conversion on both IDTs.

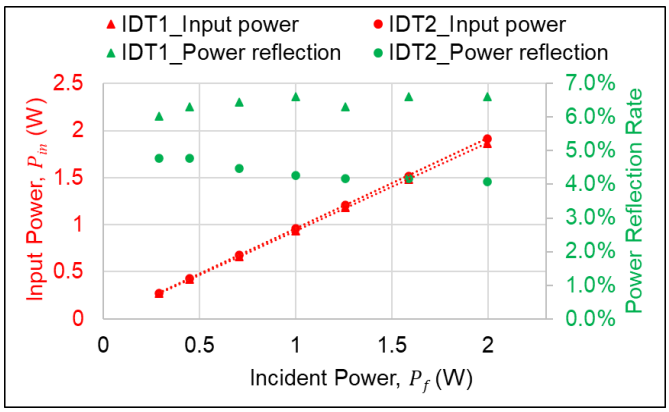

Fig. 4.7 The input power measured by subtracting the incident power by the reflected power. IDT1_P/IDT2_P are the input powers of the two IDTs, IDT1_R/IDT2_R are the reflection power percentages

Four sizes of polystyrene microsphere 5 μm, 10 μm, 15 μm and 20 μm were prepared in a mixture of 78% (vol/vol) phosphate-buffered saline (PBS) (Sigma-Aldrich) and 22% glycerol (Sigma-Aldrich). This ratio was used to mimic the density of human whole blood. The glycerol could also prevent microspheres sedimentation. The concentration of the five microsphere sizes was 2×10^7, 1×10^7, 5×10^6, and 5×10^6 per mL, respectively. Smaller sizes were prepared at higher concentrations to show a clear trajectory during the acoustic manipulation under the microscope. For the experiment separating one size from another, the smaller microsphere was diluted to approximately 1.5×10^6 per mL. The bigger ones were diluted to approximately 7×10^5 per mL in each test group. Hemocytometers undertook all the microparticles counting works under the microscope

The numerical study has provided indications of the operation input power to actuate microspheres and projected the theoretical input power to separate one microsphere from another. To validate the simulation result, the below experiment actuating microspheres with different powers was conducted. In each experiment, single particle size was used to investigate the input power for microsphere translation.

The microsphere sample was introduced to the acoustofluidic device by the pressure pump at a flow rate of 5 μL/min. The input power was increased from zero until almost full translation was achieved. The two sheath flows at 15 μL/ min was applied to create the sample width of 20 μm, or between +10 μm and -10 μm about the ANs. The experimental and simulation results for the four sizes are demonstrated in Fig. 4.8. In general, the experimental data was in quantitative agreement with the simulation trend. The power to achieve 90% microsphere translation is generally larger than the theoretical simulation. It could be caused by the uneven distribution of particles at the initial position or the diffusion of microspheres due to fluid before they flowed into the SSAW field.

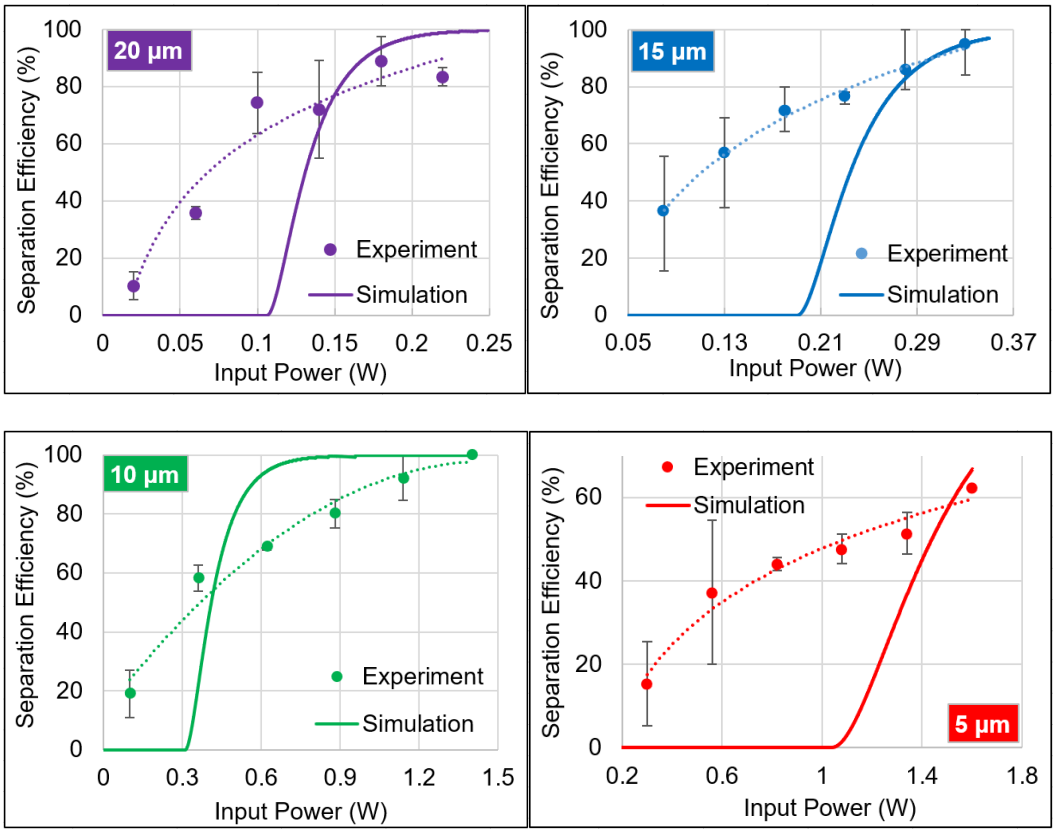

Fig. 4.8 The separation efficiency for the four sizes of microspheres in the acoustofluidic device under different input powers. The error bars represent the range of data collected in the same group

According to the input powers in the experimental data corresponding to the separation efficiency of 90%, the predictions of the input powers for separation the mixture of 20 μm and 10 μm, 15 μm and 5 μm are given in Table. 4.2, with the comparison to the theoretical values and the input powers for separation experiments in the following section.

Table. 4.2 The theoretical, experimentally predicted and practical input powers to separate polystyrene microsphere mixture of 20 μm and 10 μm, 15 μm and 5 μm

Separation input power	20 μm and 10 μm mixture	15 μm and 5 μm mixture
Theoretically predicted	0.170 W	0.303 W
Experimentally predicted	0.221 W	0.302 W
Practical	0.252 W	0.301 W

Microsphere mixtures were introduced to the microchannel using the same sample flow and sheath flow rates as the above experiment. Fig. 4.9 shows the separation efficiency of the two sizes of microspheres. As shown in Fig. 4.9a, by adjusting the input power, 86% of 20 μm microspheres were separated at the input power of 0.22 W, while 74% of 10 μm remained in the centre outlet. Fig. 4.9b shows that 98% of 15 μm microspheres were separated from 5 μm at the input power of 0.4 W, while 89% of 5 μm microspheres remained in the centre outlet. Large error bars presented on the 20 μm microspheres could be caused by the collision of microspheres during the separation process, which changed the particles' trajectory. For example, when the 20 μm microspheres were actuated, 10 μm microspheres either remained or moved at a much slower velocity towards the PNs. The collision would not only slow down 20 μm microspheres but also, in opposite, bring 10 μm closer to the PNs. As the volume ratio of 5 μm to 15 μm microspheres is smaller than the ratio of 10 μm to 20 μm microspheres, the separation efficiencies of 5 μm and 15 μm were similar to the

results of single microsphere translation experiments.

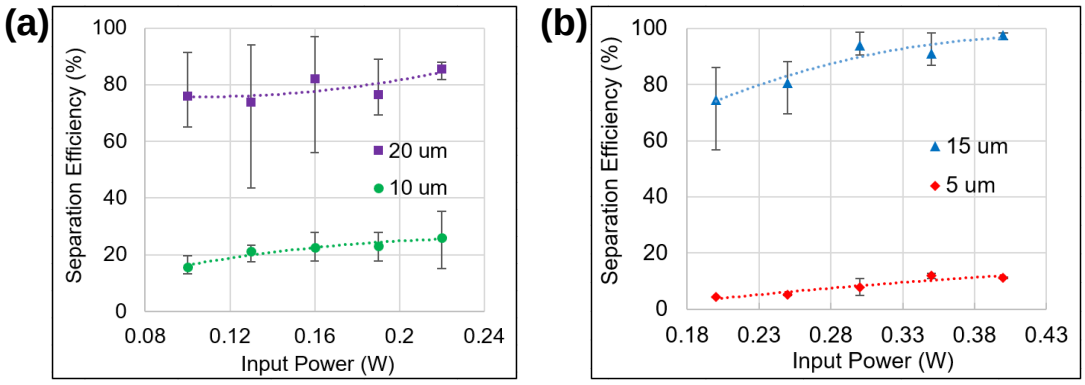

Fig. 4.9 Separation efficiencies of two groups of polystyrene microspheres mixture. a) 20 μm and 10 μm; b) 15 μm and 5 μm.

4.3 Conclusion

Polystyrene microspheres separation of 20 μm out of 10 μm and 15 μm out of 5 μm were achieved with a separation efficiency of around 90%. The experimental results of singe size particles actuation can approximately match the indication from the numerical study for particles separation related to the IDT input power. In the mixed particles separation experiment, separating 15 μm from 5 μm is more promising than 20 μm from 10 μm, because the volume ratio between 15 μm and 5μm particles is larger. Although the acoustofluidic separating microspheres on the parallel IDT is achieved, the narrow microchannel width can result in channel block by accumulated bio-samples which is stickier than the artificial microspheres. This project guided the following acoustofluidics manipulation work in chapters 5 and 6.

Chapter 5 Washing Electroporated Cells Using SSAW

This chapter aims to develop an SSAW-based cell washing device that can deflect from the original medium and collect cells into a new medium (separating cells from the medium). Compared with separation between different types of cells with different physical properties, the deflection of a single type of cells needs less precise input power control, according to the experiment demonstrated in chapter 4. As a novel cell manipulation application, this study presents acoustofluidic devices to effectively wash cells after electroporation to enhance transfection efficiency and cell viability. Considering the potential microchannel block problem by accumulated cells, an SSAW device with the CTA design is applied in this study.

5.1 Introduction of electroporation

Electroporation is applying pulsed electric fields to cells to attract the molecules of interest around the cells215 and allow for intracellular transport of materials(Gehl, 2003). Normally, cells and mediums containing materials that need to be transferred into the cells are firstly filled into a container with two opposite electrodes. Then the mixture is applied with high-amplitude (hundreds to thousands of volts) and pulsed (nanoseconds to microseconds) electric fields. Electroporation is commonly used for DNA, RNA and proteins delievery(Cox et al., 2015, Thakore et al., 2015, Balboa et al., 2015, Latella et al., 2016, Maggio and Goncalves, 2015, Qin et al., 2015, Schumann et al., 2015), and cancer gene therapy(Okita et al., 2011, Heller and Heller, 2015). Electroporation is a relatively simple gene delivery method only using target plasmid DNA (pDNA, a small circular piece of DNA that can replicate independently) solution for transfection without other chemicals(Cervia and Yuan, 2018). However, it is noted

that electroporation has low transfection efficiency(Pakhomov et al., 2010) and cell viability (Henshaw and Yuan, 2008)due to the unprotected pDNA degraded by nucleases(Lechardeur et al., 1999, Crook et al., 1996, Cifani et al., 2015, Bureau et al., 2004, Rattan et al., 2014) and the metal ions generated from the metal electrodes. These ions will cause many biological macromolecules to precipitate from the solution so that the available amount of pDNA will be reduced for cell transfection(Kooijmans et al., 2013, Stapulionis, 1999). To overcome the current problem of low efficiency after electroporation, centrifugation has been used to wash cells to remove the harmful ions from the metal electrodes. Still, the high gravitational force produced during centrifugation can alter the cell structure(Costa and de Morais, 2014) and even cause cell damage(Upadhyay et al., 2019). Moreover, a few kinds of specialized electroporation medium(Hsi et al., 2019) have been developed to avoid the harmful effect, while elongated staying of cells in the medium can still reduce the electroporation efficiency and cells viability(Rashid and Coombs, 2019). All the above methods involve intensive labour and are not well-controlled due to manual manipulation. It is desired to have an automated and efficient medium switching system to condition the medium of the samples after electroporation.

5.2 Mechanism of SSAW-based switching cell medium

As a competitive method, the acoustic-based microfluidic technique is an emerging technique to manipulate biological cells with the advantage of preserving original cellular structure and states(Wu et al., 2018d, Augustsson et al., 2016). As a novel application, the electroporated cells were first applied in the acoustofluidic device for cell washing which can be automatically achieved without serious cells damage or cells distortion compared to conventional centrifugation.

A CTA device(Ding et al., 2014) was employed to switch cell medium as the schematic shown in Fig. 5.1. A pair of interdigital transducers (IDTs) produced SSAW forming a series of pressure nodes (PNs) along with the propagation. A PDMS-made microchannel with three inlets and two outlets was placed between the IDTs with an angle of 15 degrees. The microchannel width was four times the SSAW wavelength, which allowed eight PNs to form inside the microchannel. A sample of microparticles in Medium 1 was introduced to the middle inlet. Two sheath flows containing Medium 2 were introduced to the side inlets to control the position and width of the sample inside the microchannel. The microparticles were attracted by acoustic radiation force produced by SSAW and trapped along the PNs after entering the acoustic field. At the same time, Medium 1 remained its dynamic flow pattern due to the two sheath flows. By optimising the outlets, microparticles trapped on the PNs were migrated to Outlet 1, entering Medium 2, while Medium 1 flowed on its original course and entered Outlet 2. The microparticles were removed from the old medium and joined the new medium after the SSAW actuation. The device was made by photolithography patterning with metal electrodes on a $LiNbO_3$ piezoelectric substrate.

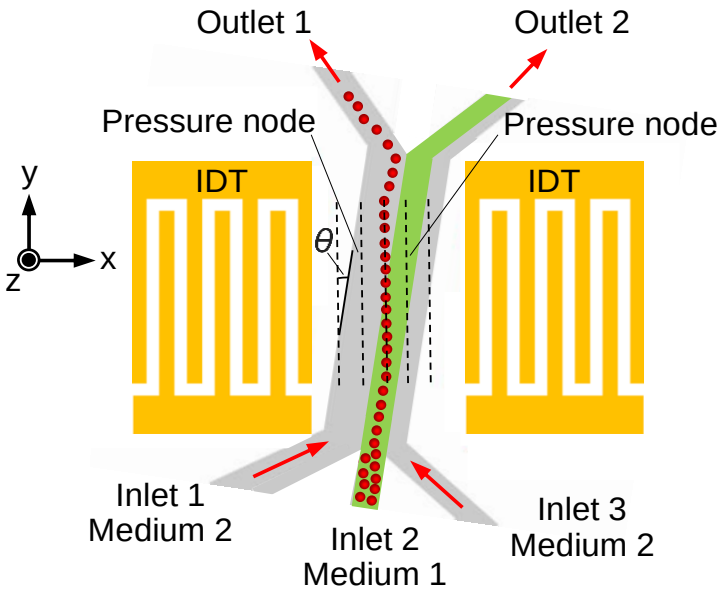

Fig. 5.1 Schematic of the tilted-angle SSAW device cell washing device. Electroporated cells with the original medium were introduced and focused from the middle inlet. Due to the acoustic radiation force, the cells were deflected to Outlet 1 while the original medium remained in the flow and was collected by outlet 2.

5.3 Sample preparation for the SSAW washing device

5.3.1 Preparation of polystyrene microspheres

To characterise the recovery rate and switching medium efficiency, polystyrene microspheres with a diameter of 15 μm were diluted in distilled water with blue pigment at a concentration of 5×10^6 per mL to mimic cell sample, which was injected into the middle inlet. The concentration was measured by a cell counter (Countess II FL Automated Cell Counter). Distilled water was also used as the two sheath flows introduced to the two side inlets.

The flow rate of the three inlets was investigated to ensure all the microspheres within the blue pigment could flow into Outlet 2 before applying SAW. In contrast, most of the microspheres could migrate to Outlet 1 after applying SAW. A trial of flow rate was performed before the following experiment to optimise the flow rate. It was noted that the flow rate of Inlet 1, 2 and 3 was 12 µl/min, 3 µl/min and 6 µl/min, respectively, and the microspheres with the blue pigment flew into Outlet 2. The selection of the three flow rates also allowed 100 % microspheres to flow into Outlet 1 while the blue pigment stayed in Outlet 2 when SAW was applied.

5.3.2 Preparation of cell culture and electroporation

Mouse embryonic fibroblast (MEF) cells were used in this experiment. The cells were detached by Trypsin-EDTA and centrifuged at 1900 rpm for 5min. 10^6 MEF cells were resuspended for each electroporation in 100µl Opti-MEM buffer (Sigma-Aldrich) with 1 µg EGFP-N1 pDNA (Clontech, Palo Alto, CA, USA) on ice(Cervia et al., 2018). For electroporation, the samples were filled into 4-mm gap aluminium cuvettes (Bio-Rad). Electroporation was applied once on the samples using BTX ECM 830 Square Wave Electroporation System (Harvard Apparatus, Holliston, MA, USA) at 500V, 500 µs duration and 1Hz frequency. After electroporation, the cuvettes were kept at room temperature for 10 mins for cells recovering, and 300 µl Dulbecco's Modified Eagle Medium (DMEM) (Gibco, Thermo Fisher, U.K.) was added into the sample for further SAW washing. Propidium iodide (PI) was added to the samples before the flow cytometry test for cell viability.

5.3.3 Preparation of cell washing

The MEF cells in 100 µl of the original medium after electroporation was diluted with 300 µl of DMEM to provide enough sample volume for the device because there was sample loss due to the tubing volume in the SSAW device. 100 µl of the diluted sample was taken and evenly separated into two parts as pre- and post-control, respectively. The pre-control was immediately put back to an incubator, while the post control remained the same condition and time with the other 300 µl sample which pumped through the SSAW device. The collected sample and post-control were then moved back to the incubator. The two control and sample passing through the SSAW device were cultured for 24 hours before microscopy observation and flow cytometry. The DMEM was used as the two sheath flow which cells were switched into.

The Gene expression and viability of cells measurement was taken by a flow cytometry system (BD FACS Canto II). The microfluidic part was flushed with 10% bleach, 70% EtOH and PBS before each experiment. To prevent the toxicity of the original medium to cells after electroporation, the viability of cells before and 1-hour after the electroporation (500 V, 500 µs and once) was measured.

5.4 Switching medium of polystyrene microspheres

The polystyrene microspheres were firstly applied to prove the function of the switching medium of the acoustofluidic device. The set flow rates of the three inlets allow the recovery rate of the 15 µm microspheres to achieve 100% when SAW was applied. The recovery rate was defined as the ratio of microparticles pumped through inlet 2 to the number of microparticles collected from outlet 1. Fig. 5.2a & b show the outlet area when SAW is off and on, respectively. It is noted that the blue pigment was

dispended due to the streaming effect produced by SAW. Nearly 100% of 15 um microspheres flowing through the microfluidic channels were driven by the acoustic radiation force and removed from the original sample to Outlet 1.

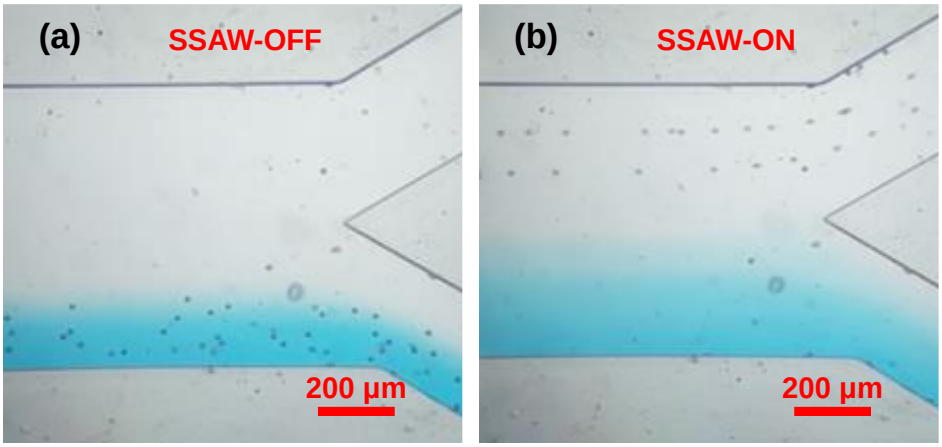

Fig. 5.2 Switching medium for polystyrene microspheres. (a) the 15 µm beads remained with the original blue medium when SSAW was off. B) the 15 µm beads were switched to the new medium when SSAW was on.

The exerted acoustic radiation force was proportional to the input power for producing SAW (Eq. 2.20 to 2.22). A higher input power allowed faster particle migration inside the SAW field, resulting in a higher recovery rate. To investigate the relationship between the recovery rate and the input power using the forementioned flow rates, the input power was increased from 0.5 W to 1.3 W, as shown in Fig. 5.3a, the recovery rate increased from 92.1% to 100%. The following experiment used 1.3 W. Fig. 5.3b indicated the distribution of the sample at the beginning of the acoustic area when SSAW was applied. The microspheres were actuated when entering the SSAW field. It was noted that the input power conversion on both IDTs achieved 97%, which was calculated using the readouts from the power meters. As the device's throughput was also a significant character, the highest flow rate and input power were also tested with the polystyrene microspheres recovery rate of 90%.

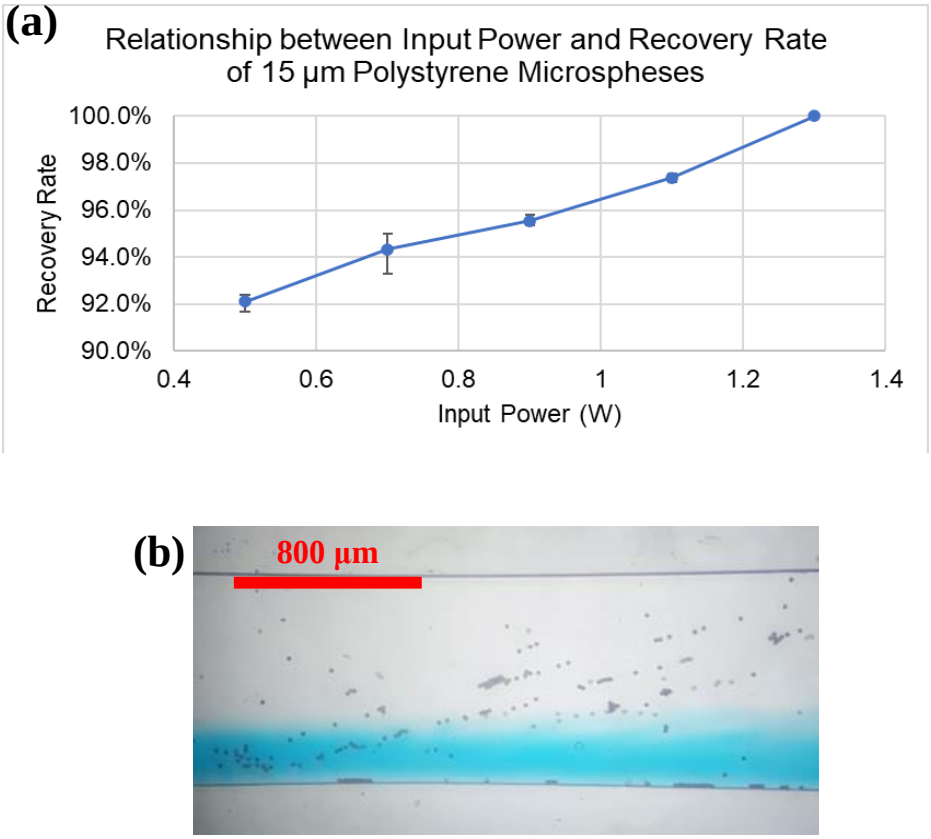

Fig. 5.3 (a) Relationship between Input Power and Recovery Rate of 15 µm Polystyrene Microspheres. The error bars represented the range of data collected in the same group. (b) The distribution of the sample at the beginning of the acoustic area when SSAW was applied.

5.5 Switching medium of cells after electroporation

As shown in Fig.5.4a, the flow cytometry result indicated the proportion of each group of cells with viability and gene electroporation efficiency (eTE) by the EGFP (x-axis) and PI (y-axis) fluorescence intensity of the samples(Cervia et al., 2018). After the cells were electroporated and remained in the medium, their viability dropped from

94.7% to 63.1% in an hour, as shown in Fig.5.4a and b). Therefore, it was essential to combine the medium switching SSAW device with the conventional electroporation process. Then the electroporated cells were pumped through the SAW device. As shown in Fig. 5.5a and b, all the MEF cells kept flowing at the bottom and were collected by the lower outlet when SSAW was off. Conversely, the cells were actuated to leave the original medium and collected by the upper outlet.

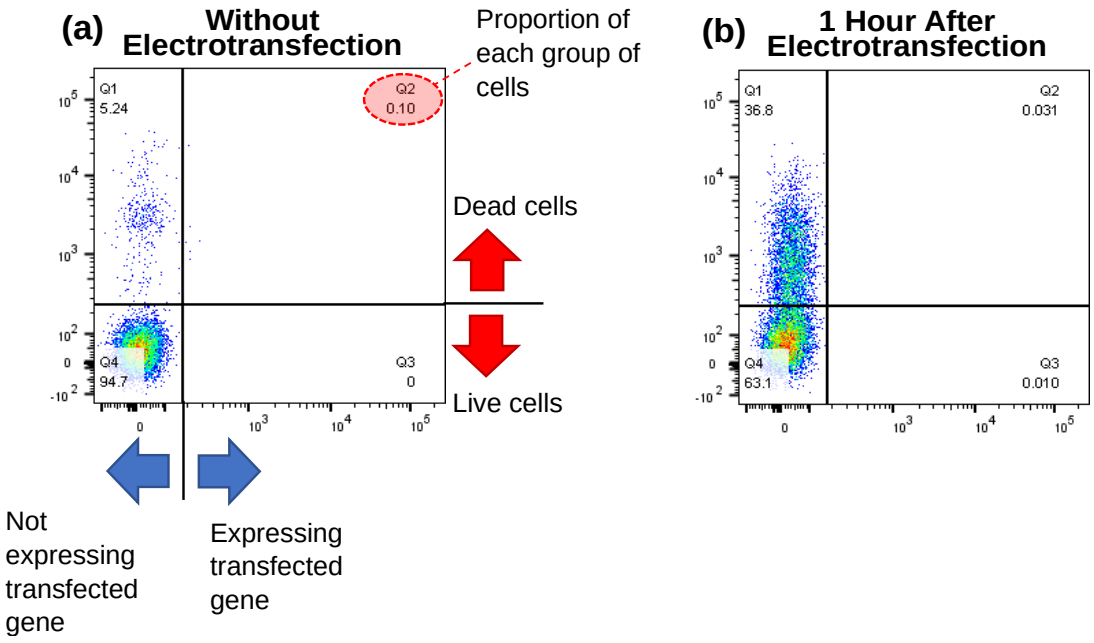

Fig. 5.4 The eTE percentage measurements (a) without electroporation. (b) 1 hour after electroporation.

The eTE percentage in the washed and pre-control groups was 43.8% and 18.4%, respectively, as shown in Fig. 5.5c and d. In addition, the viability of collected cells after switching media (94.5%) was significantly higher than the control group (34.3%).

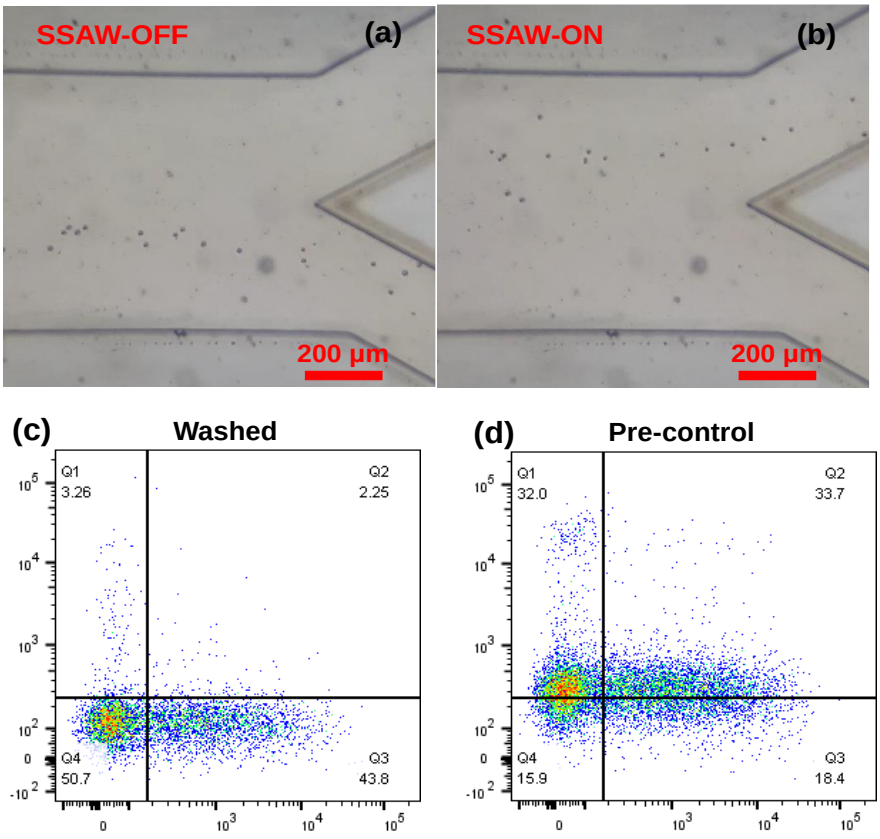

Fig. 5.5 Photos of MEF cells and flow cytometry measurements (a) MEF cells were collected by the lower outlets when SSAW was off. (b) MEF cells were collected by the upper outlets when SSAW was on. (c-d) flowcytometry measurements of washed and pre-control groups.

There were three “external” factors (the shear force by sheath flow, the acoustic pressure by SSAW and the material of microfluidics part of the device) applied to the cells during the whole experiment, which might also have had an impact on the experimental results. Thus, it was important to investigate their effect, and the three groups of measurements were shown in Table. 5.1. Firstly, to investigate the effect of sheath flow, the MEF cells were induced through the SSAW device with SSAW off and the same flow condition. The lower outlet collected all the cells, and the identical pre- and the post-control group were established. The eTE percentage of flowed

sample and two controls were 20.3%, 19.7% and 21.1% after 24 hours incubation, respectively. The results were very close to each other. Therefore there was little impact from shear stress due to the sheath flow. Second, to investigate the effect of SSAW pressure, the MEF cells were pumped through the device without sheath flow with the input power of 4 Watts. To equalise the time when the cells were in the SSAW field with the previous experiment, the sample flow rate was raised to 18 μl/min. A similar measurement of eTE percentage was also found. Finally, the sample was injected through the device without sheath flow or SSAW working to investigate impact from other parts of the device. The sample flowrate remained at 18 μl/min to keep the sample-in-channel time. There were still only minor differences between the results of each group. Thus, the direct effect from sheath flow and SSAW stimulation on eTE was ignored.

Table. 5.1 The eTE percentage of cells in groups of Sheath with electroporation (ET), SSAW with ET, and ET only

	Average eTE %		
	Sheath+ET	SSAW+ET	ET Only
Flowing through device	20.3%	19.2%	20.2%
Pre-control	19.7%	20.6%	19.1%
Post-control	21.1%	19.3%	21.5%

5.6 Conclusions

In this study, cell washing after electroporation via acoustofluidic devices has been applied. To prove the function of the SAW washing device, 15-μm microspheres were first successfully washed out from the distilled water with blue pigment. Then, with a 4W input power, MEF cells were washed from the electroporation medium. Moreover,

the eTE percentage and cells viability were increased after SAW washing. Any alternative factors during the experiment were investigated and shown to have a minimum impact on cell washing. In conclusion, the SAW device was able to wash the cells after electroporation to increase the transfection efficiency and cells viability.

Chapter 6 Investigation of the enhanced FTA SSAW device for cancer cell separation

After exploring cell-mimic microparticles separation and cell washing (single type of cells acoustically defection) in chapters 4 and 5, respectively, this chapter aims to investigate the separation of cancer cells by SSAW device, which is the initial motivation as well as the ultimate goal in this thesis. This work used the novel FTA (Fig. 3.3b) SSAW device to enhance acoustic pressure by patterning additional IDTs to fill the device space adjacent to the microchannel. This FTA design has its unique advantages demonstrated in chapter 3 to achieve better cell manipulation performance. The numerical study and cell deflection efficiency of the FTA device was investigated and compared with the CTA device. The Hela cells and peripheral blood mononuclear cells (PBMCs) were successfully deflected separately at distinct input powers, which showed the possibility of using FTA to separate HeLa cancer cells from PBMCs. The numerical model of this chapter was investigated with the help of Hanlin Wang. This chapter more focuses on the experimental work and the comparison between the theoretical model and practical data. The work in chapter 6 has been published in Ultrasound in Electron Device Letters, 2021.

6.1 Numerical comparison of FTA and CTA devices

COMSOL Multiphysics software was applied to simulate the pressure distribution using the thermoviscous module with the cooperation of Hanlin Wang in the research group. By adding a decay coefficient C_{d}, according to Eq 2.5, 2.6 and 2.11 in chapter 2, the velocity boundary condition (BC) in the frequency domain is denoted as(O'Rorke et al., 2018),

$$BC = \omega A_0 \left[e^{-C_d\left(\frac{W}{2}-y\right)} e^{i\left[-k_s\left(\frac{W}{2}-y\right)+\omega\right]} + e^{-C_d\left(\frac{W}{2}+y\right)} e^{i\left[-k_s\left(\frac{W}{2}-y\right)+\omega\right]} \right] \quad (6.1)$$

where A_0, k_s, w_0 and y is the amplitude of leaky SAW displacement, wave number of leaky SAW, channel width, and location on the y-axis, respectively. The parameters were used only for comparison purposes are demonstrated in the following table. The impedance of the PDMS is set for the boundary condition between the two sides and top of geometry.

Table. 6.1 The parameters (only for comparison purposes) for the numerical study of acoustic pressure comparing FTA with CTA.

Water		
Density	ρ	997 kg/m^3
Speed of sound	c_0	1497 m/s
Shear viscosity	μ	0.890 mPa s
Bulk viscosity	μ_b	2.47 mPa s
Compressibility	κ_0	448 T/Pa
Lithium niobite ($LiNbO_3$)		
Speed of sound	c_{sub}	3994 m/s
Poly-dimethylsiloxane (PDMS,10:1)		
Density	ρ_m	920 kg/m^3
Speed of sound	c_m	1076.5 m/s
Attenuation coeff.		31 dB/cm
Acoustic actuation parameters		
Wavelength	λ	200 μm
Forcing frequency	f	20 MHz
Displacement amplitude	A_0	0.1 nm
Displacement decay coefficient	C_d	116 m^{-1}
Acoustic impedance		
PDSM	Z_{PDMS}	0.98 MPa·s/m

Numerical simulation was first applied to investigate the acoustic pressure on cross-sections inside the microchannel at five positions for the FTA and CTA devices (Fig.

6.1a). The acoustic pressure exhibits a similar symmetric pattern at both devices' mid-point (Position 5) (Figs. 6.1c & 6.1d). The added finger electrodes evenly follow the microchannel in the FTA device and provide equal amplitudes of the counter-propagating SAWs into the microchannel. Thus the acoustic patterns in the FTA device are more uniform along the acoustic field, i.e., Positions 1 to 4 (Fig. 6.1d), while the CTA patterns vary at different positions (Fig. 6.1c). Moreover, the FTA offers a notably larger acoustic pressure at most positions given the same input power (Fig. 6.1b). The CTA's pressure is decreased from Position 1 to 4 and achieves the minimum at the mid-point (Position 5), where both the IDTs apart from the microchannel result in the largest attenuation. While the FTA's acoustic pressure slightly varies along the microchannel, which allows more controllable manipulation of microparticles. At the entry Position 1 (Fig. 6.1c), where the gap between the microchannel and the lateral IDT varies the most, the acoustic pressure in the CTA shows a distorted pattern while the FTA (Fig. 6.1d) shows a periodic pattern, attributed to the added fingers.

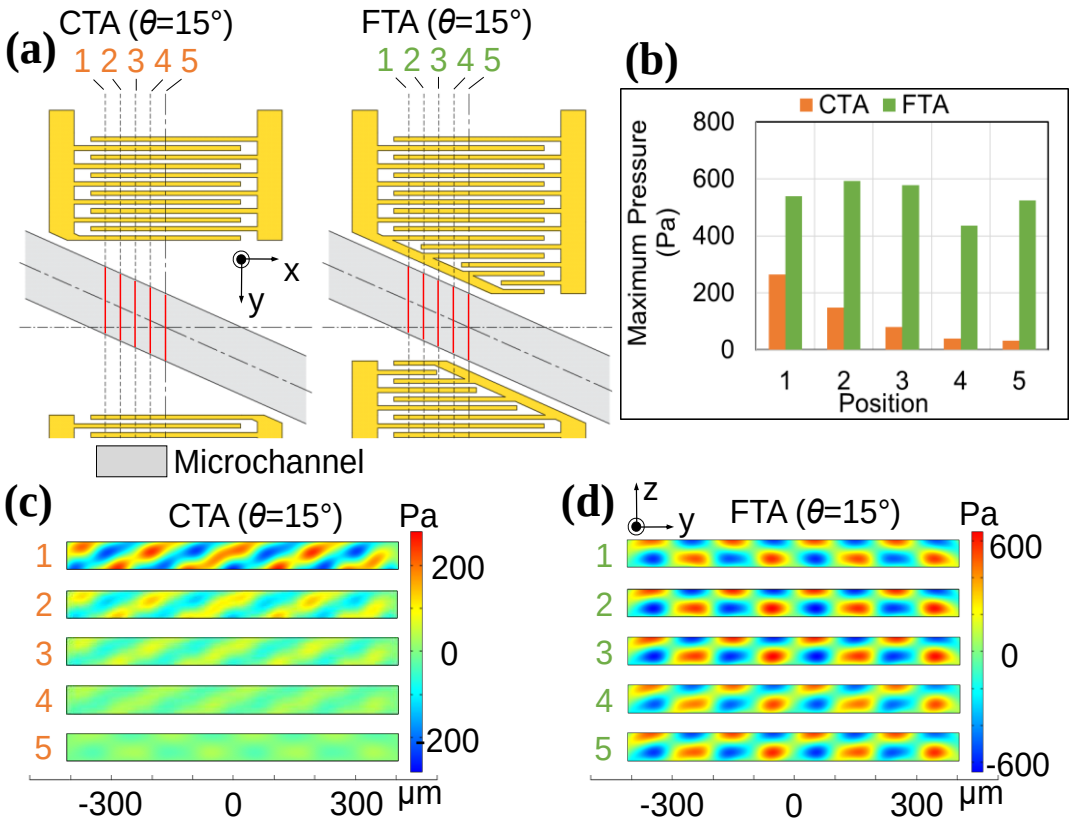

Fig. 6.1 (a) Five positions with the interval of 100 μm are chosen for the numerical study of the acoustic pressure in the CTA and FTA devices. (b) The maximum acoustic pressure of the five positions. (c) and (d) the acoustic pressure distribution of the five positions in the two devices.

6.2 Microsphere deflection comparison of FTA and CTA devices

The working frequencies of the FTA and CTA devices are 19.5 MHz and 19.6 MHz, respectively. A small difference may be caused by the capacitance and inductance introduced by the added electrodes. A suspension with 15-μm polystyrene microspheres was used to evaluate the deflection efficiency, W, of both the devices using $W = (c_2\, V_2)/(c_1\, V_1 + c_2\, V_2)$. Herein, c is the microsphere concentration, and

V is the volume of the collection from outlets. The subscript number indicates the outlet (Fig. 3.3c in chapter 3). The microspheres were suspended in a PBS and glycerol mixture (780:176, w/w) at a concentration of 2×10^6/ml. The flow rates of the three inlets were set to allow all the microspheres to flow into Outlet 2 before applying SAW, which were 10 μl/min, 5 μl/min and 5 μl/min, respectively. The deflection results are shown in Fig. 6.2a. The CTA device achieves 80% and 100% deflections at 0.85 W and 1.05 W, respectively, which agrees with the previous studies using the CTA structure(Ding et al., 2014, Li et al., 2015a). The FTA shows a notably increased deflection efficiency than that of the CTA in the power range. For instance, ~7% deflection efficiency is achieved in the FTA device compared with ~1% in the CTA at the input power of 0.25 W. The FTA achieves ~91% nearly doubling to the CTA device at the same input power of 0.65 W. Fig. 6.2b shows the microscopic images of the CTA and FTA devices under different input powers, where the deflection of the microspheres at the outlets are captured. Altogether, the results show that the FTA device can achieve the same deflection efficiency of 80%, requiring only ~57% of the CTA input power, reducing heat generation in the device and minimizing the safety risk to biological samples and the device itself.

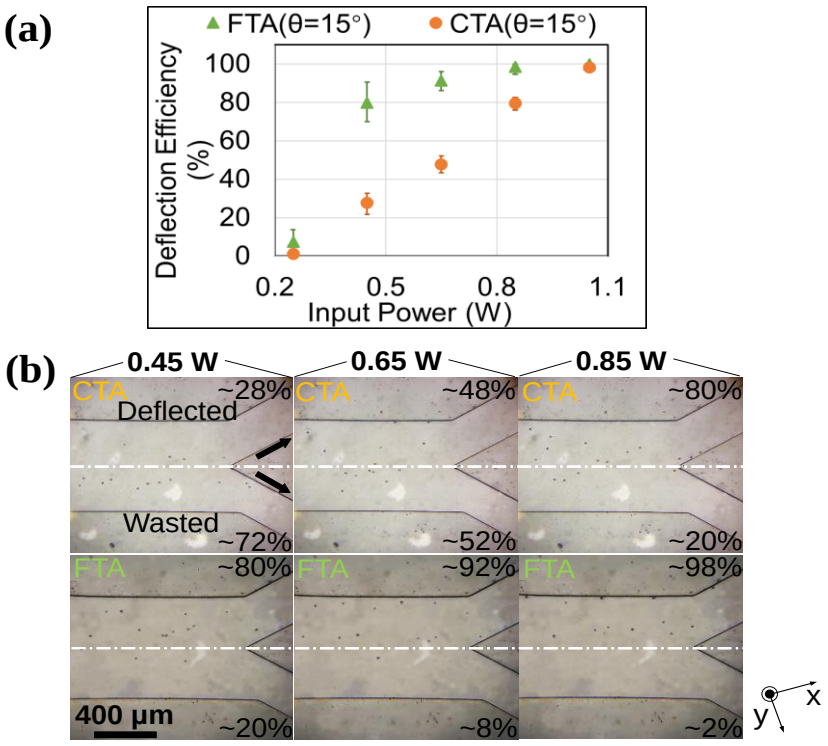

Fig. 6.2 (a) Deflection efficiency against the input power of the two devices. (b) The microscopic image of the FTA deflection at different input powers.

6.3 Applying the FTA Device in Manipulation of Cancer Cells

The FTA device has a great potential to improve the manipulation of cancer cells owing to its larger acoustic pressure created by the novel IDT structure. Commercially-sourced HeLa cells and PBMCs supplied by Cardiff University Biobank were prepared for the deflection test. As the deflection results are shown in Fig. 6.3a, the FTA device generally exhibits a higher deflection efficiency on HeLa cells due to their larger, denser but less compressible properties yielding faster deflection than those of PBMCs(Czerlinski et al., 1987, Guigas et al., 2007, Ding et al., 2014). The deflection efficiencies for the HeLa cells and PBMCs are ~90% and ~25%,

respectively, at the input power of 4.5 W while maintaining a similar cell viability of 90% as the CTA device(Li et al., 2015a). The microscopic image displaying the cell deflection at 4 W is shown in Fig. 6.3b. The HeLa cells are effectively actuated and migrated to Outlet 1, whereas most PBMCs stay in Outlet 2. The effective manipulation of cells with an FTA device shows the feasibility of separating HeLa cells from PBMCs while further testing is needed in the future. It can also be applied to cell washing and patterning, blood component separation, and bacteria manipulation.

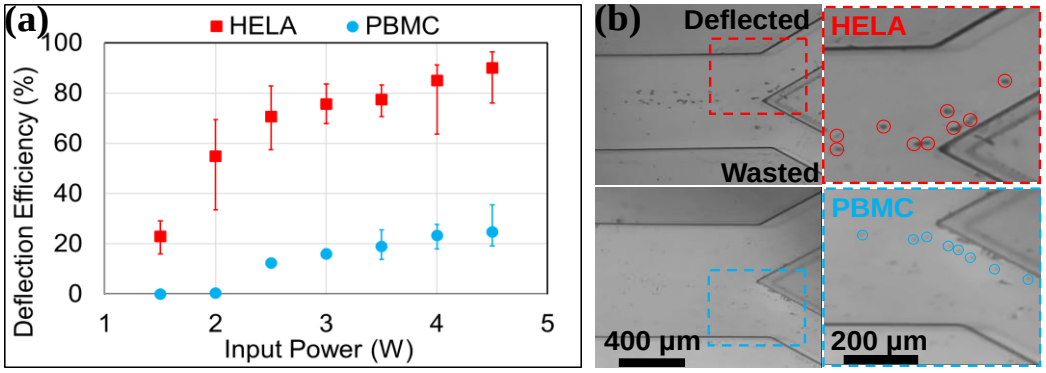

Fig. 6.3 (a) Deflection efficiency of Hela cells and PBMCs under different input powers. (b) Microscopic image of the FTA deflection at the input power of 4 W.

6.4 Conclusion

In this work, a novel FTA device was compared with the CTA in acoustic field simulation and microparticles deflection efficiency. The acoustic pressure was increased compared to the CTA and in good agreement with the numerical results. A 43% reduction of the working area was achieved, which offered a significant reduction in the input power to achieve the same deflection efficiency. According to the successful cells deflection test result, a separation of HeLa cells from PBMCs by the FTA device is possible. As a tilted-angle SSAW device, the novel FTA design has

advantages in lowering energy consumption, evenly distributing the acoustic field pressure, and enhancing acoustic energy.

Chapter 7 Novel acoustic tweezer based on Gallium Nitride compound semiconductor film for cancer cell patterning

As demonstrated in chapter 3, lithium niobate is the conventional piezoelectric material for fabricating SSAW-based acoustic devices. However, at high input powers for high-throughput manipulation, the challenge of breakage of the device was raised during the projects described in chapters 4,5 and 6. LN's very low thermal conductivity caused the joule heating to overly accumulate during device operation and then led to the breakage of the lithium niobate substrate. In chapter 6, the optimisation to this problem was implemented by changing the IDT design on the substrate. This chapter aims to demonstrate the optimization of acoustofluidic cell manipulation achieved by substituting the piezoelectric substrate material to Gallium Nitride (GaN). The work in chapter 7 has been published in IEEE Transactions on Electron Devices, 2020.

7.1 Introduction of Gallium Nitride based acoustic tweezer

Gallium Nitride (GaN) is a compound semiconductor that has resulted in the revolution in performance and efficiency of light-emitting diode (LED) and power transistors(Amano et al., 2018). GaN has tremendous potential to facilitate new functionality over and beyond the silicon-based semiconductor industry, which is currently faced with diminishing performance returns versus cost. The distinct properties of GaN, its wide bandgap, high breakdown electric field, and high electron mobility, make it an excellent candidate for the next-generation power electronics(Kuzmik, 2001, Baliga, 2013), high-frequency communications(Eblabla et

al., 2017), and photonic applications(Kako et al., 2006). GaN is also known as a robust piezoelectric material for fabricating acoustic resonators and diverse electromechanical devices required to operate in harsh environments. Its biocompatibility and stability in aqueous environments have previously been demonstrated(Jewett et al., 2012). Recently, it has been reported that GaN exhibits great potentials in biosensing(Kirste et al., 2015), interacting with cells(Snyder et al., 2018), and integrating with optoelectronics and transistors for sensor applications(Calle et al., 2005).

A common piezoelectric material used for fabricating acoustic tweezers based on SAW is lithium niobate $LiNbO_3$. However, bulk $LiNbO_3$-based SAW devices are generally brittle so that great care of handling and cooling is required to prevent thermal stress breakage of the $LiNbO_3$(Wu et al., 2017b, Wu et al., 2019a) when the device is operated at high input voltage/power. It limits the stability and performance of using these devices in high-throughput applications. Many III–V compound semiconductors including GaN, ZnO, and AlN show desired characteristics for SAW-based applications such as high-temperature stability, low propagation loss, high SAW velocity, smooth surface, and high thermal conductivity(Fu et al., 2017). ZnO provides a slightly higher electromechanical coupling coefficient but has a low wave propagation velocity and shows high leakage, thus limiting its uses at very high frequency. Also, its chemical stability and corrosion resistance are potential issues. In addition, zinc is a dopant of silicon and its monolithic integration with silicon complementary metal-oxide-semiconductor (CMOS) circuits is challenging(Harmeet Bhugra, 2017). GaN can be manufactured as thin-film piezoelectric material since the acoustic velocity in GaN is very close to silicon which could result in low acoustic loss/mismatch(Rais-Zadeh et al., 2014). In addition, the high performance that can be achieved in GaN electronic and optical devices offers a multitude of integration opportunities such as monolithic integration with control electronics based on GaN

power amplifiers and optoelectronic devices to realize functionally diverse modules and versatile labs-on-a-chip. Table. 9.1 compares the key properties between GaN and $LiNbO_3$, which show that GaN has a smaller effective coupling factor but much higher thermal conductivity.

Table. 7.1 Comparison of properties between GaN AND $LiNbO_3$

	Thermal conductivity (W/(cm·K))	Elastic modulusC_{33} (GPa)	k_{eff}^2 (%)
GaN	1.3(Kamatagi et al., 2007)	398(Rais-Zadeh et al., 2014)	2(Popa and Weinstein, 2014)
$LiNbO_3$	0.044(Yao et al., 2008)	235(Ledbetter et al., 2004)	5-12(Fu et al., 2017)

In addition, it has also been demonstrated that 2-D electron gases (2DEGs) on which GaN high electron mobility transistors (HEMTs) are based, can be used as interdigital transducers (IDTs) in SAW devices, thus eliminating the mass loading and signal reflection caused by metal IDTs(Wong et al., 2007). Such properties along with the maturity of GaN device manufacturing on large wafer sizes make GaN a perfect choice for fabricating acoustic devices to monolithically integrate with power amplifier made by HEMTs for high-frequency, high-power, and high-temperature operation, with significantly reduced size, weight, and costs(Rais-Zadeh et al., 2014). Despite extensive research that has been devoted to GaN, only limited attention has been paid to the implementation of GaN into acoustofluidic devices.

In this chapter, a novel GaN-based acoustic tweezer (GaNAT) for manipulating live biological cells and polystyrene microspheres is described. The GaNAT demonstrated the capability to operate at high power with minimal need of cooling to trap and manipulate microparticles and biological cells while keeping high cell viability. The integration of GaN with microfluidics and the potential of using GaN in new generation nano- and microelectromechanical systems (N/MEMS) will allow hitherto

unobtainable levels of integration and compatibility of GaN with the electroacoustic, electronic systems, and semiconductor system in particular.

7.2 Mechanism of GaNAT

A schematic of the GaNAT is shown in Fig. 7.1a. Comblike metallic electrodes were patterned onto the GaN thin film grown on a sapphire substrate to form the IDTs. A PDMS microchannel was then bonded between the two IDTs for accommodating fluid samples containing microparticles/cells. The GaNAT was driven by applying RF signals to generate SAWs with amplitudes of picometers to nanometers, which are propagating on the surface of the GaN layer. Fig. 7.1b shows the counterpropagating SAWs generated by the IDTs to create an SSAW on the GaN layer. Microparticles simultaneously experience a Stokes' drag force, Fdrag, when they are moving in the fluid. Buoyancy and gravitational forces are generally negligible. Polystyrene microspheres and biological cells typically possess a positive acoustic contrast factor which allows them to be attracted towards the nearest PN(Faridi et al., 2017).

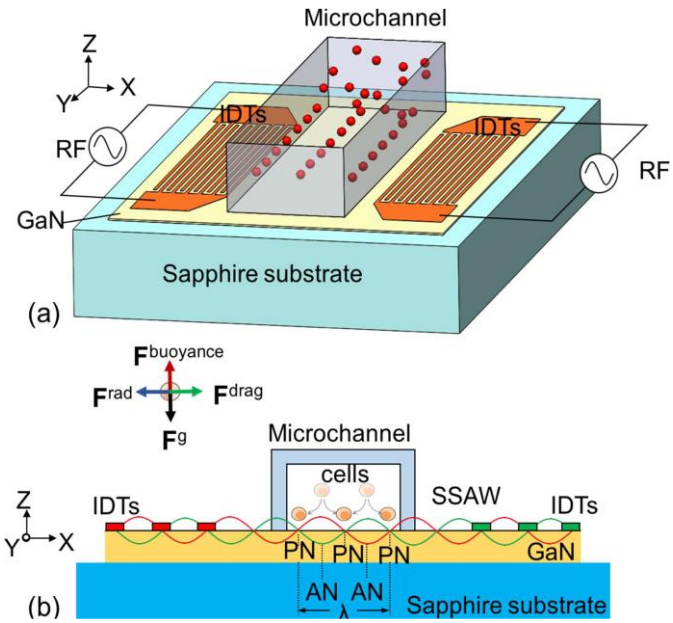

Fig. 7.1 (a) Schematic of GaNAT. (b) Four types of forces applied on a particle inside the GaNAT and the cell patterning on PNs driven by SSAWs generated by GaN IDTs.

7.3 Device fabrication and setup

The fabricated GaNAT device is shown in Fig. 7.2a. Comblike metallic electrodes were patterned onto a ~4.5-μm-thick undoped GaN thin film grown on a ~600-μm-thick sapphire substrate. Patterning of the IDTs was done by using conventional photolithography. A positive photoresist (EPI680, Everlight Advanced Chemicals Ltd., Suzhou, China) was used for spinning on the substrate followed by mask alignment. The metal bilayers (Cr/Au, 30/150 nm) were deposited onto the patterned wafer using a magnetron sputtering system (LLJGP-560, SKY Technology Development, Shenyang, China). The chromium layer was used to provide adequate adhesion between the gold electrodes and the GaN thin film. The wafer was then placed into acetone to perform a wet etching process. Then, the wafer was cleaned with ethanol, deionized water, and dried with nitrogen. The width and gap of the finger electrodes

are both 70 μm, which gives an SSAW wavelength λ of = 280 μm. The two IDTs' centre-to-centre spacing was 18 λ and each IDT consisted of 40 pairs of finger electrodes. A silicone mould for making the PDMS microchannel with the channel dimension of 1 cm (L) × 280 μm (W) × 60 μm (H) was manufactured using a standard soft-lithography process. The microchannel was made of PDMS by a standard manufacturing process. The PDMS microchannel was mechanically bonded to the centre of the GaN SAW device (between the two IDTs) to construct the GaNAT (Fig. 7.2a). The GaNAT was mounted onto a heatsink [10 cm (L) × 10 cm (W) × 4 cm (H)] coupling by thermal grease. Inlet and outlet tubes were connected to the microchannel for flowing fluid samples.

The experimental configuration is shown in Fig. 7.2b. The RF signal produced by a signal generator was amplified by a power amplifier and then coupled onto the GaNAT. To enable the maximum RF power delivered from the power amplifier to the IDTs for actuating microparticles/cells, impedance matching networks were designed for both the IDTs. The forward and reflected powers of each IDT were monitored using two power meters.

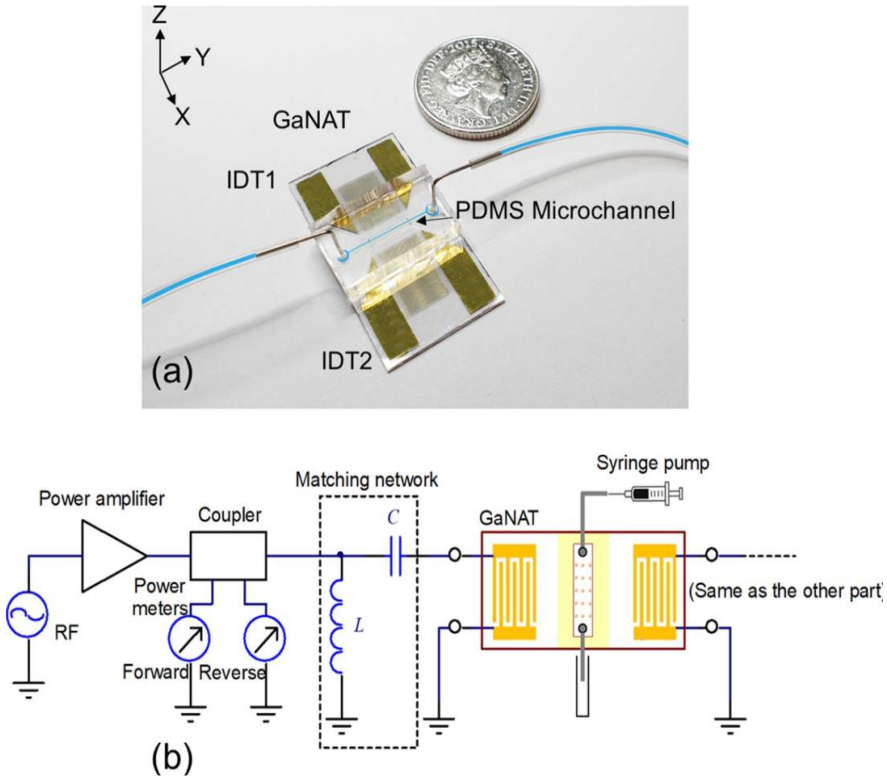

Fig. 7.2 GaNAT and the experiment. (a) Photograph of GaNAT consisted of the GaN IDTs bonded with the PDMS microchannel. (b) Test and experiment setup of the GaNAT.

7.4 Characterisation of the GaNAT

To investigate how the bonded microchannel affects the transfer functions of the GaN SAW device, a VNA was used to measure the transfer functions of the two IDTs, S_{11} (reflection coefficient) and S_{21} (transmission coefficient), with and without the microchannel in place. The IDT's surface temperature was seen to increase using an infrared thermal camera (ETS320, FLIR, USA), with increasing input power. The measuring point was set on the metal electrodes which produced most joule heat to represent the highest temperature on the GaNAT. The spatial resolution of the thermal

camera is 21 μm, which is approximately one-third of the width of the finger electrodes. Due to the RF excitation that induces Joule effect on finger electrodes(Thevenard et al., 2016), the camera's spatial resolution can accurately detect the temperature distribution on the IDTs after correcting for the emissivity of the material. The temperature was measured without microchannel and each measurement was taken once the temperature reading stabilized.

To investigate the SAW amplitude produced on the GaNAT and compare with that of a conventional $LiNbO_3$ SAW device, an SAW device made from $LiNbO_3$ with the similar frequency (20 MHz) was fabricated. A laser vibrometer (PSV- 500-VH, Polytec, Germany) was used to quantify the SAW amplitudes on both devices under the same input power of 1 W.

The results of S_{11} and S_{21} spectra of the SAW devices without microchannel (solid lines) and with microchannel (dotted lines) are shown in Fig. 7.3a and b, respectively, where the lower frequency peaks at 19.40 MHz correspond to the Rayleigh mode and 38.91 MHz correspond to the Sezawa mode.

Due to the small dispersion value ($kh_{GaN} = 2\pi h_{GaN}/\lambda \approx 0.1$, where k is the wavenumber and h_{GaN} is the thickness of GaN layer), the SAW velocity approximates the acoustic velocity in sapphire, that is, $v_{\mathrm{Ray}}^{\mathrm{sapp}} = 5486$ m/s in the [1100] direction(Pedrós et al., 2004), which gives the calculated Rayleigh frequency as $f = v_{\mathrm{Ray}}^{\mathrm{sapp}}/\lambda \approx 19.59$ MHz. The slight difference between the measured and calculated frequencies may be due to the mismatching between the GaN and sapphire layers. The Rayleigh frequency of 19.40 MHz was used in the following experiments. In general, both the S_{11} and S_{21} parameters show that adding PDMS microchannel does not deteriorate the frequency characteristics of the GaNAT. The relatively small peaks in S_{11} and S_{21} spectra are mainly due to the low thickness of the GaN film. The

electromechanical coupling coefficient, k^2, was estimated to be 0.04% ± 0.005% ($h/\lambda =$ 0.016, h is the layer thickness and is the SAW wavelength) according to the method introduced by Xu and Woods(Xu and Woods, 2010) and Woods and Boroumand(Woods and Boroumand, 2006).

The temperature rise on the IDTs due to the increased forward power and the relationship between forward powers and reverse powers on the IDTs are plotted in Fig. 7.3c. The inset was the thermal image of the IDTs at 10 W. At a room temperature of 24 °C, the temperature on the IDTs was increased to 31 °C at 10 W, which was the maximum power supplied to the GaNAT in this article. Without using any active cooling system such as Peltier cooler, the GaNAT was able to effectively convert RF powers to SAWs while keeping the device temperature below the biological limit.

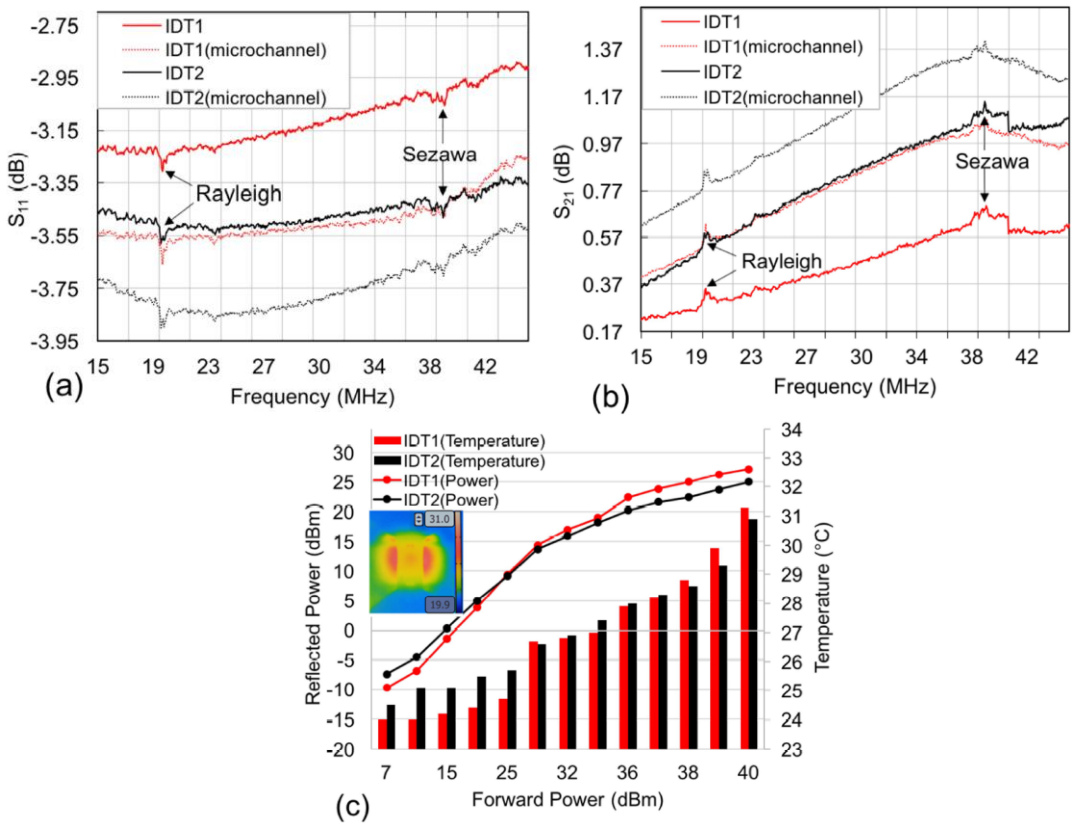

Fig. 7.3 Characterization of GaN IDTs. (a) S_{11} parameter of the two IDTs with and without the presence of the microchannel. (b) S_{21} parameter of the two IDTs with and without the presence of the microchannel. Red and black curves are the parameter for IDT1 and IDT2, respectively. Solid and dotted curves represent the measurement without and with the microchannel. Both the Rayleigh and Sezawa mode frequencies are noted on the curves. (c) Measurement of the temperature of the IDTs and the reflected power while increasing the forward power, inset is the thermal image of the GaN IDTs. The unit dBm is an electrical power unit that is euqal to 10 times base 10 logarithm of the power in miliwatts.

Under an input power of 1 W, the SAW vibration amplitudes at the centre between the two IDTs on the GaNAT and LiNbO3 devices were found to be 123.2 ± 2.4 pm (average ± SD) and 1650.8 ± 16.4 pm (average ± SD), respectively. The smaller vibration amplitude produced by GaN is due to its lower k^2, which implies that the

device would have difficulty in agitating liquid, or transport droplets, but the data shown here clearly demonstrate that it is sufficient to generate the SSAW for manipulation of particles and cells. However, we could improve the k^2 by increasing the GaN film thickness, film quality, or using doped-GaN epilayer(Xu and Woods, 2010). The minimum input powers to fully trap 10-μm polystyrene microspheres to the PNs inside the GaNAT and $LiNbO_3$ devices are 1.9 and 0.2 W, respectively.

7.5 Numerical simulation and manipulation of microspheres

A numerical model was applied to investigate the acoustofluidic conditions of the GaNAT and to predict the trajectory of microparticles(Mao et al., 2016, Muller et al., 2012). The model is valid for the GaNAT as the microchannel length is significantly longer than its height and width. The acoustic waves are uniform and perpendicular to the main flow direction. In this case, the acoustic pressure and microparticle movement can be investigated with a 2-D cross-sectional model. COMSOL Multiphysics version 5.4 was used to solve the first-order acoustic pressure fields and microparticle trajectories.

The simulation results of the acoustic pressure and the microparticle trajectories are shown in Fig. 7.4a–d. Fig. 7.4a demonstrates the first-order acoustic pressure field with no phase difference ($\Delta\varphi = 0^\circ$) between the RF signals driving the two IDTs, which results in the PNs located at the middle and two sides of the microchannel. Fig. 7.4c shows the corresponding microparticle trajectories which produce three microparticle traces on the PNs. The width of the microchannel in this article is the same as the SSAW's wavelength ($\lambda = 280$ μm), allowing the microparticles to aggregate at three positions inside the microchannel. The PN distribution can be achieved by setting the phase difference of the two IDTs to $\Delta\varphi = 0^\circ$. By adding the

phase difference to $\Delta\varphi = 180^\circ$, one can position the ANs to be at the middle and two sides of the microchannel (Fig. 7.4b), which leads to five microparticle traces as shown in Fig. 7.4d. Polystyrene microspheres were then introduced to the GaNAT to test the simulation results. When they were evenly dispersed inside the microchannel, the RF signals with $\Delta\varphi = 180^\circ$ were applied to the GaNAT and then 10-μm polystyrene microspheres were immediately shifted to the three PN traces as the microscopic top-view image shown in Fig. 7.4e. When the RF signals with μm were applied, five microsphere traces were generated inside the microchannel, as shown in Fig. 7.4f. The good agreement between the numerical prediction and experimental observation demonstrated the ability of GaNAT in actuating and trapping microspheres in a controllable pattern.

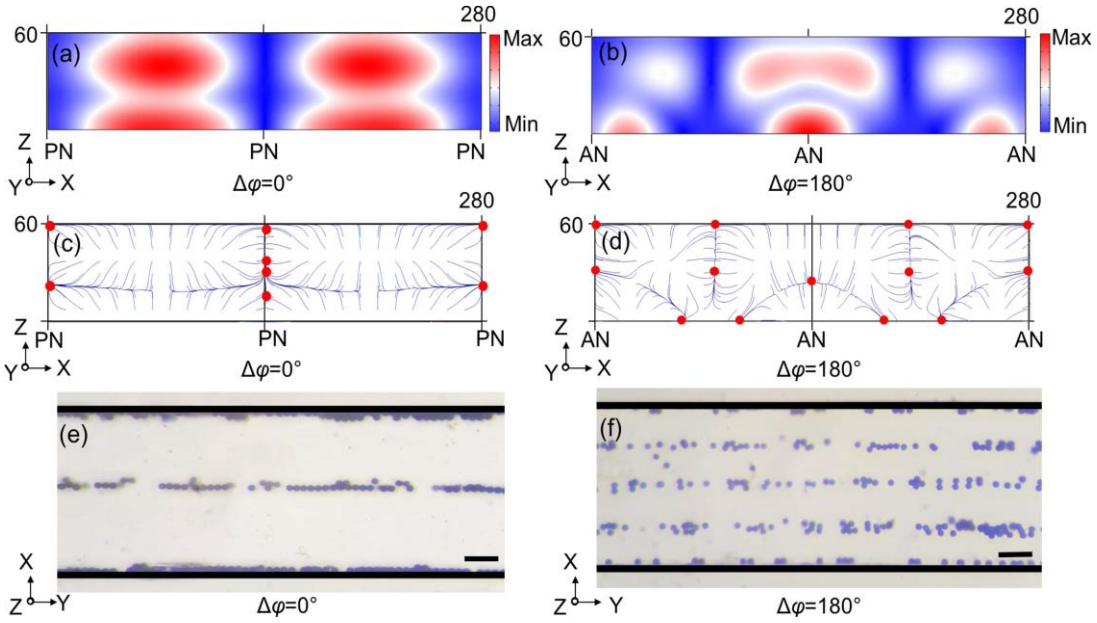

Fig. 7.4 Numerical and experimental studies of the GaNAT. (a) and (b) Acoustic pressure field inside the microchannel for the PN and pressure AN located at the middle of the channel, respectively. (c) and (d) Particle trajectories of 10-μm polystyrene microspheres actuated by the corresponding acoustic pressures in (a) and (b). (e) and (f) Microscope images of the polystyrene microsphere patterned in the GaNAT. The scale bar is 50 μm.

7.6 Manipulation of Cells

Biological cells were used to explore the potential of manipulation cells using the GaNAT and to test whether the GaNAT was able to maintain cell viability during acoustic actuation. Two types of biological cells, for example, mouse renal tumour cells (TSC1-associated tumour cells, Tsc1-204)(Yang et al., 2013) and mouse embryonic fibroblast cells (Tsc1-387-2)(Yang et al., 2015), were prepared for the test. These two types of cells are widely used to investigate mechanisms of tuberous

sclerosis-associated renal tumorigenesis and oncogenic pathway. They are quite different in their sizes, morphologies, and genotypes, and thus are easily recognized in the subsequent analysis. The sizes and viabilities of the cells were measured by a cell counter (NC-3000, Chemometec, Denmark). Mouse renal tumour cells and fibroblast cells were cultured using DMEM containing 10% fetal bovine serum, 50 units/ml penicillin, and 50 μg/ml streptomycin at 37 °C in a humidified incubator with 5% (vol/vol) CO_2 atmosphere. Before introducing to the device, the adherent cells were rendered into suspension by exposure to trypsin, followed by dilution into PBS at a concentration of 1×10^6 cells/ml. Cell samples were stored in Eppendorf tubes within an ice bath to keep the temperature at 4 °C during the experiment. To assess cell viability, acridine orange (30 μg/ml) and diaminophenylindole (100 μg/ml) were used to stain the sample at a ratio of 1:20. The stained sample was pipetted onto a counter slide and analyzed by the cell counter. For the viability study, both the fibroblast and renal tumor cells were divided into two groups: SSAW-on group—cells passing through the GaNAT with SSAW present and SSAW-off group—those without SSAW present. To mimic the flow condition for cell separation, the flow rate of the two groups going through the GaNAT was set to 20 μl/min(Li et al., 2015a).

After the microsphere verification, cells were introduced to the GaNAT. When the PNs were set at the middle and two sides of the microchannel ($\Delta\varphi = 0°$), the cells were aggregated at three traces with the majority trapped in the centre of the microchannel Fig. 7.5a. By switching to 180° phase difference ($\Delta\varphi = 180°$), the three traces immediately changed into five as shown in Fig. 7.5b. The cell trapping patterns agreed well with the numerical prediction and the microsphere results.

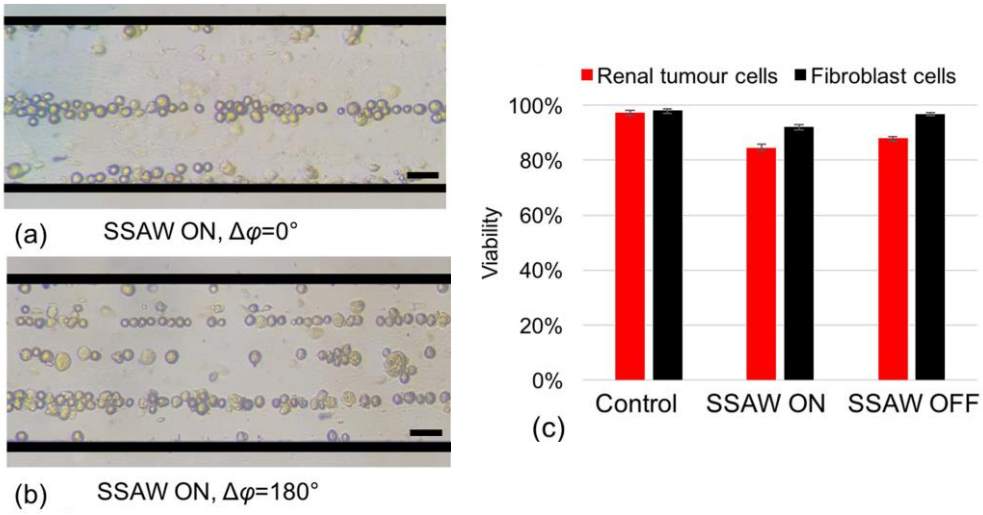

Fig. 7.5 Cell manipulation and viability test. (a) and (b) Cells patterning in the GaNAT for the PN and pressure AN located at the middle of the channel, respectively. (c) Viabilities of the control, SAW on, and SAW off groups. The scale bar is 50 μm.

The cell viabilities of the SSAW on and off groups with the comparison with original samples (control group) were tested and shown in Fig. 7.5c. For the SSAW-on group, the viabilities of the renal tumor cells and fibroblast cells were 84.5% and 92.1%, respectively. For the SSAW-off group, the viabilities were 88.1% and 96.9%, respectively. For these two groups, fibroblast cells showed higher viabilities because they are more tolerable to the changes in temperature and/or CO_2 concentration after they were removed from the incubator. Both the cell types denoted slightly lower viabilities in the SSAW-on group, which is mainly attributed to the heat produced on the chip at high input powers. Nevertheless, both the cell types showed good cell viability after acoustic manipulation using the GaNAT.

7.7 Conclusion

Despite the electromechanical coupling coefficient of GaN being lower than $LiNbO_3$, the use of GaN to develop acoustic tweezer made by GaN-based IDTs working at megahertz frequencies for manipulating cells and microparticles has been demonstrated. As a novel thin-film piezoelectric material for fabricating acoustofluidic devices, GaN/sapphire structure can be used to generate surface acoustic waves. The GaNAT denoted excellent thermal stability when operated at high input power. The thermal performance could be further improved by using Si as a substrate, and this would also offer compatibility with high yield, high volume, and low-cost semiconductor manufacturing to significantly reduce the cost of these devices. The numerical simulation results for the GaNAT were validated using the experimental results of microparticles and cell manipulation. Acoustophoresis realized by the GaNAT will open the area of exploring the multiphysical application of GaN towards monolithic integration with electronics for developing biosensors and N/MEMS.

Chapter 8 Conclusions and future work

8.1 Conclusions

The studies in this thesis denote the design and fabrication methods of the SSAW-based acoustofluidic platform and explore the device optimisation and biological applications based on the platform. As outlined in chapter 1, the ultimate goal of this PhD project was to use the acoustofluidic technique to separate CTCs from the cancer patients whole blood. Although the goal hasn't been achieved, this thesis developed a few novel optimisations and explored some clinical applications of acoustofluidics devices for cells manipulation. Briefly, chapters 1 and 2 demonstrated the introductions and reviews of CTCs detection approaches and SAW-based acoustofluidic cells manipulation, respectively. Chapter 3 detailly described establishing the acoustofluidic manipulation platform from device design to the whole experimental setup. Chapters 4 to 7 focused on the acoustofluidics application from manipulating cell-mimic microparticles to different types of cells, and device optimisation works. Specific conclusions of each chapter which contains essential works are described below.

In chapter 3, the novel development of the FTA IDT design was demonstrated, which had 24 more finger electrodes than CTA IDT to reduce the working area without extra fabrication process and cost. The FTA offers ~32% higher acoustic pressure with the same input power compared with CTA IDT. Moreover, a detailed CR fabrication method was described with the response to different environmental changes during the fabrication, including air bubble control during baking and soft lithography recipe adjustment. In addition, a closed-loop control system in electrical input power control and platform temperature control was established to support the following chapters experiments

In chapter 4, the MATLAB simulation was developed to investigate the performance of microparticles in the parallel IDT device. Polystyrene microspheres separation of 20 μm out of 10 μm and 15 μm out of 5 μm was achieved with a separation efficiency of around 90%. The experimental data was in quantitative agreement with the simulation trend. This chapter provided guidance in using electrical input power, and handling manipulated samples for the following acoustofluidics manipulation work in chapters 5 and 6.

In chapter 5, the CTA IDT devices were applied for washing MEF cells after electroporation from the original medium. The eTE percentage of washed cells (43.8%) is larger than the control group (18.4%). In addition, the viability of washed cells after (94.5%) was significantly higher than the control group (34.3%). The acoustofluidic cell washing improved the electroporation efficiency and cells viability as a post-process.

In chapter 6, the novel FTA IDT device required only ~57% electrical input power of the CTA to achieve the same particles deflection efficiency. The FTA device was applied to deflect the Hela cancer cells and PMBCs, separately. The deflection efficiencies for the HeLa cells and PBMCs were ~90% and ~25%, respectively, at the input power of 4.5 W while maintaining a similar cell viability of 90% as the CTA device. Although the separation experiments haven’t proceeded, the cells deflection result showed the possibility to separate the cancer cells from normal blood cells.

In chapter 7, a novel thin-film piezoelectric material GaN was developed for acoustofluidic manipulation devices. The GaNAT denoted excellent thermal stability when operated at high input power. It overcomes the challenges raised by the conventional LN substrate used in acoustofluidic devices, which were caused by high temperature and high electrical input power. The numerical simulation results for the GaNAT were validated using the experimental results of microparticles and mouse

renal tumour cells manipulation.

8.2 Future work

The cooling control of acoustofluidic devices has been demonstrated in chapter 3. There were always back-and-forth variations around the set value of temperature. The controller may need to be changed or self-designed with the following functions: first, rapid response to the difference from the set temperature. The rapid response can decrease the preparation time. Second, precise control of the temperature drop rate and preventing over cooling. Acoustic properties of piezoelectric substrate and samples medium will change with the temperature. Thus the temperature of the platform needs to be closed around the set value.

Most of the components used in the studies are commercial units that are relatively large and need numerous cables to connect. It limits the flexibility of acoustofluidic manipulation devices when transporting the whole setup to collaborators. Future work may include building modules to integrate these components for further research work.

In chapter 4, a numerical model was established to investigate the electrical input power and the microparticles performance in the acoustofluidic device. Future work may focus on the device's function oppositely: the acoustofluidics platform can be used to identify the physical properties, or acoustic properties, of the samples flowing through the device by observing the performance of the samples at identical electrical input powers. It could become a biomarker-independent flow-cytometry technique.

In chapters 5, 6 and 7, the cells samples were flowing through the acoustofluidic devices. Because the cells were stickier than polystyrene microparticles, cells bond to the surface of the flow path, such as tubings, microchannels, collectors can cause

sample loss. The concentration of CTCs in cancer patients' blood is significantly low. High sample loss of acoustofluidic devices can have a huge impact on the CTCs capturing result. Therefore, coating flow path or modification of samples medium will be essential to future cell manipulation work, especially for CTCs detection.

In chapter 6, the deflection efficiency of Hela cancer cells and PBMCs indicated that it is possible to separate one from the other, but it needs further experiments to prove. Furthermore, the cancer cells used in chapter 6 are normally used for preliminary validation. There are always size, density or compressibility differences between real CTCs and cancer cell lines. The physical properties of CTCs from the same type of cancer can also vary. In addition, the red blood cells with a significantly high concentration in peripheral blood can lead to microfluidic channel blockage. Although a pre-centrifugation or red blood cells lysis can help, these extra procedures can result in the loss of CTCs. Therefore future works to separate CTCs via acoustofluidic platforms need to consider all these variables and uncertainties.

In chapter 7, the GaN substrate was demonstrated to handle high temperature and electrical input power, leading to a larger cell manipulation throughput. However, the high temperature can damage the cells, so that the tolerance of high temperature of GaN is not largely attractive for cells manipulation. Moreover, using GaN with larger electrical input power than conventional LN can be a trade-off. The ratio of the electrical input to mechanical vibration on LN is larger than on GaN. Thus LN can be used to manipulate larger particles which is easy to be actuated while consuming less electrical power. For much smaller particles, such as nanoparticles, GaN can be recommended due to its capability to handle much larger electrical input power. Acoustofluidic devices with GaN substrates need to be tested with nano-samples for a comprehensive understanding in the future.

In summary, although the ultimate goal of this PhD project, which is separating CTCs

from cancer patients' blood via acoustofluidic manipulation, has not been achieved, this thesis extends the understanding of SAW-based acoustofluidic manipulation. It will enable the further development of acoustofluidic manipulation techniques and IDT designs for clinical or chemical applications.

Appendices

Appendix 1 MATLAB codes for general parameters settings

```
clc;clear;close
%%%%%%%%%%%%%%%%%%% Beads starting point
(m) %%%%%%%%%%%%%%%%%%%%
P=0.17;%Power input (watt)
PF=0.45;%power factor
WF=2/17;% Sample flow width factor
rshs=3; %Sheath to sample ratio
frs=5; %sample flow rate (ul/min)
wavelength=200e-6;% acoustic wavelength (m)
d1=20e-6;% the diameter of particle 1 (m)
d2=15e-6;% the diameter of particle 2 (m)
%%%%%%%%%%%% channel set-up %%%%%%%%%%%%%%%%%%
hc=60e-6; %channel height(m)
wc=120e-6; %channel width(m)
L=10e-3;%length of acoustic region (m)
W=3e-3;%width of acoustic region (m)
A1=L*W;%acoustic area
%%%%%%%%%%%% sample set-up %%%%%%%%%%%%%%%%%%
Z=17437.5e3;% acoustic impendance (Ohm)?
cm=3.48e-10;% media comporessibility (pa^-1)
pp=1050;%particle denstiy (kg/m^3)
cp=1.5e-10;%particle compressibility (pa^-1)
pm=1050.5%media density (kg/m^3);
u=0.0016408;%fluid viscosity(Pa*s)
K=((5*pp-2*pm)/(2*pp+pm))-(cp/cm); %acoustic contrast factor
d=20e-6;% the diameter of particle    (m)
%%%%%%%%%%%%fluidic data%%%%%%%%%%%%
frsh=frs*rshs; %sheat flow rate (ul/min)
ft=(frs+2*frsh); %total flow rate (m3/s)
w=WF*(frs/ft*120)*1e-6;% sample flow width (um)
w1=WF*(frs/ft*120);% sample flow width (different unit for ploting)
Acc=hc*wc; %channel crosssection area(m2)
vp=ft/Acc/6e10;%Particles flow speed (m/s)
t=L/vp;%particles traveling time
xr=x*1e-6;%lateral position of particles
```

Appendix 2 MATLAB codes for investigating the relationship between electrical input power and deflection distance of the microparticles.

```
i=1;
Zout=zeros(1,101);
Zoutout=zeros(3,101); % plot ponints on y-axis
for b= [1e-9 6e-6];
x=b; % particles starting point
for a=5e-6;
d=a;% the diameter of particle
n=1;
for P=0:0.063:6.3; %Power input is 3W
k=(pi^2/9)*(d^2/wavelength^2)*((PF*P*Z)/A1)*((cm*K)/u);
A=tan(((2*pi)/wavelength)*x);
B=exp(k.*t);
C=atan(A.*B);
xf=(wavelength/(2*pi)).*C*1e6;
Zout(n)=xf;
n=n+1;
end
end
Zoutout(i,:)=Zout;
i=i+1;
end
%%%%%%%%%%%%%%%%%%% plot %%%%%%%%%%%%%%%%%%%
P=0:0.063:6.3;
plot(P,Zoutout(1,:));
hold on
plot(P,Zoutout(2,:));
hold on
plot(P,Zoutout(3,:));
axis([0,6.3,0,55]);
xlabel('Input Power/w');
ylabel('Separation distance/um ')
```

Appendix 3 MATLAB codes for investigating the relationship between electrical input power and acoustic radiation force applied on the microparticles.

```
Zout=zeros(1,100);
i=1;
for a=[0.02 0.22];
P=a; % Input power (watt)
n=1;
for b= -50e-6:1e-6:50e-6;
x=b; % particles position point
Fa=pi^2*(PF*P*Z/A1)*d^3/12/wavelength*cm*K*sin(4*pi*x/wavelength);
Zout(n)=Fa;
n=n+1;
end
Zoutout(i,:)=Zout;
i=i+1;
end
%%%%%%%%%%%%%%%%%%% plot %%%%%%%%%%%%%%%%%%%
x0= -50:1:50;
plot(x0,Zoutout(1,:));
hold on
plot(x0,Zoutout(2,:));
hold on
plot(x0,Zoutout(3,:));
```

Appendix 4 MATLAB codes for investigating the relationship between electrical input power and the distribution of microparticles at the outlet area.

```
k1=(pi^2/9)*(d1^2/wavelength^2)*((PF*P*Z)/A1)*((cm*K)/u);
k2=(pi^2/9)*(d2^2/wavelength^2)*((PF*P*Z)/A1)*((cm*K)/u);
D=((2*pi)/wavelength)*xr;
A=tan(D);
B1=exp(k1*t);
B2=exp(k2*t);
C1=atan(A.*B1);
C2=atan(A.*B2);
xfa=(wavelength/(2*pi)).*C1*1e6; %final position of particles after acoustic filtration (1e6 is for ploting in um)
xfb=(wavelength/(2*pi)).*C2*1e6;
fx=(((6/w^3).*(w/2-xr).*(w/2+xr)))*1e-4;%probability density function of particles before acoustic field
%%%%%%%%%%%%%%%%%% plot %%%%%%%%%%%%%%%%%%
hold on;
gx1=(fx.*((1/B1)+B1.*A.^2).*(1./sec(D).^2));
gx2=(fx.*((1/B2)+B2.*A.^2).*(1./sec(D).^2));
h2=plot(xfa,gx1);
hold on;
h3=plot(xfb,gx2);
axis([-60 60 0 20]);
SS1=trapz(x,fx);
SS21a=find(xfa>-40&xfa<40);% (not separated)
SS21b=find(xfb>-40&xfb<40);% (not separated)
xf2a=xfa(SS21a);
xf2b=xfb(SS21b);
gx2a=gx1(SS21a);
gx2b=gx2(SS21b);
SS2a=trapz(xf2a,gx2a);
SS2b=trapz(xf2b,gx2b);
Rrema=(1-SS2a/SS1)*100%removal rate
str = {'20 um removal rate',num2str(Rrema)};
text(-8,10,str)
text(6,9.5,'%')
Rremb=(1-SS2b/SS1)*100 %removal rate
str = {'15 um removal rate',num2str(Rremb)};
text(-8,15,str)
text(6,14.5,'%')
```

```
xlabel('Lateral Position (um)');
ylabel('Polystyrene microsphere distribution ');
chx=linspace(-40,-40,100);
chy=linspace(0,20,100);
hold on;
plot(chx,chy,'k-.');
chx2=linspace(40,40,100);
chy2=linspace(0,20,100);
hold on;
plot(chx2,chy2,'k-.');
fill([-60 -60 -40 -40],[20 19 19 20],'g','edgealpha',0);
fill([40 40 60 60],[20 19 19 20],'g','edgealpha',0);
fill([-40 -40 40 40],[20 19 19 20],'y','edgealpha',0);
legend([h2,h3],strcat(num2str (d1*1e6),'um'),strcat(num2str (d2*1e6),'um'));
text(-58,19.5,'separated');
text(-2.15,19.5,'Centre');
text(42,19.5,'separated');
```

Bibliography

ADAMS, A. A., OKAGBARE, P. I., FENG, J., HUPERT, M. L., PATTERSON, D., GöTTERT, J., MCCARLEY, R. L., NIKITOPOULOS, D., MURPHY, M. C. & SOPER, S. A. 2008. Highly efficient circulating tumor cell isolation from whole blood and label-free enumeration using polymer-based microfluidics with an integrated conductivity sensor. *J Am Chem Soc,* 130**,** 8633-41.

AHMED, S., WANG, W., MAIR, L. O., FRALEIGH, R. D., LI, S., CASTRO, L. A., HOYOS, M., HUANG, T. J. & MALLOUK, T. E. 2013. Steering Acoustically Propelled Nanowire Motors toward Cells in a Biologically Compatible Environment Using Magnetic Fields. *Langmuir,* 29**,** 16113-16118.

AHN, J. C., TENG, P.-C., CHEN, P.-J., POSADAS, E., TSENG, H.-R., LU, S. C. & YANG, J. D. 2020. Detection of Circulating Tumor Cells and Their Implications as a Biomarker for Diagnosis, Prognostication, and Therapeutic Monitoring in Hepatocellular Carcinoma. *Hepatology,* n/a.

ALLARD, W. J., MATERA, J., MILLER, M. C., REPOLLET, M., CONNELLY, M. C., RAO, C., TIBBE, A. G., UHR, J. W. & TERSTAPPEN, L. W. 2004. Tumor cells circulate in the peripheral blood of all major carcinomas but not in healthy subjects or patients with nonmalignant diseases. *Clinical cancer research,* 10**,** 6897-6904.

AMANO, H., BAINES, Y., BEAM, E., BORGA, M., BOUCHET, T., CHALKER, P. R., CHARLES, M., CHEN, K. J., CHOWDHURY, N., CHU, R., DE SANTI, C., DE SOUZA, M. M., DECOUTERE, S., DI CIOCCIO, L., ECKARDT, B., EGAWA, T., FAY, P., FREEDSMAN, J. J., GUIDO, L., HäBERLEN, O., HAYNES, G., HECKEL, T., HEMAKUMARA, D., HOUSTON, P., HU, J., HUA, M., HUANG, Q., HUANG, A., JIANG, S., KAWAI, H., KINZER, D., KUBALL, M., KUMAR, A., LEE, K. B., LI, X., MARCON, D., MäRZ, M., MCCARTHY, R., MENEGHESSO, G., MENEGHINI, M., MORVAN, E., NAKAJIMA, A., NARAYANAN, E. M. S., OLIVER, S., PALACIOS, T., PIEDRA, D., PLISSONNIER, M., REDDY, R., SUN, M., THAYNE, I., TORRES, A., TRIVELLIN, N., UNNI, V., UREN, M. J., VAN HOVE, M., WALLIS, D. J., WANG, J., XIE, J., YAGI, S., YANG, S., YOUTSEY, C., YU, R., ZANONI, E., ZELTNER, S. & ZHANG, Y. 2018. The 2018 GaN power electronics roadmap. *Journal of Physics D: Applied Physics,* 51**,** 163001.

ANGLE. 2019. *Parsortix® PR1 system: Capture and harvest of circulating tumor cells from blood* [Online]. Available: https://angleplc.com/library/product-information/ [Accessed 25th Jan 2021].

ANTFOLK, M., MAGNUSSON, C., AUGUSTSSON, P., LILJA, H. & LAURELL, T. 2015. Acoustofluidic, Label-Free Separation and Simultaneous Concentration of Rare Tumor Cells from White Blood Cells. *Analytical Chemistry,* 87**,** 9322-9328.

ARMSTRONG, J. P. K., MAYNARD, S. A., PENCE, I. J., FRANKLIN, A. C., DRINKWATER, B. W. & STEVENS, M. M. 2019. Spatiotemporal quantification of acoustic cell patterning using Voronoï tessellation. *Lab on a Chip,* 19**,** 562-573.

ARUMUGAM, T., RAMACHANDRAN, V., FOURNIER, K. F., WANG, H., MARQUIS, L., ABBRUZZESE, J. L., GALLICK, G. E., LOGSDON, C. D., MCCONKEY, D. J. & CHOI, W. 2009. Epithelial to mesenchymal transition contributes to drug resistance in pancreatic cancer. *Cancer Res,* 69**,** 5820-8.

AUGUSTSSON, P., BARNKOB, R., WERELEY, S. T., BRUUS, H. & LAURELL, T. 2011. Automated and temperature-controlled micro-PIV measurements enabling long-term-stable microchannel acoustophoresis characterization. *Lab on a Chip,* 11**,** 4152-4164.

AUGUSTSSON, P., KARLSEN, J. T., SU, H.-W., BRUUS, H. & VOLDMAN, J. J. N. C. 2016. Iso-acoustic focusing of cells for size-insensitive acousto-mechanical phenotyping. 7**,** 11556.

AYAN, B., OZCELIK, A., BACHMAN, H., TANG, S.-Y., XIE, Y., WU, M., LI, P. & HUANG, T. J. 2016. Acoustofluidic coating of particles and cells. *Lab on a Chip,* 16**,** 4366-4372.

BACCELLI, I., SCHNEEWEISS, A., RIETHDORF, S., STENZINGER, A., SCHILLERT, A., VOGEL, V., KLEIN, C., SAINI, M., BäUERLE, T., WALLWIENER, M., HOLLAND-LETZ, T., HöFNER, T., SPRICK, M., SCHARPFF, M., MARMé, F., SINN, H. P., PANTEL, K., WEICHERT, W. & TRUMPP, A. 2013. Identification of a population of blood circulating tumor cells from breast cancer patients that initiates metastasis in a xenograft assay. *Nat Biotechnol,* 31**,** 539-44.

BALBOA, D., WELTNER, J., EUROLA, S., TROKOVIC, R., WARTIOVAARA, K. & OTONKOSKI, T. J. S. C. R. 2015. Conditionally stabilized dCas9 activator for controlling gene expression in human cell reprogramming and differentiation. 5**,** 448-459.

BALIC, M., DANDACHI, N., HOFMANN, G., SAMONIGG, H., LOIBNER, H., OBWALLER, A., VAN DER KOOI, A., TIBBE, A. G., DOYLE, G. V., TERSTAPPEN, L. W. & BAUERNHOFER, T. 2005. Comparison of two methods for enumerating circulating tumor cells in carcinoma patients. *Cytometry B Clin Cytom,* 68**,** 25-30.

BALIGA, B. J. 2013. Gallium nitride devices for power electronic applications. *Semiconductor Science and Technology,* 28**,** 074011.

BANKó, P., LEE, S. Y., NAGYGYöRGY, V., ZRíNYI, M., CHAE, C. H., CHO, D. H. & TELEKES, A. 2019. Technologies for circulating tumor cell separation from whole blood. *Journal of hematology & oncology,* 12**,** 48.

BARNKOB, R., AUGUSTSSON, P., LAURELL, T. & BRUUS, H. 2010. Measuring the local pressure amplitude in microchannel acoustophoresis. *Lab on a Chip,* 10**,** 563-570.

BERKOWSKI, K. L., PLUNKETT, K. N., YU, Q. & MOORE, J. S. 2005. Introduction to Photolithography: Preparation of Microscale Polymer Silhouettes. *Journal of Chemical Education,* 82**,** 1365.

BOSTONPIEZOOPTICS.COM. *Lithium Niobate Physical Properties* [Online]. Available: https://www.bostonpiezooptics.com/assets/pdf/Lithium_Niobate.pdf [Accessed 11 Feb 2021].

BRAY, F., FERLAY, J., SOERJOMATARAM, I., SIEGEL, R. L., TORRE, L. A. & JEMAL, A. 2018. Global cancer statistics 2018: GLOBOCAN estimates of incidence and mortality worldwide for 36 cancers in 185 countries. *CA Cancer J Clin,* 68**,** 394-424.

BROWN, J. C., RHIM, A. D., MANNING, S. L., BRENNAN, L., MANSOUR, A. I., RUSTGI, A. K., DAMJANOV, N., TROXEL, A. B., RICKELS, M. R., KY, B., ZEMEL, B. S., COURNEYA, K. S. & SCHMITZ, K. H. 2018. Effects of exercise on circulating tumor cells among patients with resected stage I-III colon cancer. *PLOS ONE,* 13**,** e0204875.

BUREAU, M. F., NAIMI, S., TORERO IBAD, R., SEGUIN, J., GEORGER, C., ARNOULD, E., MATON, L., BLANCHE, F., DELAERE, P. & SCHERMAN, D. 2004. Intramuscular plasmid DNA electrotransfer: biodistribution and degradation. *Biochimica et biophysica acta,* 1676**,** 138-148.

CALLE, F., PEDRóS, J., PALACIOS, T. & GRAJAL, J. 2005. Nitride-based surface acoustic wave devices and applications. *physica status solidi (c),* 2**,** 976-983.

CAMPTON, D. E., RAMIREZ, A. B., NORDBERG, J. J., DROVETTO, N., CLEIN, A. C., VARSHAVSKAYA, P., FRIEMEL, B. H., QUARRE, S., BREMAN, A., DORSCHNER, M., BLAU, S., BLAU, C. A., SABATH, D. E., STILWELL, J. L. & KALDJIAN, E. P. 2015. High-recovery visual identification and single-cell retrieval of circulating tumor cells for genomic analysis using a dual-technology platform integrated with automated immunofluorescence staining. *BMC Cancer,* 15**,** 360.

CAULEY, C. E., PITMAN, M. B., ZHOU, J., PERKINS, J., KULEMAN, B., LISS, A. S., FERNANDEZ-DEL CASTILLO, C., WARSHAW, A. L., LILLEMOE, K. D. & THAYER, S. P. 2015. Circulating Epithelial Cells in Patients with Pancreatic Lesions: Clinical and Pathologic Findings. *J Am Coll Surg,* 221**,** 699-707.

CEN, P., NI, X., YANG, J., GRAHAM, D. Y. & LI, M. 2012. Circulating tumor cells in the diagnosis and management of pancreatic cancer. *Biochimica et Biophysica Acta (BBA)-Reviews on Cancer,* 1826**,** 350-356.

CERVIA, L. D., CHANG, C. C., WANG, L., MAO, M. & YUAN, F. 2018. Enhancing Electrotransfection Efficiency through Improvement in Nuclear Entry of Plasmid DNA. *Mol Ther Nucleic Acids,* 11**,** 263-271.

CERVIA, L. D. & YUAN, F. 2018. Current Progress in Electrotransfection as a Nonviral Method for Gene Delivery. *Molecular Pharmaceutics,* 15**,** 3617-3624.

CHAFFER, C. L., THOMPSON, E. W. & WILLIAMS, E. D. 2007. Mesenchymal to epithelial transition in development and disease. *Cells Tissues Organs,* 185**,** 7-19.

CHAFFER, C. L. & WEINBERG, R. A. 2011. A perspective on cancer cell metastasis. *Science,* 331**,** 1559-64.

CHIN, M. L. 2006. A fabrication study of surface acoustic wave devices for magnetic field detection.

CIFANI, N., CHRONOPOULOU, L., POMPILI, B., DI MARTINO, A., BORDI, F., SENNATO, S., DI DOMENICO, E. G., PALOCCI, C. & ASCENZIONI, F. 2015. Improved stability and efficacy of chitosan/pDNA complexes for gene delivery. *Biotechnology letters,* 37**,** 557-565.

CLARKE, M. F., DICK, J. E., DIRKS, P. B., EAVES, C. J., JAMIESON, C. H. M., JONES, D. L., VISVADER, J., WEISSMAN, I. L. & WAHL, G. M. 2006. Cancer Stem Cells—Perspectives on Current Status and Future Directions: AACR Workshop on Cancer Stem Cells. *Cancer Research,* 66**,** 9339-9344.

COHEN, S. J., PUNT, C., IANNOTTI, N., SAIDMAN, B. H., SABBATH, K. D., GABRAIL, N. Y., PICUS, J., MORSE, M., MITCHELL, E. & MILLER, M. C. 2008. Relationship of circulating tumor cells to tumor response, progression-free survival, and overall survival in patients with metastatic colorectal cancer. *Clin Oncol,* 26**,** 3213-3221.

COLLINS, D. J., DEVENDRAN, C., MA, Z., NG, J. W., NEILD, A. & AI, Y. 2016. Acoustic tweezers via sub–time-of-flight regime surface acoustic waves. *Science advances,* 2**,** e1600089.

COSTA, J. A. V. & DE MORAIS, M. G. 2014. Chapter 1 - An Open Pond System for Microalgal Cultivation. *In:* PANDEY, A., LEE, D.-J., CHISTI, Y. & SOCCOL, C. R. (eds.) *Biofuels from Algae.* Amsterdam: Elsevier.

COURT, C. M., ANKENY, J. S., SHO, S. & TOMLINSON, J. S. 2016. Circulating Tumor Cells in Gastrointestinal Cancer: Current Practices and Future Directions. *In:* BENTREM, D. & BENSON, A. B. (eds.) *Gastrointestinal Malignancies.* Cham: Springer International Publishing.

COX, D. B. T., PLATT, R. J. & ZHANG, F. J. N. M. 2015. Therapeutic genome editing: prospects and challenges. 21**,** 121.

CRAENE, B. D. & BERX, G. 2013. Regulatory networks defining EMT during cancer initiation and progression. *Nature Reviews Cancer,* 13**,** 97-110.

CRISAN, D., RUARK, D. S., DECKER, D. A., DREVON, A. M. & DICARLO, R. G. 2000. Detection of circulating epithelial cells after surgery for benign breast disease. *Mol Diagn,* 5**,** 33-8.

CRISTOFANILLI, M., BUDD, G. T., ELLIS, M. J., STOPECK, A., MATERA, J., MILLER, M. C., REUBEN, J. M., DOYLE, G. V., ALLARD, W. J., TERSTAPPEN, L. W. & HAYES, D. F. 2004. Circulating tumor cells, disease progression, and survival in metastatic breast cancer. *N Engl J Med,* 351**,** 781-91.

CRISTOFANILLI, M., HAYES, D. F., BUDD, G. T., ELLIS, M. J., STOPECK, A., REUBEN, J. M., DOYLE, G. V., MATERA, J., ALLARD, W. J. & MILLER, M. C. 2005. Circulating tumor cells: a novel prognostic factor for newly diagnosed metastatic breast cancer. *Journal of clinical oncology,* 23**,** 1420-1430.

CROOK, K., MCLACHLAN, G., STEVENSON, B. J. & PORTEOUS, D. J. 1996. Plasmid DNA molecules complexed with cationic liposomes are protected from degradation by nucleases and shearing by aerosolisation. *Gene Ther,* 3**,** 834-9.

CZERLINSKI, G., REID, D., APOSTOL, A., BAUER, K. & SCARPELLI, D. 1987. Determination of the density of cells from sedimentation studies at 1G. *Journal of Biological Physics,* 15**,** 29-32.

DE BONO, J. S., SCHER, H. I., MONTGOMERY, R. B., PARKER, C., MILLER, M. C., TISSING, H., DOYLE, G. V., TERSTAPPEN, L. W., PIENTA, K. J. & RAGHAVAN, D. 2008. Circulating tumor cells predict survival benefit from treatment in metastatic castration-resistant prostate cancer. *Clinical cancer research,* 14**,** 6302-6309.

DEMIRKAN, B. 2013. The Roles of Epithelial-to-Mesenchymal Transition (EMT) and Mesenchymal-to-Epithelial Transition (MET) in Breast Cancer Bone Metastasis: Potential Targets for Prevention and Treatment. *J Clin Med,* 2**,** 264-82.

DHARMASIRI, U., BALAMURUGAN, S., ADAMS, A. A., OKAGBARE, P. I., OBUBUAFO, A. & SOPER, S. A. 2009. Highly efficient capture and enumeration of low abundance prostate cancer cells using prostate-specific membrane antigen aptamers immobilized to a polymeric microfluidic device. *Electrophoresis,* 30**,** 3289-300.

DING, X., LIN, S. C., KIRALY, B., YUE, H., LI, S., CHIANG, I. K., SHI, J., BENKOVIC, S. J. & HUANG, T. J. 2012. On-chip manipulation of single microparticles, cells, and organisms using surface acoustic waves. *Proc Natl Acad Sci U S A,* 109**,** 11105-9.

DING, X., PENG, Z., LIN, S.-C. S., GERI, M., LI, S., LI, P., CHEN, Y., DAO, M., SURESH, S. & HUANG, T. J. 2014. Cell separation using tilted-angle standing surface acoustic waves. *Proceedings of the National Academy of Sciences,* 111**,** 12992-12997.

DIPARDO, B. J., WINOGRAD, P., COURT, C. M. & TOMLINSON, J. S. 2018. Pancreatic cancer circulating tumor cells: applications for personalized oncology. *Expert review of molecular diagnostics,* 18**,** 809-820.

DMPHOTONICS.COM. *Lithium Tantalate Crystal* [Online]. Available: http://www.dmphotonics.com/LiTaO3_crystal/Lithium%20Tantalate%20Crystal.htm [Accessed 11 Feb 2021].

DOINIKOV, A. 2003. Acoustic radiation forces: Classical theory and recent advances.

DONG, Y., SKELLEY, A. M., MERDEK, K. D., SPROTT, K. M., JIANG, C., PIERCEALL, W. E., LIN, J., STOCUM, M., CARNEY, W. P. & SMIRNOV, D. A. 2013. Microfluidics and circulating tumor cells. *The Journal of Molecular Diagnostics,* 15**,** 149-157.

DOYLE, C., KUSHI, L. H., BYERS, T., COURNEYA, K. S., DEMARK-WAHNEFRIED, W., GRANT, B., MCTIERNAN, A., ROCK, C. L., THOMPSON, C. & GANSLER, T. 2006. Nutrition and physical activity during and after cancer treatment: an American Cancer Society guide for informed choices. *CA: a cancer journal for clinicians,* 56**,** 323-353.

EBLABLA, A. M., LI, X., WALLIS, D. J., GUINEY, I. & ELGAID, K. 2017. GaN on Low-Resistivity Silicon THz High-Q Passive Device Technology. *IEEE Transactions on Terahertz Science and Technology,* 7**,** 93-97.

EVERETT, M. E. 2013. Frontmatter. *Near-Surface Applied Geophysics.* Cambridge: Cambridge University Press.

EXPLORATORIUM. 2021. *Love and Rayleigh waves* [Online]. Available: https://www.exploratorium.edu/faultline/activezone/slides/rlwaves-slide.html [Accessed 20th Jan 2021].

FAKHFOURI, A., DEVENDRAN, C., COLLINS, D. J., AI, Y. & NEILD, A. 2016. Virtual membrane for filtration of particles using surface acoustic waves (SAW). *Lab on a Chip,* 16**,** 3515-3523.

FALL, D., DUQUENNOY, M., OUAFTOUH, M., SMAGIN, N., PIWAKOWSKI, B. & JENOT, F. 2018. Optimization of interdigital transducers for the generation of surface acoustic waves over a large bandwidth (20–125 MHz). *Sensors and Actuators A: Physical,* 273**,** 303-310.

FARIDI, M. A., RAMACHANDRAIAH, H., IRANMANESH, I., GRISHENKOV, D., WIKLUND, M. & RUSSOM, A. 2017. MicroBubble activated acoustic cell sorting. *Biomedical Microdevices,* 19**,** 23.

FAUSTINO, V., CATARINO, S. O., LIMA, R. & MINAS, G. 2016. Biomedical microfluidic devices by using low-cost fabrication techniques: A review. *Journal of biomechanics,* 49**,** 2280-2292.

FERREIRA, M. M., RAMANI, V. C. & JEFFREY, S. S. 2016. Circulating tumor cell technologies. *Mol Oncol,* 10**,** 374-94.

FRANKE, T. A. & WIXFORTH, A. 2008. Microfluidics for Miniaturized Laboratories on a Chip. *ChemPhysChem,* 9**,** 2140-2156.

FRANKEN, B., DE GROOT, M. R., MASTBOOM, W. J., VERMES, I., VAN DER PALEN, J., TIBBE, A. G. & TERSTAPPEN, L. W. 2012. Circulating tumor cells, disease recurrence and survival in newly diagnosed breast cancer. *Breast Cancer Res,* 14**,** R133.

FU, Y. Q., LUO, J. K., NGUYEN, N. T., WALTON, A. J., FLEWITT, A. J., ZU, X. T., LI, Y., MCHALE, G., MATTHEWS, A., IBORRA, E., DU, H. & MILNE, W. I. 2017. Advances in piezoelectric thin films for acoustic biosensors, acoustofluidics and lab-on-chip applications. *Progress in Materials Science,* 89**,** 31-91.

GARG, N., WESTERHOF, T. M., LIU, V., LIU, R., NELSON, E. L. & LEE, A. P. 2018. Whole-blood sorting, enrichment and in situ immunolabeling of cellular subsets using acoustic microstreaming. *Microsystems & Nanoengineering,* 4**,** 17085.

GEDGE, M. & HILL, M. 2012. Acoustofluidics 17: Theory and applications of surface acoustic wave devices for particle manipulation. *Lab on a Chip,* 12**,** 2998-3007.

GEHL, J. J. A. P. S. 2003. Electroporation: theory and methods, perspectives for drug delivery, gene therapy and research. 177**,** 437-447.

GIBSON, D. 2019. Multi-action Pt(IV) anticancer agents; do we understand how they work? *J Inorg Biochem,* 191**,** 77-84.

GLEGHORN, J. P., PRATT, E. D., DENNING, D., LIU, H., BANDER, N. H., TAGAWA, S. T., NANUS, D. M., GIANNAKAKOU, P. A. & KIRBY, B. J. 2010. Capture of circulating tumor cells from whole blood of prostate cancer patients using geometrically enhanced differential immunocapture (GEDI) and a prostate-specific antibody. *Lab Chip,* 10**,** 27-9.

GORGES, T. M., TINHOFER, I., DROSCH, M., RöSE, L., ZOLLNER, T. M., KRAHN, T. & VON AHSEN, O. 2012. Circulating tumour cells escape from EpCAM-based detection due to epithelial-to-mesenchymal transition. *BMC Cancer,* 12**,** 178.

GREINER. 2021. *ONCOQUICK®* [Online]. Available: https://shop.gbo.com/en/usa/products/bioscience/seperation/oncoquick/ [Accessed 20th Jan 2021].

GRüNERT, S., JECHLINGER, M. & BEUG, H. 2003. Diverse cellular and molecular mechanisms contribute to epithelial plasticity and metastasis. *Nat Rev Mol Cell Biol,* 4**,** 657-65.

GU, Y., CHEN, C., WANG, Z., HUANG, P.-H., FU, H., WANG, L., WU, M., CHEN, Y., GAO, T., GONG, J., KWUN, J., AREPALLY, G. M. & HUANG, T. J. 2019. Plastic-based acoustofluidic devices for high-throughput, biocompatible platelet separation. *Lab on a Chip,* 19**,** 394-402.

GUAN, C.-S., WANG, X.-M., LV, Z.-B., YAN, S., SUN, L. & XIE, R.-M. 2018. MRI findings of AIDS-related giant facial Kaposi's sarcoma: A case report. *Medicine,* 97**,** e12530.

GUIGAS, G., KALLA, C. & WEISS, M. 2007. The degree of macromolecular crowding in the cytoplasm and nucleoplasm of mammalian cells is conserved. *FEBS letters,* 581**,** 5094-5098.

GUMBINER, B. M. 1996. Cell adhesion: the molecular basis of tissue architecture and morphogenesis. *Cell,* 84**,** 345-57.

HAN, D., CHEN, K., CHE, J., HANG, J. & LI, H. 2018. Detection of Epithelial-Mesenchymal Transition Status of Circulating Tumor Cells in Patients with Esophageal Squamous Carcinoma. *BioMed Research International,* 2018**,** 7610154.

HANSSEN, A., WAGNER, J., GORGES, T. M., TAENZER, A., UZUNOGLU, F. G., DRIEMEL, C., STOECKLEIN, N. H., KNOEFEL, W. T., ANGENENDT, S., HAUCH, S., ATANACKOVIC, D., LOGES, S., RIETHDORF, S., PANTEL, K. & WIKMAN, H. 2016. Characterization of different CTC subpopulations in non-small cell lung cancer. *Scientific reports,* 6**,** 28010.

HARMEET BHUGRA, G. P. 2017. *Piezoelectric MEMS Resonators*, Springer, Cham.

HAROUAKA, R. A., NISIC, M. & ZHENG, S. Y. 2013. Circulating tumor cell enrichment based on physical properties. *J Lab Autom,* 18**,** 455-68.

HAROUAKA, R. A., ZHOU, M.-D., YEH, Y.-T., KHAN, W. J., DAS, A., LIU, X., CHRIST, C. C., DICKER, D. T., BANEY, T. S. & KAIFI, J. T. 2014. Flexible micro spring array device for high-throughput enrichment of viable circulating tumor cells. *Clinical chemistry,* 60**,** 323-333.

HASHIMOTO, K.-Y. 2000. *Surface Acoustic Wave Devices in Telecommunications*, Springer-Verlag Berlin Heidelberg.

HEITZER, E., HAQUE, I. S., ROBERTS, C. E. S. & SPEICHER, M. R. 2019. Current and future perspectives of liquid biopsies in genomics-driven oncology. *Nat Rev Genet,* 20**,** 71-88.

HELLER, R. & HELLER, L. C. 2015. Gene electrotransfer clinical trials. *Advances in genetics.* Elsevier.

HENSHAW, J. W. & YUAN, F. J. J. O. P. S. 2008. Field distribution and DNA transport in solid tumors during electric field-mediated gene delivery. 97**,** 691-711.

HOGAN, E., ALMIRA-SUAREZ, I., LI, S., COLLINS, S. P. & JEAN, W. C. 2019. Clinical Management of Prostate Cancer Metastasis to Pineal Gland: Case Report and Review of Literature. *World Neurosurg,* 122**,** 464-468.

HOU, H. W., WARKIANI, M. E., KHOO, B. L., LI, Z. R., SOO, R. A., TAN, D. S.-W., LIM, W.-T., HAN, J., BHAGAT, A. A. S. & LIM, C. T. 2013. Isolation and retrieval of circulating tumor cells using centrifugal forces. *Scientific reports,* 3**,** 1259.

HSI, P., CHRISTIANSON, R. J., DUBAY, R. A., LISSANDRELLO, C. A., FIERING, J., BALESTRINI, J. L. & TANDON, V. 2019. Acoustophoretic rapid media exchange and continuous-flow electrotransfection of primary human T cells for applications in automated cellular therapy manufacturing. *Lab on a Chip,* 19**,** 2978-2992.

HVICHIA, G., PARVEEN, Z., WAGNER, C., JANNING, M., QUIDDE, J., STEIN, A., MüLLER, V., LOGES, S., NEVES, R. & STOECKLEIN, N. 2016. A novel microfluidic platform for size and deformability based separation and the subsequent molecular characterization of viable circulating tumor cells. *International journal of cancer,* 138**,** 2894-2904.

INSTITUTE, N. C. 2015. Cancer Staging.

JAIN, S., LIN, S. Y., SONG, W. & SU, Y. H. 2019. Urine-Based Liquid Biopsy for Nonurological Cancers. *Genet Test Mol Biomarkers,* 23**,** 277-283.

JEWETT, S. A., MAKOWSKI, M. S., ANDREWS, B., MANFRA, M. J. & IVANISEVIC, A. 2012. Gallium nitride is biocompatible and non-toxic before and after functionalization with peptides. *Acta Biomaterialia,* 8**,** 728-733.

JIN, C., MCFAUL, S. M., DUFFY, S. P., DENG, X., TAVASSOLI, P., BLACK, P. C. & MA, H. 2014. Technologies for label-free separation of circulating tumor cells: from historical foundations to recent developments. *Lab on a Chip,* 14**,** 32-44.

JOOSSE, S. A., GORGES, T. M. & PANTEL, K. 2015. Biology, detection, and clinical implications of circulating tumor cells. *EMBO Mol Med,* 7**,** 1-11.

KAKO, S., SANTORI, C., HOSHINO, K., GöTZINGER, S., YAMAMOTO, Y. & ARAKAWA, Y. 2006. A gallium nitride single-photon source operating at 200 K. *Nature Materials,* 5**,** 887-892.

KAMATAGI, M. D., SANKESHWAR, N. S. & MULIMANI, B. G. 2007. Thermal conductivity of GaN. *Diamond and Related Materials,* 16**,** 98-106.

KANG, H. M., KIM, G. H., JEON, H. K., KIM, D. H., JEON, T. Y., PARK, D. Y., JEONG, H., CHUN, W. J., KIM, M.-H., PARK, J., LIM, M., KIM, T.-H. & CHO, Y.-K. 2017. Circulating tumor cells detected by lab-on-a-disc: Role in early diagnosis of gastric cancer. *PLOS ONE,* 12**,** e0180251.

KAPELERIS, J., KULASINGHE, A., WARKIANI, M. E., VELA, I., KENNY, L., O'BYRNE, K. & PUNYADEERA, C. 2018. The Prognostic Role of Circulating Tumor Cells (CTCs) in Lung Cancer. *Frontiers in oncology,* 8**,** 311-311.

KATAYAMA, R., SHAW, A. T., KHAN, T. M., MINO-KENUDSON, M., SOLOMON, B. J., HALMOS, B., JESSOP, N. A., WAIN, J. C., YEO, A. T. & BENES, C. 2012. Mechanisms of acquired crizotinib resistance in ALK-rearranged lung cancers. *Science translational medicine,* 4**,** 120ra17-120ra17.

KIRSCHNER, J. 2010. Surface Acoustic Wave Sensors (SAWS). *Micromechanical systems*.

KIRSTE, R., ROHRBAUGH, N., BRYAN, I., BRYAN, Z., COLLAZO, R. & IVANISEVIC, A. 2015. Electronic Biosensors Based on III-Nitride Semiconductors. *Annual Review of Analytical Chemistry,* 8**,** 149-169.

KOOIJMANS, S. A. A., STREMERSCH, S., BRAECKMANS, K., DE SMEDT, S. C., HENDRIX, A., WOOD, M. J. A., SCHIFFELERS, R. M., RAEMDONCK, K. & VADER, P. 2013. Electroporation-induced siRNA precipitation obscures the efficiency of siRNA loading into extracellular vesicles. *J Control Release,* 172**,** 229-238.

KOVACS, G., LUBKING, G. W., VELLEKOOP, M. J. & VENEMA, A. Love waves for (bio)-chemical sensing in liquids. IEEE 1992 Ultrasonics Symposium Proceedings, 20-23 Oct. 1992 1992. 281-285 vol.1.

KUGAENKO, O. M., UVAROVA, S. S., KRYLOV, S. A., SENATULIN, B. R., PETRAKOV, V. S., BUZANOV, O. A., EGOROV, V. N. & SAKHAROV, S. A. 2012. Basic thermophysical parameters of langasite (La3Ga5SiO14), langatate (La3Ta0.5Ga5.5O14), and catangasite (Ca3TaGa3Si2O14) single crystals in a temperature range of 25 to 1000°C. *Bulletin of the Russian Academy of Sciences: Physics,* 76**,** 1258-1263.

KUZMIK, J. 2001. Power electronics on InAlN/(In)GaN: Prospect for a record performance. *IEEE Electron Device Letters,* 22**,** 510-512.

LABGAA, I. & VILLANUEVA, A. 2015. Liquid biopsy in liver cancer. *Discov Med,* 19**,** 263-73.

LAKäMPER, S., LAMPRECHT, A., SCHAAP, I. A. & DUAL, J. 2015. Direct 2D measurement of time-averaged forces and pressure amplitudes in acoustophoretic devices using optical trapping. *Lab on a Chip,* 15**,** 290-300.

LAMBERT, A. W., PATTABIRAMAN, D. R. & WEINBERG, R. A. 2017. Emerging Biological Principles of Metastasis. *Cell,* 168**,** 670-691.

LARA, O., TONG, X., ZBOROWSKI, M. & CHALMERS, J. J. 2004. Enrichment of rare cancer cells through depletion of normal cells using density and flow-through, immunomagnetic cell separation. *Experimental hematology,* 32**,** 891-904.

LATELLA, M. C., DI SALVO, M. T., COCCHIARELLA, F., BENATI, D., GRISENDI, G., COMITATO, A., MARIGO, V. & RECCHIA, A. J. M. T.-N. A. 2016. In vivo editing of the human mutant rhodopsin gene by electroporation of plasmid-based CRISPR/Cas9 in the mouse retina. 5**,** e389.

LAURELL, T., PETERSSON, F. & NILSSON, A. 2007. Chip integrated strategies for acoustic separation and manipulation of cells and particles. *Chemical Society Reviews,* 36**,** 492-506.

LECHARDEUR, D., SOHN, K. J., HAARDT, M., JOSHI, P. B., MONCK, M., GRAHAM, R. W., BEATTY, B., SQUIRE, J., O'BRODOVICH, H. & LUKACS, G. L. 1999. Metabolic instability of plasmid DNA in the cytosol: a potential barrier to gene transfer. *Gene Ther,* 6**,** 482-97.

LEDBETTER, H., OGI, H. & NAKAMURA, N. 2004. Elastic, anelastic, piezoelectric coefficients of monocrystal lithium niobate. *Mechanics of Materials,* 36**,** 941-947.

LEE, K., SHAO, H., WEISSLEDER, R. & LEE, H. 2015. Acoustic Purification of Extracellular Microvesicles. *ACS Nano,* 9**,** 2321-2327.

LENSHOF, A., EVANDER, M., LAURELL, T. & NILSSON, J. 2012a. Acoustofluidics 5: Building microfluidic acoustic resonators. *Lab Chip,* 12**,** 684-95.

LENSHOF, A., MAGNUSSON, C. & LAURELL, T. 2012b. Acoustofluidics 8: applications of acoustophoresis in continuous flow microsystems. *Lab on a Chip,* 12**,** 1210-1223.

LI, J., HAN, X., YU, X., XU, Z., YANG, G., LIU, B. & XIU, P. 2018. Clinical applications of liquid biopsy as prognostic and predictive biomarkers in hepatocellular carcinoma: circulating tumor cells and circulating tumor DNA. *J Exp Clin Cancer Res,* 37**,** 213.

LI, P., MAO, Z., PENG, Z., ZHOU, L., CHEN, Y., HUANG, P.-H., TRUICA, C. I., DRABICK, J. J., EL-DEIRY, W. S., DAO, M., SURESH, S. & HUANG, T. J. 2015a. Acoustic separation of circulating tumor cells. *Proceedings of the National Academy of Sciences,* 112**,** 4970-4975.

LI, S., DING, X., MAO, Z., CHEN, Y., NAMA, N., GUO, F., LI, P., WANG, L., CAMERON, C. E. & HUANG, T. J. 2015b. Standing surface acoustic wave (SSAW)-based cell washing. *Lab on a Chip,* 15**,** 331-338.

LI, S., MA, F., BACHMAN, H., CAMERON, C. E., ZENG, X. & HUANG, T. J. 2017. Acoustofluidic bacteria separation. *Journal of micromechanics and microengineering : structures, devices, and systems,* 27**,** 015031.

LI, S., REN, L., HUANG, P.-H., YAO, X., CUENTO, R. A., MCCOY, J. P., CAMERON, C. E., LEVINE, S. J. & HUANG, T. J. 2016b. Acoustofluidic Transfer of Inflammatory Cells from Human Sputum Samples. *Analytical Chemistry,* 88**,** 5655-5661.

LI, T.-T., LIU, H., LI, F.-P., HU, Y.-F., MOU, T.-Y., LIN, T., YU, J., ZHENG, L. & LI, G.-X. 2015d. Evaluation of epithelial-mesenchymal transitioned circulating tumor cells in patients with resectable gastric cancer: Relevance to therapy response. *World journal of gastroenterology,* 21**,** 13259-13267.

LIM, M., KIM, C. J., SUNKARA, V., KIM, M. H. & CHO, Y. K. 2018. Liquid Biopsy in Lung Cancer: Clinical Applications of Circulating Biomarkers (CTCs and ctDNA). *Micromachines (Basel),* 9.

LINEHAN, W. M., SRINIVASAN, R. & SCHMIDT, L. S. 2010. The genetic basis of kidney cancer: a metabolic disease. *Nature reviews urology,* 7**,** 277.

LIU, H., ZHANG, X., LI, J., SUN, B., QIAN, H. & YIN, Z. 2015. The biological and clinical importance of epithelial-mesenchymal transition in circulating tumor cells. *J Cancer Res Clin Oncol,* 141**,** 189-201.

LOUSADA-FERNANDEZ, F., RAPADO-GONZALEZ, O., LOPEZ-CEDRUN, J. L., LOPEZ-LOPEZ, R., MUINELO-ROMAY, L. & SUAREZ-CUNQUEIRO, M. M. 2018. Liquid Biopsy in Oral Cancer. *Int J Mol Sci,* 19.

LOWE, A. C. 2018. Circulating Tumor Cells: Applications in Cytopathology. *Surg Pathol Clin,* 11**,** 679-686.

LTD, S. T. *Piezoelectric Fundamentals* [Online]. Available: https://sensortechcanada.com/technical-notes/piezoelectric-fundamentals/ [Accessed 01 Feb 2021].

LU, J. & HAN, B. 2018. Liquid Biopsy Promotes Non-Small Cell Lung Cancer Precision Therapy. *Technology in Cancer Research & Treatment,* 17**,** 1533033818801809.

LU, N. N., XIE, M., WANG, J., LV, S. W., YI, J. S., DONG, W. G. & HUANG, W. H. 2015. Biotin-triggered decomposable immunomagnetic beads for capture and release of circulating tumor cells. *ACS Appl Mater Interfaces,* 7**,** 8817-26.

MA, Y., HAO, S., WANG, S., ZHAO, Y., LIM, B., LEI, M., SPECTOR, D. J., EL-DEIRY, W. S., ZHENG, S.-Y. & ZHU, J. 2015. A Combinatory Strategy for Detection of Live CTCs Using Microfiltration and a New Telomerase-Selective Adenovirus. *Molecular Cancer Therapeutics,* 14**,** 835-843.

MACK, C. 2007. Introduction to Semiconductor Lithography. *Fundamental Principles of Optical Lithography.*

MADER, S. & PANTEL, K. 2017. Liquid Biopsy: Current Status and Future Perspectives. *Oncol Res Treat,* 40**,** 404-408.

MAGGIO, I. & GONCALVES, M. A. J. T. I. B. 2015. Genome editing at the crossroads of delivery, specificity, and fidelity. 33**,** 280-291.

MAHESWARAN, S., SEQUIST, L. V., NAGRATH, S., ULKUS, L., BRANNIGAN, B., COLLURA, C. V., INSERRA, E., DIEDERICHS, S., IAFRATE, A. J., BELL, D. W., DIGUMARTHY, S., MUZIKANSKY, A., IRIMIA, D., SETTLEMAN, J., TOMPKINS, R. G., LYNCH, T. J., TONER, M. & HABER, D. A. 2008. Detection of mutations in EGFR in circulating lung-cancer cells. *N Engl J Med,* 359**,** 366-77.

MANOHAR, G. 2012. *Investigation of Various Surface Acoustic Wave Design Configurations for Improved Sensitivity.*

MAO, Z., XIE, Y., GUO, F., REN, L., HUANG, P. H., CHEN, Y., RUFO, J., COSTANZO, F. & HUANG, T. J. 2016. Experimental and numerical studies on standing surface acoustic wave microfluidics. *Lab on a Chip,* 16**,** 515-24.

MARRINUCCI, D., BETHEL, K., LAZAR, D., FISHER, J., HUYNH, E., CLARK, P., BRUCE, R., NIEVA, J. & KUHN, P. 2010. Cytomorphology of circulating colorectal tumor cells: a small case series. *Journal of oncology,* 2010.

MATTOX, A. K., BETTEGOWDA, C., ZHOU, S., PAPADOPOULOS, N., KINZLER, K. W. & VOGELSTEIN, B. 2019. Applications of liquid biopsies for cancer. *Science translational medicine,* 11**,** eaay1984.

MCDONALD, J. C., DUFFY, D. C., ANDERSON, J. R., CHIU, D. T., WU, H., SCHUELLER, O. J. & WHITESIDES, G. M. 2000. Fabrication of microfluidic systems in poly (dimethylsiloxane). *ELECTROPHORESIS: An International Journal,* 21**,** 27-40.

MEHLEN, P. & PUISIEUX, A. 2006. Metastasis: a question of life or death. *Nature reviews cancer,* 6**,** 449-458.

MELLBY, L. D., NYBERG, A. P., JOHANSEN, J. S., WINGREN, C., NORDESTGAARD, B. G., BOJESEN, S. E., MITCHELL, B. L., SHEPPARD, B. C., SEARS, R. C. & BORREBAECK, C. A. K. 2018. Serum Biomarker Signature-Based Liquid Biopsy for Diagnosis of Early-Stage Pancreatic Cancer. *J Clin Oncol,* 36**,** 2887-2894.

MESSARITAKIS, I., NIKOLAOU, M., POLITAKI, E., KOINIS, F., LAGOUDAKI, E., KOUTSOPOULOS, A., GEORGOULIA, N., GEORGOULIAS, V. & KOTSAKIS, A. 2018. Bcl-2 expression in circulating tumor cells (CTCs) of patients with small cell lung cancer (SCLC) receiving front-line treatment. *Lung Cancer,* 124**,** 270-278.

MIKHAYLOV, R., WU, F., WANG, H., CLAYTON, A., SUN, C., XIE, Z., LIANG, D., DONG, Y., YUAN, F., MOSCHOU, D., WU, Z., SHEN, M. H., YANG, J., FU, Y., YANG, Z., BURTON, C., ERRINGTON, R. J., WILTSHIRE, M. & YANG, X. 2020. Development and characterisation of acoustofluidic devices using detachable electrodes made from PCB. *Lab on a Chip,* 20**,** 1807-1814.

MIKOLAJCZYK, S. D., MILLAR, L. S., TSINBERG, P., COUTTS, S. M., ZOMORRODI, M., PHAM, T., BISCHOFF, F. Z. & PIRCHER, T. J. 2011. Detection of EpCAM-Negative and Cytokeratin-Negative Circulating Tumor Cells in Peripheral Blood. *J Oncol,* 2011**,** 252361.

MIRACRYS.COM. 2021. *Langasite and Langatate* [Online]. Available: http://www.miracrys.com/CCinit.php?id=productsg [Accessed 11th Feb 2021].

MULLER, P. B., BARNKOB, R., JENSEN, M. J. H. & BRUUS, H. 2012. A numerical study of microparticle acoustophoresis driven by acoustic radiation forces and streaming-induced drag forces. *Lab on a Chip,* 12**,** 4617-4627.

NAGRATH, S., SEQUIST, L. V., MAHESWARAN, S., BELL, D. W., IRIMIA, D., ULKUS, L., SMITH, M. R., KWAK, E. L., DIGUMARTHY, S. & MUZIKANSKY, A. 2007. Isolation of rare circulating tumour cells in cancer patients by microchip technology. *Nature,* 450**,** 1235-1239.

NAM, S. J., YEO, H. Y., CHANG, H. J., KIM, B. H., HONG, E. K. & PARK, J. W. 2016. A New Cell Block Method for Multiple Immunohistochemical Analysis of Circulating Tumor Cells in Patients with Liver Cancer. *Cancer Res Treat,* 48**,** 1229-1242.

NAMA, N., BARNKOB, R., MAO, Z., KäHLER, C. J., COSTANZO, F. & HUANG, T. J. 2015. Numerical study of acoustophoretic motion of particles in a PDMS microchannel driven by surface acoustic waves. *Lab on a Chip,* 15**,** 2700-2709.

NANKO, M., SHIMADA, H., YAMAOKA, H., TANAKA, K., MASUI, H., MATSUO, K., IKE, H., OKI, S. & HARA, M. 1998. Micrometastatic colorectal cancer lesions in the liver. *Surg Today,* 28**,** 707-13.

NIESSEN, C. M. 2007. Tight junctions/adherens junctions: basic structure and function. *The Journal of investigative dermatology,* 127**,** 2525-2532.

O'RORKE, R., COLLINS, D. & AI, Y. 2018. A rapid and meshless analytical model of acoustofluidic pressure fields for waveguide design. *Biomicrofluidics,* 12**,** 024104.

OHLSSON, P., EVANDER, M., PETERSSON, K., MELLHAMMAR, L., LEHMUSVUORI, A., KARHUNEN, U., SOIKKELI, M., SEPPä, T., TUUNAINEN, E., SPANGAR, A., VON LODE, P., RANTAKOKKO-JALAVA, K., OTTO, G., SCHEDING, S., SOUKKA, T., WITTFOOTH, S. & LAURELL, T. 2016. Integrated Acoustic Separation, Enrichment, and Microchip Polymerase Chain Reaction Detection of Bacteria from Blood for Rapid Sepsis Diagnostics. *Analytical Chemistry,* 88**,** 9403-9411.

OHLSSON, P., PETERSSON, K., AUGUSTSSON, P. & LAURELL, T. 2018. Acoustic impedance matched buffers enable separation of bacteria from blood cells at high cell concentrations. *Scientific Reports,* 8**,** 9156.

OKITA, K., MATSUMURA, Y., SATO, Y., OKADA, A., MORIZANE, A., OKAMOTO, S., HONG, H., NAKAGAWA, M., TANABE, K. & TEZUKA, K.-I. J. N. M. 2011. A more efficient method to generate integration-free human iPS cells. 8**,** 409.

OTA, N., YALIKUN, Y., SUZUKI, T., LEE, S. W., HOSOKAWA, Y., GODA, K. & TANAKA, Y. 2019. Enhancement in acoustic focusing of micro and nanoparticles by thinning a microfluidic device. *Royal Society Open Science,* 6**,** 181776.

PAGET, S. 1889. THE DISTRIBUTION OF SECONDARY GROWTHS IN CANCER OF THE BREAST. *The Lancet,* 133**,** 571-573.

PAKHOMOV, A. G., MIKLAVCIC, D. & MARKOV, M. S. 2010. *Advanced electroporation techniques in biology and medicine*, CRC Press.

PANTEL, K., DENèVE, E., NOCCA, D., COFFY, A., VENDRELL, J. P., MAUDELONDE, T., RIETHDORF, S. & ALIX-PANABIèRES, C. 2012. Circulating epithelial cells in patients with benign colon diseases. *Clin Chem,* 58**,** 936-40.

PARK, J., JUNG, J. H., DESTGEER, G., AHMED, H., PARK, K. & SUNG, H. J. 2017. Acoustothermal tweezer for droplet sorting in a disposable microfluidic chip. *Lab on a Chip,* 17**,** 1031-1040.

PATERLINI-BRECHOT, P. & BENALI, N. L. 2007. Circulating tumor cells (CTC) detection: clinical impact and future directions. *Cancer letters,* 253**,** 180-204.

PECOT, C. V., BISCHOFF, F. Z., MAYER, J. A., WONG, K. L., PHAM, T., BOTTSFORD-MILLER, J., STONE, R. L., LIN, Y. G., JALADURGAM, P., ROH, J. W., GOODMAN, B. W., MERRITT, W. M., PIRCHER, T. J., MIKOLAJCZYK, S. D., NICK, A. M., CELESTINO, J., ENG, C., ELLIS, L. M., DEAVERS, M. T. & SOOD, A. K. 2011. A novel platform for detection of CK+ and CK- CTCs. *Cancer Discov,* 1**,** 580-6.

PEDRóS, J., CALLE, F., GRAJAL, J., JIMéNEZ RIOBóO, R. J., PRIETO, C., PAU, J. L., PEREIRO, J., HERMANN, M., EICKHOFF, M. & BOUGRIOUA, Z. 2004. Anisotropic propagation of surface acoustic waves on nitride layers. *Superlattices and Microstructures,* 36**,** 815-823.

PETERSSON, F., ÅBERG, L., SWäRD-NILSSON, A.-M. & LAURELL, T. 2007. Free flow acoustophoresis: microfluidic-based mode of particle and cell separation. *Analytical chemistry,* 79**,** 5117-5123.

PIYASENA, M. E., AUSTIN SUTHANTHIRARAJ, P. P., APPLEGATE, R. W., JR., GOUMAS, A. M., WOODS, T. A., LóPEZ, G. P. & GRAVES, S. W. 2012. Multinode acoustic focusing for parallel flow cytometry. *Anal Chem,* 84**,** 1831-9.

PLAKS, V., KOOPMAN, C. D. & WERB, Z. 2013. Circulating tumor cells. *Science,* 341**,** 1186-1188.

POLYAK, K. & WEINBERG, R. A. 2009. Transitions between epithelial and mesenchymal states: acquisition of malignant and stem cell traits. *Nat Rev Cancer,* 9**,** 265-73.

POPA, L. C. & WEINSTEIN, D. L-band Lamb mode resonators in Gallium Nitride MMIC technology. 2014 IEEE International Frequency Control Symposium (FCS), 19-22 May 2014 2014. 1-4.

POULET, G., MASSIAS, J. & TALY, V. 2019. Liquid Biopsy: General Concepts. *Acta Cytol,* 63**,** 449-455.

QI, L. N., XIANG, B. D., WU, F. X., YE, J. Z., ZHONG, J. H., WANG, Y. Y., CHEN, Y. Y., CHEN, Z. S., MA, L., CHEN, J., GONG, W. F., HAN, Z. G., LU, Y., SHANG, J. J. & LI, L. Q. 2018a. Circulating Tumor Cells Undergoing EMT Provide a Metric for Diagnosis and Prognosis of Patients with Hepatocellular Carcinoma. *Cancer Res,* 78**,** 4731-4744.

QI, Z.-H., XU, H.-X., ZHANG, S.-R., XU, J.-Z., LI, S., GAO, H.-L., JIN, W., WANG, W.-Q., WU, C.-T., NI, Q.-X., YU, X.-J. & LIU, L. 2018b. The Significance of Liquid Biopsy in Pancreatic Cancer. *Journal of Cancer,* 9**,** 3417-3426.

QIN, W., DION, S. L., KUTNY, P. M., ZHANG, Y., CHENG, A. W., JILLETTE, N. L., MALHOTRA, A., GEURTS, A. M., CHEN, Y.-G. & WANG, H. J. G. 2015. Efficient CRISPR/Cas9-mediated genome editing in mice by zygote electroporation of nuclease. 200**,** 423-430.

RAEYMAEKERS, B., PANTEA, C. & SINHA, D. N. 2011. Manipulation of diamond nanoparticles using bulk acoustic waves. *Journal of Applied Physics,* 109**,** 014317.

RAIS-ZADEH, M., GOKHALE, V. J., ANSARI, A., FAUCHER, M., THéRON, D., CORDIER, Y. & BUCHAILLOT, L. 2014. Gallium Nitride as an Electromechanical Material. *Journal of Microelectromechanical Systems,* 23**,** 1252-1271.

RASHID, M. U. & COOMBS, K. M. 2019. Serum-reduced media impacts on cell viability and protein expression in human lung epithelial cells. *J Cell Physiol,* 234**,** 7718-7724.

RATTAN, R., BIELINSKA, A. U. & BANASZAK HOLL, M. M. 2014. Quantification of cytosolic plasmid DNA degradation using high-throughput sequencing: implications for gene delivery. *The journal of gene medicine,* 16**,** 75-83.

RAYLEIGH, L. 1885. On Waves Propagated along the Plane Surface of an Elastic Solid. *Proceedings of the London Mathematical Society,* s1-17**,** 4-11.

REITER, J. G., MAKOHON-MOORE, A. P., GEROLD, J. M., HEYDE, A., ATTIYEH, M. A., KOHUTEK, Z. A., TOKHEIM, C. J., BROWN, A., DEBLASIO, R. M. & NIYAZOV, J. 2018. Minimal functional driver gene heterogeneity among untreated metastases. *Science,* 361**,** 1033-1037.

REJNIAK, K. A. 2016. Circulating Tumor Cells: When a Solid Tumor Meets a Fluid Microenvironment. *Advances in experimental medicine and biology,* 936**,** 93-106.

REN, K., ZHOU, J. & WU, H. 2013. Materials for microfluidic chip fabrication. *Accounts of chemical research,* 46**,** 2396-2406.

REN, L., YANG, S., ZHANG, P., QU, Z., MAO, Z., HUANG, P. H., CHEN, Y., WU, M., WANG, L., LI, P. & HUANG, T. J. 2018. Standing Surface Acoustic Wave (SSAW)-Based Fluorescence-Activated Cell Sorter. *Small,* 14**,** e1801996.

REYA, T., MORRISON, S. J., CLARKE, M. F. & WEISSMAN, I. L. 2001. Stem cells, cancer, and cancer stem cells. *nature,* 414**,** 105-111.

RIETHDORF, S., O'FLAHERTY, L., HILLE, C. & PANTEL, K. 2018. Clinical applications of the CellSearch platform in cancer patients. *Adv Drug Deliv Rev,* 125**,** 102-121.

RODITI.COM. *Lithium Niobate Properties* [Online]. Available: http://www.roditi.com/SingleCrystal/LiNbO3/liNBO3-Properties.html [Accessed 11 Feb 2021].

RODITI.COM. *Lithium Tantalate Properties* [Online]. Available: http://www.roditi.com/SingleCrystal/Lithium-Tantalate/LiTaO3-Properties.html [Accessed 11 Feb 2021].

RODRIGUEZ, P. L., HARADA, T., CHRISTIAN, D. A., PANTANO, D. A., TSAI, R. K. & DISCHER, D. E. 2013. Minimal "Self" Peptides That Inhibit Phagocytic Clearance and Enhance Delivery of Nanoparticles. *Science,* 339**,** 971-975.

SAMANDARI, M., JULIA, M. G., RICE, A., CHRONOPOULOS, A. & DEL RIO HERNANDEZ, A. E. 2018. Liquid biopsies for management of pancreatic cancer. *Transl Res,* 201**,** 98-127.

SANTASUSAGNA, S., MORENO, I., NAVARRO, A., CASTELLANO, J. J., MARTINEZ, F., HERNáNDEZ, R., MUñOZ, C. & MONZO, M. 2018. Proteomic Analysis of Liquid Biopsy from Tumor-Draining Vein Indicates that High Expression of Exosomal ECM1 Is Associated with Relapse in Stage I-III Colon Cancer. *Translational Oncology,* 11**,** 715-721.

SATELLI, A., BROWNLEE, Z., MITRA, A., MENG, Q. H. & LI, S. 2015a. Circulating tumor cell enumeration with a combination of epithelial cell adhesion molecule- and cell-surface vimentin-based methods for monitoring breast cancer therapeutic response. *Clin Chem,* 61**,** 259-66.

SATELLI, A., MITRA, A., BROWNLEE, Z., XIA, X., BELLISTER, S., OVERMAN, M. J., KOPETZ, S., ELLIS, L. M., MENG, Q. H. & LI, S. 2015b. Epithelial-mesenchymal transitioned circulating tumor cells capture for detecting tumor progression. *Clin Cancer Res,* 21**,** 899-906.

SCHMID, L., WEITZ, D. A. & FRANKE, T. 2014. Sorting drops and cells with acoustics: acoustic microfluidic fluorescence-activated cell sorter. *Lab on a Chip,* 14**,** 3710-3718.

SCHUMANN, K., LIN, S., BOYER, E., SIMEONOV, D. R., SUBRAMANIAM, M., GATE, R. E., HALIBURTON, G. E., CHUN, J. Y., BLUESTONE, J. A. & DOUDNA, J. A. J. P. O. T. N. A. O. S. 2015. Generation of knock-in primary human T cells using Cas9 ribonucleoproteins. 112**,** 10437-10442.

SEARCH, C. 2020. *CELLSEARCH® System Overview* [Online]. Available: https://www.cellsearchctc.com/product-systems-overview/cellsearch-system-overview [Accessed 14 May 2020].

SEHGAL, P. & KIRBY, B. J. 2017. Separation of 300 and 100 nm Particles in Fabry–Perot Acoustofluidic Resonators. *Analytical Chemistry,* 89**,** 12192-12200.

SERRANO, M. J., ORTEGA, F. G., ALVAREZ-CUBERO, M. J., NADAL, R., SANCHEZ-ROVIRA, P., SALIDO, M., RODRíGUEZ, M., GARCíA-PUCHE, J. L., DELGADO-RODRIGUEZ, M., SOLé, F., GARCíA, M. A., PERáN, M., ROSELL, R., MARCHAL, J. A. & LORENTE, J. A. 2014. EMT and EGFR in CTCs cytokeratin negative non-metastatic breast cancer. *Oncotarget,* 5**,** 7486-97.

SETTNES, M & BRUUS, H 2012, 'Forces acting on a small particle in an acoustical field in a viscous fluid', *Physical Review E,* vol. 85, no. 1, pp. 016327.

SHANKAR, G. M., BALAJ, L., STOTT, S. L., NAHED, B. & CARTER, B. S. 2017. Liquid biopsy for brain tumors. *Expert Rev Mol Diagn,* 17**,** 943-947.

SHEN, Z., WU, A. & CHEN, X. 2017. Current detection technologies for circulating tumor cells. *Chemical Society Reviews,* 46**,** 2038-2056.

SHI, J., HUANG, H., STRATTON, Z., HUANG, Y. & HUANG, T. J. 2009. Continuous particle separation in a microfluidic channelvia standing surface acoustic waves (SSAW). *Lab on a Chip,* 9**,** 3354-3359.

SHIBUE, T., BROOKS, M. W., INAN, M. F., REINHARDT, F. & WEINBERG, R. A. 2012. The outgrowth of micrometastases is enabled by the formation of filopodium-like protrusions. *Cancer Discov,* 2**,** 706-21.

SIROHI, J. & CHOPRA, I. 2000. Fundamental Understanding of Piezoelectric Strain Sensors. *Journal of Intelligent Material Systems and Structures,* 11**,** 246-257.

SKOV, N. R. & BRUUS, H. 2016. Modeling of Microdevices for SAW-Based Acoustophoresis — A Study of Boundary Conditions. *Micromachines,* 7**,** 182.

SMIT, M. A., GEIGER, T. R., SONG, J. Y., GITELMAN, I. & PEEPER, D. S. 2009. A Twist-Snail axis critical for TrkB-induced epithelial-mesenchymal transition-like transformation, anoikis resistance, and metastasis. *Mol Cell Biol,* 29**,** 3722-37.

SNYDER, P. J., LAJEUNESSE, D. R., REDDY, P., KIRSTE, R., COLLAZO, R. & IVANISEVIC, A. 2018. Bioelectronics communication: encoding yeast regulatory responses using nanostructured gallium nitride thin films. *Nanoscale,* 10**,** 11506-11516.

SQUIRES, T. M. & QUAKE, S. R. 2005. Microfluidics: Fluid physics at the nanoliter scale. *Reviews of modern physics,* 77**,** 977.

STAFF, M. C. 2020. *Adjuvant therapy: Treatment to keep cancer from returning* [Online]. Available: https://www.mayoclinic.org/diseases-conditions/cancer/in-depth/adjuvant-therapy/art-20046687 [Accessed 10th Oct 2021].

STAPULIONIS, R. 1999. Electric pulse-induced precipitation of biological macromolecules in electroporation. *Bioelectrochem Bioenerg,* 48**,** 249-54.

STEINBICHLER, T. B., DUDáS, J., SKVORTSOV, S., GANSWINDT, U., RIECHELMANN, H. & SKVORTSOVA, I.-I. 2018. Therapy resistance mediated by cancer stem cells. *Seminars in cancer biology,* 53**,** 156-167.

SU, Y. H., KIM, A. K. & JAIN, S. 2018. Liquid biopsies for hepatocellular carcinoma. *Transl Res,* 201**,** 84-97.

SZCZEPANIK, A., SIERZEGA, M., DRABIK, G., PITUCH-NOWOROLSKA, A., KOŁODZIEJCZYK, P. & ZEMBALA, M. 2019. CD44+ cytokeratin-positive tumor cells in blood and bone marrow are associated with poor prognosis of patients with gastric cancer. *Gastric Cancer,* 22**,** 264-272.

TALASAZ, A. H., POWELL, A. A., HUBER, D. E., BERBEE, J. G., ROH, K. H., YU, W., XIAO, W., DAVIS, M. M., PEASE, R. F., MINDRINOS, M. N., JEFFREY, S. S. & DAVIS, R. W. 2009. Isolating highly enriched populations of circulating epithelial cells and other rare cells from blood using a magnetic sweeper device. *Proc Natl Acad Sci U S A,* 106**,** 3970-5.

TAN, Y. & WU, H. 2018. The significant prognostic value of circulating tumor cells in colorectal cancer: A systematic review and meta-analysis. *Curr Probl Cancer,* 42**,** 95-106.

TANCRELL, R. H., SCHULZ, M. B., BARRETT, H. H., DAVIS, L. & HOLLAND, M. G. 1969. Dispersive delay lines using ultrasonic surface waves. *Proceedings of the IEEE,* 57**,** 1211-1213.

THAKORE, P. I., D'IPPOLITO, A. M., SONG, L., SAFI, A., SHIVAKUMAR, N. K., KABADI, A. M., REDDY, T. E., CRAWFORD, G. E. & GERSBACH, C. A. J. N. M. 2015. Highly specific epigenome editing by CRISPR-Cas9 repressors for silencing of distal regulatory elements. 12**,** 1143.

THEVENARD, L., CAMARA, I. S., PRIEUR, J. Y., ROVILLAIN, P., LEMAîTRE, A., GOURDON, C. & DUQUESNE, J. Y. 2016. Strong reduction of the coercivity by a surface acoustic wave in an out-of-plane magnetized epilayer. *Physical Review B,* 93**,** 140405.

THIERY, J. P., ACLOQUE, H., HUANG, R. Y. & NIETO, M. A. 2009. Epithelial-mesenchymal transitions in development and disease. *Cell,* 139**,** 871-90.

TIE, J., WANG, Y., TOMASETTI, C., LI, L., SPRINGER, S., KINDE, I., SILLIMAN, N., TACEY, M., WONG, H.-L. & CHRISTIE, M. 2016. Circulating tumor DNA analysis detects minimal residual disease and predicts recurrence in patients with stage II colon cancer. *Science translational medicine,* 8**,** 346ra92-346ra92.

TRAPP, E., JANNI, W., SCHINDLBECK, C., JüCKSTOCK, J., ANDERGASSEN, U., DE GREGORIO, A., ALUNNI-FABBRONI, M., TZSCHASCHEL, M., POLASIK, A., KOCH, J. G., FRIEDL, T. W. P., FASCHING, P. A., HAEBERLE, L., FEHM, T., SCHNEEWEISS, A., BECKMANN, M. W., PANTEL, K., MUELLER, V., RACK, B. & SCHOLZ, C. 2019. Presence of Circulating Tumor Cells in High-Risk Early Breast Cancer During Follow-Up and Prognosis. *J Natl Cancer Inst,* 111**,** 380-387.

TRAVAGLIATI, M., SHILTON, R., BELTRAM, F. & CECCHINI, M. 2013. Fabrication, Operation and flow visualization in surface-acoustic-wave-driven acoustic-counterflow microfluidics. *JoVE (Journal of Visualized Experiments)***,** e50524.

TRUINI, A., ALAMA, A., DAL BELLO, M. G., COCO, S., VANNI, I., RIJAVEC, E., GENOVA, C., BARLETTA, G., BIELLO, F. & GROSSI, F. 2014. Clinical Applications of Circulating Tumor Cells in Lung Cancer Patients by CellSearch System. *Front Oncol,* 4**,** 242.

TUCHIN, V. V., TáRNOK, A. & ZHAROV, V. P. 2011. In vivo flow cytometry: a horizon of opportunities. *Cytometry Part A,* 79**,** 737-745.

UEN, Y.-H., LU, C.-Y., TSAI, H.-L., YU, F.-J., HUANG, M.-Y., CHENG, T.-L., LIN, S.-R. & WANG, J.-Y. 2008. Persistent presence of postoperative circulating tumor cells is a poor prognostic factor for patients with stage I–III colorectal cancer after curative resection. *Annals of surgical oncology,* 15**,** 2120.

UK, C. R. 2020. Cancer Statistics for the UK.

UPADHYAY, A. K., SINGH, R., SINGH, J. S. & SINGH, D. P. 2019. Chapter 21 - Microalgae-Assisted Phyco-Remediation and Energy Crisis Solution: Challenges and Opportunity. *In:* SINGH, J. S. & SINGH, D. P. (eds.) *New and Future Developments in Microbial Biotechnology and Bioengineering.* Elsevier.

VAN DE STOLPE, A., PANTEL, K., SLEIJFER, S., TERSTAPPEN, L. W. & DEN TOONDER, J. M. 2011. Circulating tumor cell isolation and diagnostics: toward routine clinical use. AACR.

WANG, L., KODZIUS, R., YI, X., LI, S., HUI, Y. S. & WEN, W. 2012. Prototyping chips in minutes: Direct Laser Plotting (DLP) of functional microfluidic structures. *Sensors and Actuators B: Chemical,* 168**,** 214-222.

WANG, S., LIU, K., LIU, J., YU, Z. T.-F., XU, X., ZHAO, L., LEE, T., LEE, E. K., REISS, J., LEE, Y.-K., CHUNG, L. W. K., HUANG, J., RETTIG, M., SELIGSON, D., DURAISWAMY, K. N., SHEN, C. K.-F. & TSENG, H.-R. 2011. Highly Efficient Capture of Circulating Tumor Cells by Using Nanostructured Silicon Substrates with Integrated Chaotic Micromixers. *Angewandte Chemie International Edition,* 50**,** 3084-3088.

WANG, W., ZHAO, Q., HU, A., HE, X. & ZHU, X. 2017. Application of Indocyanine Green (ICG) Detection in Evaluating Early Prognosis in Patients with Fatty Liver Disease After Liver Transplantation. *Annals of transplantation,* 22**,** 208-214.

WEN, Y. F., CHENG, T. T., CHEN, X. L., HUANG, W. J., PENG, H. H., ZHOU, T. C., LIN, X. D. & ZENG, L. S. 2018. Elevated circulating tumor cells and squamous cell carcinoma antigen levels predict poor survival for patients with locally advanced cervical cancer treated with radiotherapy. *PLoS One,* 13**,** e0204334.

WENG, W. H., HO, I. L., PANG, C. C., PANG, S. N., PAN, T. M. & LEUNG, W. H. 2018. Real-time circulating tumor cells detection via highly sensitive needle-like cytosensor-demonstrated by a blood flow simulation. *Biosens Bioelectron,* 116**,** 51-59.

WIKIMEDIA. 2021. *Standing wave* [Online]. Available: https://upload.wikimedia.org/wikipedia/commons/thumb/4/4b/Standingwaves.svg/1200px-Standingwaves.svg.png [Accessed 1st Jan 2021].

WONG, K., TANG, W., LAU, K. M. & CHEN, K. J. Planar Two-dimensional Electron Gas (2DEG) IDT SAW Filter on AlGaN/GaN Heterostructure. 2007 IEEE/MTT-S International Microwave Symposium, 3-8 June 2007 2007. 2043-2046.

WONG, S. C. C., CHAN, C. M. L., MA, B. B. Y., HUI, E. P., NG, S. S. M., SAN LAI, P. B., CHEUNG, M. T., LO, E. S. F., CHAN, A. K. C. & LAM, M. Y. Y. 2009. Clinical significance of cytokeratin 20-positive circulating tumor cells detected by a refined immunomagnetic enrichment assay in colorectal cancer patients. *Clinical Cancer Research,* 15**,** 1005-1012.

WOODARD, G. A., JONES, K. D. & JABLONS, D. M. 2016. Lung Cancer Staging and Prognosis. *Cancer Treat Res,* 170**,** 47-75.

WOODS, R. C. & BOROUMAND, F. A. 2006. Comments on "Epitaxially grown GaN thin-film SAW filter with high velocity and low insertion loss". *IEEE Transactions on Electron Devices,* 53**,** 173-176.

WU, M., CHEN, C., WANG, Z., BACHMAN, H., OUYANG, Y., HUANG, P.-H., SADOVSKY, Y. & HUANG, T. J. 2019a. Separating extracellular vesicles and lipoproteins via acoustofluidics. *Lab on a Chip,* 19**,** 1174-1182.

WU, M., CHEN, K., YANG, S., WANG, Z., HUANG, P.-H., MAI, J., LI, Z.-Y. & HUANG, T. J. 2018a. High-throughput cell focusing and separation via acoustofluidic tweezers. *Lab on a Chip,* 18**,** 3003-3010.

WU, M., HUANG, P.-H., ZHANG, R., MAO, Z., CHEN, C., KEMENY, G., LI, P., LEE, A. V., GYANCHANDANI, R., ARMSTRONG, A. J., DAO, M., SURESH, S. & HUANG, T. J. 2018b. Circulating Tumor Cell Phenotyping via High-Throughput Acoustic Separation. 14**,** 1801131.

WU, M., OUYANG, Y., WANG, Z., ZHANG, R., HUANG, P.-H., CHEN, C., LI, H., LI, P., QUINN, D., DAO, M., SURESH, S., SADOVSKY, Y. & HUANG, T. J. 2017b. Isolation of exosomes from whole blood by integrating acoustics and microfluidics. *Proceedings of the National Academy of Sciences,* 114**,** 10584.

WU, M., OZCELIK, A., RUFO, J., WANG, Z., FANG, R. & HUANG, T. J. 2019b. Acoustofluidic separation of cells and particles. *Microsystems & nanoengineering,* 5**,** 32.

XIE, Y., BACHMAN, H. & HUANG, T. J. 2019. Acoustofluidic methods in cell analysis. *TrAC Trends in Analytical Chemistry,* 117**,** 280-290.

XIONG, K., WEI, W., JIN, Y., WANG, S., ZHAO, D., WANG, S., GAO, X., QIAO, C., YUE, H. & MA, G. 2016. Biomimetic Immuno‐Magnetosomes for High‐Performance Enrichment of Circulating Tumor Cells. *Advanced Materials,* 28**,** 7929-7935.

XU, X. & WOODS, R. C. 2010. On the piezoelectric coupling constant of epitaxial Mg-doped GaN. *Solid-State Electronics,* 54**,** 680-684.

XUE, J., K XIE, V., WANG, P., CUI, J., GAO, Y. & LU, Z. 2014. Interrelationships of circulating tumor cells with metastasis and thrombosis: role of microRNAs. *Current pharmaceutical design,* 20**,** 5298-5308.

YADAV, D. K., BAI, X., YADAV, R. K., SINGH, A., LI, G., MA, T., CHEN, W. & LIANG, T. 2018. Liquid biopsy in pancreatic cancer: the beginning of a new era. *Oncotarget,* 9.

YANG, J., KALOGEROU, M., GALLACHER, J., SAMPSON, J. R. & SHEN, M. H. 2013. Renal tumours in a Tsc1^{+/–} mouse model show epigenetic suppression of organic cation transporters Slc22a1, Slc22a2 and Slc22a3, and do not respond to metformin. *European Journal of Cancer,* 49**,** 1479-1490.

YANG, J., KALOGEROU, M., SAMSEL, P. A., ZHANG, Y., GRIFFITHS, D. F., GALLACHER, J., SAMPSON, J. R. & SHEN, M. H. 2015. Renal tumours in a Tsc2(+/-) mouse model do not show feedback inhibition of Akt and are effectively prevented by rapamycin. *Oncogene,* 34**,** 922-31.

YANG, L., LANG, J. C., BALASUBRAMANIAN, P., JATANA, K. R., SCHULLER, D., AGRAWAL, A., ZBOROWSKI, M. & CHALMERS, J. J. 2009. Optimization of an enrichment process for circulating tumor cells from the blood of head and neck cancer patients through depletion of normal cells. *Biotechnol Bioeng,* 102**,** 521-34.

YANG, W., MU, T., JIANG, J., SUN, Q., HOU, X., SUN, Y., ZHONG, L., WANG, C. & SUN, C. 2018. Identification of Potential Biomarkers and Metabolic Profiling of Serum in Ovarian Cancer Patients Using UPLC/Q-TOF MS. *Cellular Physiology and Biochemistry,* 51**,** 1134-1148.

YAO, S., WANG, J., LIU, H., HU, X., ZHANG, H., CHENG, X. & LING, Z. 2008. Growth, optical and thermal properties of near-stoichiometric LiNbO3 single crystal. *Journal of Alloys and Compounds,* 455**,** 501-505.

YEH, Y.-T., HAROUAKA, R. A. & ZHENG, S.-Y. 2017. Evaluating a novel dimensional reduction approach for mechanical fractionation of cells using a tandem flexible micro spring array (tFMSA). *Lab on a Chip,* 17**,** 691-701.

YIN, J., WANG, Z., LI, G., LIN, F., SHAO, K., CAO, B. & HOU, Y. 2019. Characterization of circulating tumor cells in breast cancer patients by spiral microfluidics. *Cell Biol Toxicol,* 35**,** 59-66.

YOON, H. J., SHANKER, A., WANG, Y., KOZMINSKY, M., JIN, Q., PALANISAMY, N., BURNESS, M. L., AZIZI, E., SIMEONE, D. M., WICHA, M. S., KIM, J. & NAGRATH, S. 2016. Tunable Thermal-Sensitive Polymer-Graphene Oxide Composite for Efficient Capture and Release of Viable Circulating Tumor Cells. *Adv Mater,* 28**,** 4891-7.

YU, M., STOTT, S., TONER, M., MAHESWARAN, S. & HABER, D. A. 2011. Circulating tumor cells: approaches to isolation and characterization. *Journal of Cell Biology,* 192**,** 373-382.

ZASZCZYŃSKA, A., GRADYS, A. & SAJKIEWICZ, P. 2020. Progress in the Applications of Smart Piezoelectric Materials for Medical Devices. *Polymers,* 12**,** 2754.

ZHANG, C., HUANG, K.-C., RAJWA, B., LI, J., YANG, S., LIN, H., LIAO, C.-S., EAKINS, G., KUANG, S., PATSEKIN, V., ROBINSON, J. P. & CHENG, J.-X. 2017. Stimulated Raman scattering flow cytometry for label-free single-particle analysis. *Optica,* 4**,** 103-109.

ZHANG, J., SHI, H., JIANG, T., LIU, Z., LIN, P. P. & CHEN, N. 2018. Circulating tumor cells with karyotyping as a novel biomarker for diagnosis and treatment of nasopharyngeal carcinoma. *BMC Cancer,* 18**,** 1133.

ZHANG, P., BACHMAN, H., OZCELIK, A. & HUANG, T. J. 2020. Acoustic Microfluidics. *Annu Rev Anal Chem (Palo Alto Calif),* 13**,** 17-43.

ZHAO, S., WU, M., YANG, S., WU, Y., GU, Y., CHEN, C., YE, J., XIE, Z., TIAN, Z. & BACHMAN, H. 2020. A disposable acoustofluidic chip for nano/microparticle separation using unidirectional acoustic transducers. *Lab on a Chip*.

ZHOU, M.-D., HAO, S., WILLIAMS, A. J., HAROUAKA, R. A., SCHRAND, B., RAWAL, S., AO, Z., BRENNEMAN, R., GILBOA, E. & LU, B. 2014. Separable bilayer microfiltration device for viable label-free enrichment of circulating tumour cells. *Scientific reports,* 4**,** 7392.